





Hyperbolic Spin Liquids

Patrick M. Lenggenhager ^{1,*}, Santanu Dey ², Tomáš Bzdušek ³, and Joseph Maciejko ^{2,4,†}

¹Max Planck Institute for the Physics of Complex Systems, Nöthnitzer Str. 38, 01187 Dresden, Germany

²Department of Physics, University of Alberta, Edmonton, Alberta T6G 2E1, Canada

³Department of Physics, University of Zürich, Winterthurerstrasse 190, 8057 Zürich, Switzerland

⁴Theoretical Physics Institute & Quantum Horizons Alberta,
University of Alberta, Edmonton, Alberta T6G 2E1, Canada

(Dated: July 16, 2024)

Hyperbolic lattices present a unique opportunity to venture beyond the conventional paradigm of crystalline many-body physics and explore correlated phenomena in negatively curved space. As a theoretical benchmark for such investigations, we extend Kitaev’s spin-1/2 honeycomb model to hyperbolic lattices and exploit their non-Euclidean space-group symmetries to solve the model exactly. We elucidate the ground-state phase diagram on the $\{8, 3\}$ lattice and find a gapped \mathbb{Z}_2 spin liquid with Abelian anyons, a gapped chiral spin liquid with non-Abelian anyons and chiral edge states, and a compressible spin liquid with low-energy density of states dominated by non-Abelian Bloch states of Majorana fermions.

Introduction.—Among the factors that influence the collective behavior of quantum materials, lattice geometry plays a crucial role, from determining the electronic band structure for weak correlations to geometrically frustrating conventional orders for strong correlations [1]. Hyperbolic $\{p, q\}$ lattices [2–8]—synthetic materials that emulate regular tilings of two-dimensional (2D) hyperbolic space by p -sided polygons with coordination q , with $(p-2)(q-2) > 4$ [9]—present a unique opportunity to explore many-body physics on unusual, non-Euclidean lattice geometries. While a wealth of phenomena have been investigated on hyperbolic lattices at the single-particle level [10–42], much less is known about the interplay of negative curvature and many-body correlations.

Hyperbolic analogs of prototypical interacting Hamiltonians such as the quantum Ising, XY, and Heisenberg models [43–45] and the Bose [46] and Fermi [45, 47, 48] Hubbard models have been studied recently using mean-field theory, spin-wave theory, and quantum Monte Carlo (QMC). However, the ability of such methods to reliably capture the bulk properties of hyperbolic lattices must be critically assessed. For example, finite $\{10, 3\}$ lattices display a low-energy density of states (DOS) that appears semimetallic [45, 47], but the thermodynamic-limit DOS is known to be finite [24], with important consequences for many-body physics. Thus, even numerically exact methods such as QMC may suffer from unusually severe finite-size effects in the hyperbolic context. This motivates a search for exactly solvable models, to not only discover interesting emergent phenomena but also benchmark approximate many-body theories of hyperbolic lattices.

Here, we introduce for the first time an exactly solvable model of strongly correlated spins on hyperbolic lattices (Fig. 1). Our model generalizes Kitaev’s honeycomb lattice model [49] to $\{p, 3\}$ lattices and can be solved exactly for any even $p \geq 8$. Although the Kitaev model can be generalized to arbitrary 3-coordinated graphs, exact solvability does not immediately follow. First, a 3-edge coloring of the graph

must exist and be explicitly constructed, which is in general an NP-complete problem [50]. Second, even with conserved plaquette fluxes [49], the flux optimization problem is generically hard because of the exponential growth of flux configurations with system size. While Lieb’s lemma [51–55] can simplify the problem if reflection symmetries are present, to the difference of Euclidean lattices, non-crystalline structures typically possess at most finitely many such symmetries, thus exponentially many flux configurations must still be sampled numerically [56, 57]. Here, we resolve both issues by exploiting the space-group symmetries of hyperbolic lattices [11, 19, 20]. First, infinitely many non-Euclidean reflection symmetries allow us to simultaneously solve the 3-edge coloring problem *and* determine the ground-state flux configuration analytically. Second, the (noncommutative) translation symmetry enables us to efficiently approximate the thermodynamic limit via hyperbolic band theory (HBT) [11–13]. We study the model at zero temperature on the $\{8, 3\}$ lattice and find two gapped topological phases: a \mathbb{Z}_2 spin liquid with Abelian anyons, and a chiral spin liquid with non-Abelian anyons and chiral Majorana edge modes. At a single point in the phase diagram, we also find a gapless spin liquid that—unlike Kitaev’s Dirac spin liquid [49]—is compressible, with a finite low-energy DOS dominated by non-Abelian Bloch states [12].

Hyperbolic Kitaev model.—We consider hyperbolic $\{p, 3\}$ lattices with a 3-edge coloring, i.e., an assignment of one of three colors (yellow, red, blue, labeled as $\alpha = x, y, z$, respectively) to each edge such that coincident edges have different colors (Fig. 1a). With an $s = 1/2$ spin on each site, we define the ferromagnetic ($J_\alpha > 0$) hyperbolic Kitaev model (HKM) as:

$$\hat{\mathcal{H}} = - \sum_{\langle j, k \rangle_\alpha} J_\alpha \hat{\sigma}_j^\alpha \hat{\sigma}_k^\alpha - K \sum_{[lmn]_{\alpha\beta\gamma}^+} \varepsilon_{\alpha\beta\gamma} \hat{\sigma}_l^\alpha \hat{\sigma}_m^\beta \hat{\sigma}_n^\gamma. \quad (1)$$

The J_α term is an anisotropic exchange interaction between adjacent sites j, k sharing an α -edge $\langle j, k \rangle_\alpha$. The term involving the totally antisymmetric tensor $\varepsilon_{\alpha\beta\gamma}$ is an interaction among a counterclockwise-oriented triplet of sites n, m, l (denoted $[lmn]_{\alpha\beta\gamma}^+$) that are connected by bonds $\langle l, m \rangle_\alpha$ and $\langle m, n \rangle_\gamma$, respectively, with $\beta \neq \alpha, \gamma$ the color of the third bond adjacent to site m [58]. This term can arise as the leading-order

* plengg@pks.mpg.de
† maciejko@ualberta.ca

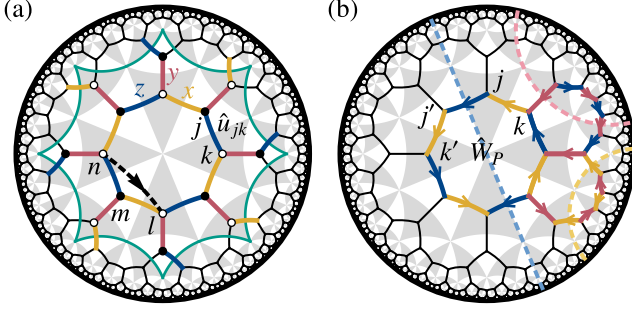


FIG. 1. (a) Hyperbolic Kitaev model on the $\{8, 3\}$ lattice with two sublattices (white/black dots). Symmetric 3-edge coloring (yellow/red/blue, representing $x/y/z$) shown inside the primitive cell (green octagon with opposite edges identified). Adjacent sites j, k form a bond $\langle j, k \rangle_z$; sites n, m, l form an oriented triplet $[lmn]_{xyz}^+$. In the Majorana representation, these generate the bond operator \hat{u}_{jk} and a next-nearest-neighbor term (dashed black arrow), respectively. The symmetry of the model is depicted by the gray/white triangles. (b) Application of Lieb's lemma to determine the ground-state flux sector for three representative plaquettes. Three independent mirror lines (dashed geodesics) cut bonds of a different color. Separately for each plaquette, reflection positivity with respect to one of them implies ground-state bond eigenvalues $u_{jk} = +1$ as indicated by arrows from k to j (up to gauge transformations). This constrains the gauge-invariant plaquette operators \hat{W}_P consistently throughout the lattice: here $W_P = -1$ for all P .

nontrivial effect of a perturbation $-\sum_{j,\alpha} h_\alpha \hat{\sigma}_j^\alpha$ by an external magnetic field \mathbf{h} [49], or through Floquet engineering [59].

Not all graphs are 3-edge colorable, but any 3-coordinated bipartite simple graph is according to König's theorem [60]. Although this applies to any infinite $\{p, 3\}$ lattice with even p , such a coloring is not unique. In the Supplemental Material (SM) [58], we construct a 3-edge coloring for any hyperbolic $\{p, 3\}$ lattice with p even (see Fig. 1a for $p=8$) such that Eq. (1) is symmetric with respect to any (non-Euclidean) bond-cutting reflection, of which there are three types (Fig. 1b). The coloring is also compatible with translation symmetry and appropriately chosen periodic boundary conditions (PBC) [58].

Majorana representation.—We now solve the HKM exactly. At each site j , we introduce the Majorana fermions \hat{b}_j^α , $\alpha \in \{x, y, z\}$ and \hat{c}_j such that $\hat{\sigma}_j^\alpha = i\hat{b}_j^\alpha \hat{c}_j$ [49]. Defining the bond operator $\hat{u}_{jk} = i\hat{b}_j^\alpha \hat{b}_k^\alpha$ on edge $\langle j, k \rangle_\alpha$, the Hamiltonian becomes [58]

$$\hat{\mathcal{H}} = \sum_{\langle j,k \rangle_\alpha} J_\alpha \hat{u}_{jk} i\hat{c}_j \hat{c}_k + K \sum_{[lmn]_{\alpha\beta\gamma}^+} \hat{u}_{lm} \hat{u}_{mn} i\hat{c}_l \hat{c}_n. \quad (2)$$

While $\hat{\mathcal{H}}$ in Eq. (2) acts on the extended Hilbert space, $\hat{\mathcal{H}}$ in Eq. (1) only acts on the physical Hilbert space of the spin system, defined as the common $+1$ eigenspace of the \mathbb{Z}_2 gauge transformations $\hat{D}_j = \hat{b}_j^x \hat{b}_j^y \hat{b}_j^z \hat{c}_j$.

Because the \hat{u}_{jk} commute with $\hat{\mathcal{H}}$ and each other, we replace them by their eigenvalues $u_{jk} = \pm 1$ and study the resulting quadratic Majorana Hamiltonian. Since the bond operators are not gauge invariant, we consider the Wilson loops

$\hat{W}(\ell) = \prod_{\langle j,k \rangle_\alpha \in \ell} \hat{\sigma}_j^\alpha \hat{\sigma}_k^\alpha$ along closed paths ℓ . In the Majorana representation, they take the form $\hat{W}(\ell) = \prod_{\langle j,k \rangle_\alpha \in \ell} (-i\hat{u}_{jk})$. On an infinite hyperbolic lattice, all u_{jk} are (up to gauge transformations) fully determined by the Wilson loops \hat{W}_P around the individual plaquettes P , measuring the corresponding flux. On compactified PBC clusters with genus g , plaquette fluxes can only be changed in pairs, and there also exist Wilson loops along $2g$ noncontractible paths [22].

Exact solution of the flux problem.—For $K = 0$, the ground-state configuration of plaquette fluxes can be determined analytically from symmetry. First, Lieb's lemma on reflection positivity [51–55] implies that, in the ground state, the gauge variables \hat{u}_{jk} lying on either side of a mirror line are related by reflection, up to gauge transformations. Since our model is reflection symmetric with respect to *any* bond-cutting mirror line for *any* choice of parameters J_α (Fig. 1b), we can consider each plaquette separately.

Given a plaquette, we select one of the reflection symmetries and denote by j' the image of site j under that reflection. We can always choose a gauge where $u_{j'j} = +1$ for the bonds crossing the mirror line (dashed geodesics in Fig. 1b). Then, Lieb's lemma implies that the remaining reflection-related bonds satisfy $u_{jk} = u_{k'j'}$. Indeed, under reflection symmetry the term $u_{jk} i\hat{c}_j \hat{c}_k$ is mapped to $u_{jk} (-i)\hat{c}_{j'} \hat{c}_{k'} = u_{jk} i\hat{c}_{k'} \hat{c}_{j'}$ (reflection is represented antiunitarily for Majorana fermions). Thus, for a $\{p, 3\}$ lattice with p even,

$$W_P = (-i)^p \cdot (-1) \cdot 1^{p/2-1} = -(-1)^{p/2}, \quad (3)$$

where $(-i)^p$ follows from the definition of W_P , (-1) from the opposite orientation (relative to the oriented Wilson loop) of the two bonds cut by the mirror line, and the remaining $(p/2-1)$ reflection-related pairs of bonds each have equal orientation. Unlike in the case of the coloring studied traditionally [49], Eq. (3) applies for any choice of couplings J_α .

The honeycomb ($\{6, 3\}$) lattice has $p/2 = 3$, such that $W_P = +1$, while in our example, $p/2 = 4$, thus the ground state has homogeneous π -flux ($W_P = -1$). By further exploring all $2^{6-1} = 32$ possible translation-invariant flux configurations on the infinite $\{8, 3\}$ lattice, we find that, in agreement with Eq. (3), the homogeneous π -flux configuration results in the lowest many-fermion ground-state energy [58]. For concreteness, we subsequently focus on the $\{8, 3\}$ lattice.

Fermionic spectrum.—Having determined the ground-state flux sector, we next study the spectrum of fermionic excitations as a function of the couplings J_α . The relevant quadratic Majorana Hamiltonian $\hat{\mathcal{H}} = \sum_{j,k} A_{jk} i\hat{c}_j \hat{c}_k$ possesses hyperbolic translation symmetry, thus we diagonalize it using HBT [11–13]. To capture the non-Abelian Bloch states [12] characteristic of hyperbolic reciprocal space, we generalize the supercell method [13] to quadratic Majorana Hamiltonians [58]. We use a coherent sequence [13, 25, 26] of five supercells containing up to 2048 sites, obtained from HYPERCELLS [13, 61–63], and perform random sampling of momenta [58] using HYPERBLOCH [64]. From the fermionic spectrum, we deduce the DOS $\rho(E)$ and corresponding spectral gap ΔE . To complement the supercell method based on HBT, we additionally compute $\rho(E)$ at selected points in the phase diagram using

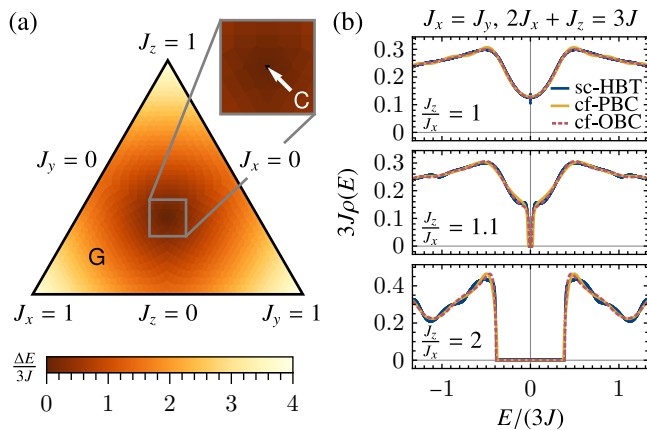


FIG. 2. (a) Phase diagram of the spectral gap ΔE for $K=0$ in the plane $J_x+J_y+J_z=3J$. Inset: region near the isotropic point ($J_x=J_y=J_z=J$) where the gap vanishes (black), distinguishing compressible (C) and gapped (G) spin-liquid phases. (b) Low-energy fermionic DOS (top) at the isotropic point, (middle) slightly away from it, and (bottom) deep in the anisotropic region, calculated using the supercell method (sc-HBT; 2048 sites) and the continued-fraction method applied to clusters with periodic (cf-PBC) and to flakes with open boundary conditions (cf-OBC) with $\sim 10^8$ sites.

the real-space continued-fraction method [24, 65, 66] on PBC clusters and finite flakes with open boundary conditions (OBC) containing $\sim 10^8$ sites [58].

Compressible spin liquid.—We first consider the case $K=0$. The ΔE phase diagram in Fig. 2a shows a gapless phase (C) at the isotropic point $J_x=J_y=J_z$ (see inset and also SM [58]) and a gapped phase away from it (G). Representative DOS computed from different methods are in excellent agreement (Fig. 2b). Resembling the case of an analogous edge coloring on the honeycomb lattice [67], a gap develops for small deviations from the isotropic point. However, the gapless phase C shows a finite DOS at $E=0$ in sharp contrast to the linearly vanishing DOS $\rho(E) \propto |E|$ associated with the Dirac spectrum on the honeycomb lattice [49]. Thus, unlike Kitaev’s Dirac spin liquid, the $\{8, 3\}$ HKM realizes a *compressible* spin liquid. Crucially, Abelian HBT alone incorrectly predicts a vanishing DOS $\rho(E) \propto |E|^3$ at low energies arising from conical singularities in the 4D Brillouin zone of Abelian Bloch states. However, the latter only capture particular slices through the full reciprocal space which is dominated by non-Abelian Bloch states [18]. Thus, finite compressibility here is a direct consequence of non-Abelian Bloch physics, which is absent for Euclidean lattices. Similar phenomenology, where non-Abelian Bloch states drastically alter the low-energy DOS, has been observed in Ref. 34.

\mathbb{Z}_2 spin liquid.—To better understand the nature of the gapped (G) phase away from the isotropic point, we study the HKM in the limit of extreme coupling anisotropy, $J_x, J_y \ll J_z$, where the fermion gap $\Delta E/(3J) \approx 4$ (Fig. 2a). When $J_x=J_y=0$, the model reduces to decoupled Ising dimers on z -bonds, each of which minimizes its energy by adopting one of two ferromagnetic configurations ($\uparrow\uparrow$ or $\downarrow\downarrow$), resulting in a macroscopic ground-state degeneracy. This degeneracy is

lifted at small but nonzero J_x, J_y , and the nature and spectrum of the resulting low-energy excitations can be determined from an effective Hamiltonian obtained by degenerate perturbation theory [49, 68, 69]. We first find that the HKM on the $\{8, 3\}$ lattice maps exactly onto a model of effective spin-1/2 degrees of freedom and hardcore bosons on the Archimedean $(8, 4, 8, 4)$ lattice [58]. The latter is the lattice obtained by collapsing the z -bond dimers into effective sites, and contains alternating square (\square) and octagonal (\circ) plaquettes. The spin states represent the two ferromagnetic configurations of each dimer, and bosons correspond to excitations out of the low-energy ferromagnetic subspace, with large energy cost $\Delta E/2 \approx 2J_z$.

To focus on the low-energy physics, we project onto the zero-boson subspace, and obtain the effective spin-1/2 Hamiltonian:

$$\hat{H}_{\text{eff}} = \frac{5}{16} \frac{J_{\parallel}^4}{J_z^3} \sum_{\square} \hat{W}_{\square} + \frac{429}{2048} \frac{J_{\parallel}^8}{J_z^7} \sum_{\circ} \hat{W}_{\circ}, \quad (4)$$

where \hat{W} are Wilson loop operators on the $(8, 4, 8, 4)$ lattice, and we have set $J_x=J_y=J_{\parallel}$ here for simplicity [58]. The \hat{W} operators all commute with each other, and are in fact equivalent to the plaquette operators \hat{W}_P introduced earlier. Thus, the positive couplings in Eq. (4) imply that $\hat{W}_P = -1$ in the ground state, consistent with the exact result Eq. (3). Second, Eq. (4) implies that the lowest-energy excitation is a \mathbb{Z}_2 vortex with $\hat{W}_{\circ} = +1$ and energy cost $\sim J_{\parallel}^8/J_z^7$, much less than the fermion gap $\Delta E/2 \approx 2J_z$ in that limit. Finally, the effective model (4) can be further mapped [58] to a hyperbolic analog of the toric code [70] on the $\{8, 4\}$ lattice, i.e., a hyperbolic surface code [71–76]. This last mapping reveals that the \square and \circ vortices obey bosonic self-statistics but are mutual semions, establishing that the G phase is a topologically ordered \mathbb{Z}_2 spin liquid [77].

Chiral spin liquid.—A different type of gapped spin liquid is obtained when the emergent Majorana fermions carry a nonzero Chern number. This requires time-reversal symmetry to be broken, which occurs here for $K \neq 0$. Focusing first on the isotropic point, where for $K=0$ the fermionic spectrum is gapless, a gap opens at infinitesimal $K \neq 0$ and subsequently increases with increasing K (Fig. 3c). Thus, for finite K , a new gapped phase χ develops around the isotropic point and remains separated from G by a circular gapless line in parameter space (Fig. 3a). From cuts through the phase diagram for different values of K (Fig. 3b), we find that the χ region expands with increasing K .

The Chern number C determines the properties of anyonic excitations as well as the existence and character of topologically protected boundary modes [49]. While in Euclidean translation-invariant systems, C can be easily computed in momentum space, we rely here on a real-space formulation [49, 58] and compute it on finite PBC clusters (Fig. 4a). Comparing the result to Fig. 3a, the χ phase around the isotropic point has odd Chern number $C = -1$, establishing it as a chiral spin liquid with non-Abelian anyons [49], while C vanishes in the \mathbb{Z}_2 spin liquid (G) phase.

Finally, the nonzero Chern number suggests gapless chiral edge modes, which we investigate in an OBC disk-shaped

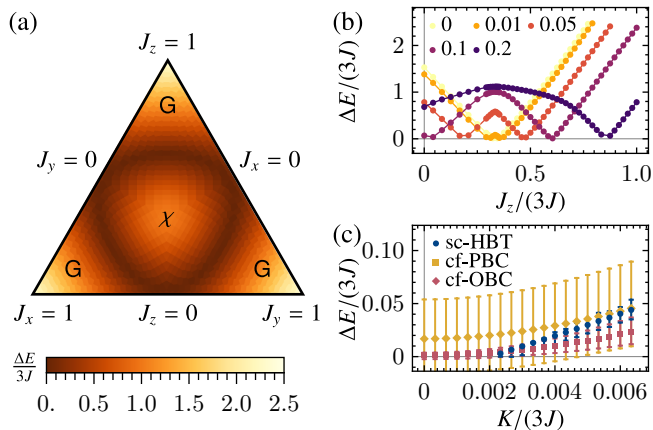


FIG. 3. (a) Phase diagram for $K/(3J) = 0.1$, showing chiral (χ) and \mathbb{Z}_2 (G) spin liquid phases separated by a phase transition (dark brown). (b) Vertical cut through the phase diagram in (a) for different values of $K/(3J)$, with $J_x = J_y = (3J - J_z)/2$. (c) Gap ΔE vs K at the isotropic point $J_x = J_y = J_z = J$ obtained using the three methods (see Fig. 2 caption).

flake at the isotropic point. For a sufficiently large flake, an approximate continuous rotation symmetry emerges on the edge, allowing us to introduce an approximate angular momentum quantum number ℓ [58]. In Fig. 4b, we show the corresponding angular dispersion together with a measure p_{edge} of edge localization defined as the integrated probability density within the outer 10% of the hyperbolic radius of the flake [58]. Bulk modes (blue) generally do not have sharp angular momentum, but a branch of states sharply peaked at a single ℓ and strongly localized on the edge (red) crosses the bulk gap; we identify it with the single dispersive band of chiral edge states expected for the $C = -1$ topology. In contrast to Euclidean lattices, there is an extensive number of such edge states due to the finite boundary-to-bulk ratio in hyperbolic geometry.

For edge modes described by a chiral Majorana conformal field theory with chiral central charge $c_- = 1/2$, we expect a linear low-energy angular dispersion $E \propto \ell$ with half-integer quantization $\ell \in \mathbb{Z} + \frac{1}{2}$ [78, 79]. The inset in Fig. 4b (red dots) confirms this expectation, notably the absence of a zero-energy mode with $\ell = 0 \notin \mathbb{Z} + \frac{1}{2}$. Inserting a vortex through the center of the disk binds a Majorana zero mode there, shifts ℓ by $1/2$ such that $\ell \in \mathbb{Z}$ [78, 79], and induces a second zero-energy mode on the boundary (red crosses in the inset).

Conclusion.—In summary, we introduced for the first time an exactly solvable model of strongly correlated hyperbolic quantum matter, the hyperbolic Kitaev model (HKM). The non-Euclidean space-group symmetries of hyperbolic lattices play a crucial role in the model’s construction and solution. In contrast to previous non-crystalline extensions of the Kitaev model, reflection symmetries across geodesics enable an exact analytical determination of the ground-state flux sector via Lieb’s lemma, and noncommutative translation symmetries allow for an efficient determination of thermodynamic-limit properties via hyperbolic band theory. Our detailed study of the HKM on the $\{8, 3\}$ lattice reveals both Abelian and non-Abelian gapped topological spin liquids, as well as a gap-

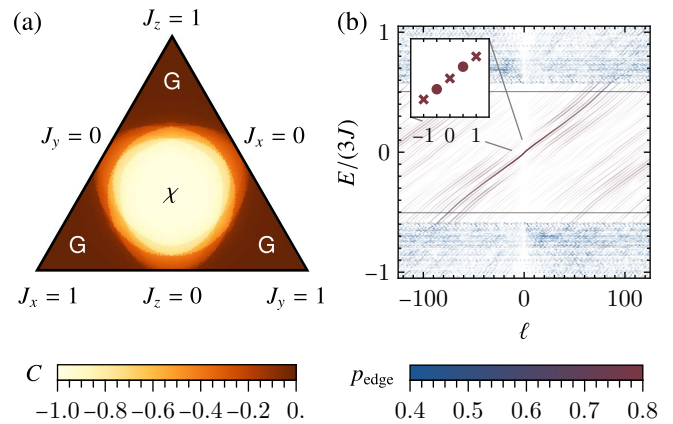


FIG. 4. (a) Phase diagram of the Chern number C for $K/(3J) = 0.1$ computed on a PBC cluster (2048 sites). Phases χ and G (compare Fig. 3a) show constant integer C away from the transition. (b) Energy E vs angular momentum ℓ for $J_x = J_y = J_z = J$, $K/(3J) = 0.1$, computed on an OBC disk (896 sites). Color encodes the degree of edge localization p_{edge} , and opacity the weight of the corresponding ℓ . Inset: $\ell \in \mathbb{Z} + \frac{1}{2}$ (red dots) at low energies without a vortex, and $\ell \in \mathbb{Z}$ (red crosses) with a \mathbb{Z}_2 vortex at the center of the disk (including a perturbation to prevent hybridization [58]).

less spin liquid that, unlike Kitaev’s Dirac spin liquid, has a compressible (finite) low-energy DOS dominated by Majorana non-Abelian Bloch states, a unique feature of hyperbolic space.

Our work opens several vistas for future study. On the theoretical side, given the degree of analytical control the HKM affords, one should investigate whether the bulk hyperbolic spin liquids found here realize interesting “holographic spin liquids” on the edge [80–84]. Unlike Kitaev’s (unique) honeycomb lattice in 2D, infinitely many $\{p, 3\}$ lattices are now open to investigation, as well as other possible extensions of Kitaev physics [85–89]. On the experimental side, the spin-spin interactions in Eq. (1) could potentially be realized via qubit-photon interactions [90] in circuit quantum electrodynamics [2]. For applications to quantum error correction, implementing a two-spin interaction in the anisotropic coupling limit $J_z \gg J_x, J_y$ might represent a simpler path towards hyperbolic surface codes than directly engineering the requisite multi-spin interactions [71, 72].

Acknowledgments.—We thank Igor Boettcher for many insightful conversations and suggestions over the course of this project, as well as Marin Bukov, Felix Duset, Juraj Hašík, Tobias Hofmann, Bastien Lapiere, Jiří Minář, Benedikt Placke, G. Shankar, Ronny Thomale, and Götz S. Uhrig for valuable discussions. P. M. L. acknowledges support by the European Union (ERC, QuSimCtrl, 101113633). Views and opinions expressed are however those of the authors only and do not necessarily reflect those of the European Union or the European Research Council Executive Agency. Neither the European Union nor the granting authority can be held responsible for them. S. D. was supported by the Faculty of Science at the University of Alberta. T. B. was supported by the Starting Grant No. 211310 by the Swiss National Science Foundation (SNSF). J. M. was supported by NSERC Discovery Grants

#RGPIN-2020-06999 and #RGPAS-2020-00064; the Canada Research Chair (CRC) Program; and Alberta Innovates. This research was enabled in part by support provided by the Digital Research Alliance of Canada (alliancecan.ca).





Note added. While finalizing this manuscript, we became aware of an independent work [91] studying the Kitaev model on the $\{9, 3\}$ lattice, where the authors identify a gapless chiral \mathbb{Z}_2 spin liquid.

-
- [1] S. Sachdev, *Quantum Phases of Matter* (Cambridge University Press, Cambridge, 2023).
- [2] A. J. Kollár, M. Fitzpatrick, and A. A. Houck, Hyperbolic lattices in circuit quantum electrodynamics, *Nature* **571**, 45 (2019).
- [3] P. M. Lenggenhager, A. Stegmaier, L. K. Upreti, T. Hofmann, T. Helbig, A. Vollhardt, M. Greiter, C. H. Lee, S. Imhof, H. Brand, T. Kießling, I. Boettcher, T. Neupert, R. Thomale, and T. Bzdušek, Simulating hyperbolic space on a circuit board, *Nat. Commun.* **13**, 4373 (2022).
- [4] A. Chen, H. Brand, T. Helbig, T. Hofmann, S. Imhof, A. Fritzsche, T. Kießling, A. Stegmaier, L. K. Upreti, T. Neupert, T. Bzdušek, M. Greiter, R. Thomale, and I. Boettcher, Hyperbolic matter in electrical circuits with tunable complex phases, *Nat. Commun.* **14**, 622 (2023).
- [5] W. Zhang, H. Yuan, N. Sun, H. Sun, and X. Zhang, Observation of novel topological states in hyperbolic lattices, *Nat. Commun.* **13**, 2937 (2022).
- [6] W. Zhang, F. Di, X. Zheng, H. Sun, and X. Zhang, Hyperbolic band topology with non-trivial second Chern numbers, *Nat. Commun.* **14**, 1083 (2023).
- [7] L. Huang, L. He, W. Zhang, H. Zhang, D. Liu, X. Feng, F. Liu, K. Cui, Y. Huang, W. Zhang, and X. Zhang, Hyperbolic photonic topological insulators, *Nat. Commun.* **15**, 1647 (2024).
- [8] Q. Chen, Z. Zhang, H. Qin, A. Bossart, Y. Yang, H. Chen, and R. Fleury, Anomalous and Chern topological waves in hyperbolic networks, *Nat. Commun.* **15**, 2293 (2024).
- [9] N. Balazs and A. Voros, Chaos on the pseudosphere, *Phys. Rep.* **143**, 109 (1986).
- [10] I. Boettcher, P. Bienias, R. Belyansky, A. J. Kollár, and A. V. Gorshkov, Quantum simulation of hyperbolic space with circuit quantum electrodynamics: From graphs to geometry, *Phys. Rev. A* **102**, 032208 (2020).
- [11] J. Maciejko and S. Rayan, Hyperbolic band theory, *Sci. Adv.* **7**, eabe9170 (2021).
- [12] J. Maciejko and S. Rayan, Automorphic Bloch theorems for hyperbolic lattices, *Proc. Natl. Acad. Sci. U.S.A.* **119**, e2116869119 (2022).
- [13] P. M. Lenggenhager, J. Maciejko, and T. Bzdušek, Non-Abelian hyperbolic band theory from supercells, *Phys. Rev. Lett.* **131**, 226401 (2023).
- [14] N. Cheng, F. Serafin, J. McInerney, Z. Rocklin, K. Sun, and X. Mao, Band theory and boundary modes of high-dimensional representations of infinite hyperbolic lattices, *Phys. Rev. Lett.* **129**, 088002 (2022).
- [15] E. Kienzle and S. Rayan, Hyperbolic band theory through Higgs bundles, *Adv. Math.* **409**, 108664 (2022).
- [16] Á. Nagy and S. Rayan, On the Hyperbolic Bloch Transform, *Ann. Henri Poincaré* (2023).
- [17] A. Attar and I. Boettcher, Selberg trace formula in hyperbolic band theory, *Phys. Rev. E* **106**, 034114 (2022).
- [18] G. Shankar and J. Maciejko, Hyperbolic lattices and two-dimensional Yang-Mills theory, [arXiv:2309.03857](https://arxiv.org/abs/2309.03857) (2023).
- [19] I. Boettcher, A. V. Gorshkov, A. J. Kollár, J. Maciejko, S. Rayan, and R. Thomale, Crystallography of hyperbolic lattices, *Phys. Rev. B* **105**, 125118 (2022).
- [20] A. Chen, Y. Guan, P. M. Lenggenhager, J. Maciejko, I. Boettcher, and T. Bzdušek, Symmetry and topology of hyperbolic Haldane models, *Phys. Rev. B* **108**, 085114 (2023).
- [21] A. J. Kollár, M. Fitzpatrick, P. Sarnak, and A. A. Houck, Line-graph lattices: Euclidean and non-Euclidean flat bands, and implementations in circuit quantum electrodynamics, *Commun. Math. Phys.* **376**, 1909 (2020).
- [22] T. Bzdušek and J. Maciejko, Flat bands and band-touching from real-space topology in hyperbolic lattices, *Phys. Rev. B* **106**, 155146 (2022).
- [23] R. Mosseri, R. Vogeler, and J. Vidal, Aharonov-Bohm cages, flat bands, and gap labeling in hyperbolic tilings, *Phys. Rev. B* **106**, 155120 (2022).
- [24] R. Mosseri and J. Vidal, Density of states of tight-binding models in the hyperbolic plane, *Phys. Rev. B* **108**, 035154 (2023).
- [25] F. R. Lux and E. Prodan, Spectral and Combinatorial Aspects of Cayley-Crystals, *Ann. Henri Poincaré* **10.1007/s00023-023-01373-3** (2023).
- [26] F. R. Lux and E. Prodan, Converging periodic boundary conditions and detection of topological gaps on regular hyperbolic tessellations, *Phys. Rev. Lett.* **131**, 176603 (2023).
- [27] S. Yu, X. Piao, and N. Park, Topological hyperbolic lattices, *Phys. Rev. Lett.* **125**, 053901 (2020).
- [28] Z.-R. Liu, C.-B. Hua, T. Peng, and B. Zhou, Chern insulator in a hyperbolic lattice, *Phys. Rev. B* **105**, 245301 (2022).
- [29] D. M. Urwyler, P. M. Lenggenhager, I. Boettcher, R. Thomale, T. Neupert, and T. Bzdušek, Hyperbolic topological band insulators, *Phys. Rev. Lett.* **129**, 246402 (2022).
- [30] Z.-R. Liu, C.-B. Hua, T. Peng, R. Chen, and B. Zhou, Higher-order topological insulators in hyperbolic lattices, *Phys. Rev. B* **107**, 125302 (2023).
- [31] Y.-L. Tao and Y. Xu, Higher-order topological hyperbolic lattices, *Phys. Rev. B* **107**, 184201 (2023).
- [32] Q. Pei, H. Yuan, W. Zhang, and X. Zhang, Engineering boundary-dominated topological states in defective hyperbolic lattices, *Phys. Rev. B* **107**, 165145 (2023).
- [33] H. Yuan, W. Zhang, Q. Pei, and X. Zhang, Hyperbolic topological flat bands, *Phys. Rev. B* **109**, L041109 (2024).
- [34] T. Tummuru, A. Chen, P. M. Lenggenhager, T. Neupert, J. Maciejko, and T. Bzdušek, Hyperbolic non-Abelian semimetal, *Phys. Rev. Lett.* **132**, 206601 (2024).
- [35] C. Sun, A. Chen, T. Bzdušek, and J. Maciejko, Topological linear response of hyperbolic Chern insulators, [arXiv:2406.08388](https://arxiv.org/abs/2406.08388) (2024).
- [36] C. Lv, R. Zhang, Z. Zhai, and Q. Zhou, Curving the space by non-Hermiticity, *Nat. Commun.* **13**, 2184 (2022).
- [37] J. Sun, C.-A. Li, S. Feng, and H. Guo, Hybrid higher-order skin-topological effect in hyperbolic lattices, *Phys. Rev. B* **108**, 075122 (2023).
- [38] K. Ikeda, S. Aoki, and Y. Matsuki, Hyperbolic band theory under magnetic field and Dirac cones on a higher genus surface, *J. Phys.: Condens. Matter* **33**, 485602 (2021).
- [39] A. Stegmaier, L. K. Upreti, R. Thomale, and I. Boettcher, Universality of Hofstadter Butterflies on Hyperbolic Lattices, *Phys. Rev. Lett.* **128**, 166402 (2022).
- [40] J. B. Curtis, P. Narang, and V. Galitski, Absence of Weak Localization on Negative Curvature Surfaces, [arXiv:2308.01351](https://arxiv.org/abs/2308.01351) (2023).

- [41] A. Chen, J. Maciejko, and I. Boettcher, Anderson localization transition in disordered hyperbolic lattices, [arXiv:2310.07978](https://arxiv.org/abs/2310.07978) (2023).
- [42] T. Li, Y. Peng, Y. Wang, and H. Hu, Anderson transition and mobility edges on hyperbolic lattices, [arXiv:2312.11857](https://arxiv.org/abs/2312.11857) (2023).
- [43] M. Daniška and A. Gendiar, Analysis of quantum spin models on hyperbolic lattices and Bethe lattice, *J. Phys. A: Math. Theor.* **49**, 145003 (2016).
- [44] M. Daniška and A. Gendiar, Study of classical and quantum phase transitions on non-Euclidean geometries in higher dimensions, *Acta Phys. Slovaca* **68**, 187 (2018).
- [45] A. Götz, G. Rein, J. C. Inácio, and F. F. Assaad, Hubbard and Heisenberg models on hyperbolic lattices – Metal-insulator transitions, global antiferromagnetism and enhanced boundary fluctuations, [arXiv:2406.03416](https://arxiv.org/abs/2406.03416) (2024).
- [46] X. Zhu, J. Guo, N. P. Breuckmann, H. Guo, and S. Feng, Quantum phase transitions of interacting bosons on hyperbolic lattices, *J. Phys.: Condens. Matter* **33**, 335602 (2021).
- [47] N. Glusceovich, A. Samanta, S. Manna, and B. Roy, Dynamic mass generation on two-dimensional electronic hyperbolic lattices, [arXiv:2302.04864](https://arxiv.org/abs/2302.04864) (2023).
- [48] N. Glusceovich and B. Roy, Magnetic catalysis in weakly interacting hyperbolic Dirac materials, [arXiv:2305.11174](https://arxiv.org/abs/2305.11174) (2023).
- [49] A. Kitaev, Anyons in an exactly solved model and beyond, *Ann. Phys.* **321**, 2 (2006).
- [50] L. Stockmeyer, Planar 3-colorability is polynomial complete, *ACM SIGACT News* **5**, 19 (1973).
- [51] E. H. Lieb, Flux phase of the half-filled band, *Phys. Rev. Lett.* **73**, 2158 (1994).
- [52] E. H. Lieb and M. Loss, Fluxes, Laplacians, and Kasteleyn's theorem, *Duke Math. J.* **71**, 337 (1993).
- [53] N. Macris and B. Nachtergaele, On the flux phase conjecture at half-filling: An improved proof, *J. Stat. Phys.* **85**, 745 (1996).
- [54] A. Jaffe and F. L. Pedrocchi, Reflection positivity for Majoranas, *Ann. Henri Poincaré* **16**, 189 (2015).
- [55] S. Chesi, A. Jaffe, D. Loss, and F. L. Pedrocchi, Vortex loops and Majoranas, *J. Math. Phys.* **54**, 112203 (2013).
- [56] G. Cassella, P. d'Ornellas, T. Hodson, W. M. H. Natori, and J. Knolle, An exact chiral amorphous spin liquid, *Nat. Commun.* **14**, 6663 (2023).
- [57] S. Kim, M. Saad, D. Mao, A. Agarwala, and D. Chowdhury, Quasicrystalline spin liquid, [arXiv:2402.07971](https://arxiv.org/abs/2402.07971) (2024).
- [58] See Supplemental Material, which cites additional Refs. 92–114, for further information on the 3-edge coloring, the Majorana representation, hyperbolic band theory for Majorana fermions, the numerical methods, the energy in different flux sectors, the gapped \mathbb{Z}_2 spin liquid, and the chiral edge states.
- [59] B.-Y. Sun, N. Goldman, M. Aidelsburger, and M. Bukov, Engineering and probing non-Abelian chiral spin liquids using periodically driven ultracold atoms, *PRX Quantum* **4**, 020329 (2023).
- [60] R. Diestel, *Graph Theory*, 5th ed. (Springer, Berlin, 2017).
- [61] P. M. Lenggenhager, J. Maciejko, and T. Bzdušek, *HyperCells: A GAP package for constructing primitive cells and supercells of hyperbolic lattices* (2023), <https://github.com/patrick-lenggenhager/HyperCells>.
- [62] P. M. Lenggenhager, *Emerging avenues in band theory: multi-gap topology and hyperbolic lattices*, Ph.D. thesis, ETH Zurich (2023).
- [63] M. Conder, Quotients of triangle groups acting on surfaces of genus 2 to 101, <https://www.math.auckland.ac.nz/~conder/TriangleGroupQuotients101.txt> (2007).
- [64] P. M. Lenggenhager, J. Maciejko, and T. Bzdušek, *HyperBloch: A Mathematica package for hyperbolic tight-binding models and the supercell method* (2023), <https://github.com/patrick-lenggenhager/HyperBloch>.
- [65] R. Haydock, V. Heine, and M. J. Kelly, Electronic structure based on the local atomic environment for tight-binding bands, *J. Phys. C* **5**, 2845 (1972).
- [66] R. Haydock, V. Heine, and M. J. Kelly, Electronic structure based on the local atomic environment for tight-binding bands. II, *J. Phys. C* **8**, 2591 (1975).
- [67] M. Kamfor, S. Dusuel, J. Vidal, and K. P. Schmidt, Kitaev model and dimer coverings on the honeycomb lattice, *J. Stat. Mech.* **2010**, P08010 (2010).
- [68] J. Vidal, K. P. Schmidt, and S. Dusuel, Perturbative approach to an exactly solved problem: Kitaev honeycomb model, *Phys. Rev. B* **78**, 245121 (2008).
- [69] K. P. Schmidt, S. Dusuel, and J. Vidal, Emergent Fermions and Anyons in the Kitaev Model, *Phys. Rev. Lett.* **100**, 057208 (2008).
- [70] A. Kitaev, Fault-tolerant quantum computation by anyons, *Ann. Phys.* **303**, 2 (2003).
- [71] N. P. Breuckmann and B. M. Terhal, Constructions and Noise Threshold of Hyperbolic Surface Codes, *IEEE Trans. Inf. Theory* **62**, 3731 (2016).
- [72] N. P. Breuckmann, C. Vuillot, E. Campbell, A. Krishna, and B. M. Terhal, Hyperbolic and semi-hyperbolic surface codes for quantum storage, *Quantum Sci. Technol.* **2**, 035007 (2017).
- [73] A. Lavasani, G. Zhu, and M. Barkeshli, Universal logical gates with constant overhead: instantaneous Dehn twists for hyperbolic quantum codes, *Quantum* **3**, 180 (2019).
- [74] A. Jahn and J. Eisert, Holographic tensor network models and quantum error correction: a topical review, *Quantum Sci. Technol.* **6**, 033002 (2021).
- [75] O. Higgott and N. P. Breuckmann, Constructions and performance of hyperbolic and semi-hyperbolic Floquet codes, [arXiv:2308.03750](https://arxiv.org/abs/2308.03750) (2023).
- [76] A. Fahimniya, H. Dehghani, K. Bharti, S. Mathew, A. J. Kollár, A. V. Gorshkov, and M. J. Gullans, Fault-tolerant hyperbolic Floquet quantum error correcting codes, [arXiv:2309.10033](https://arxiv.org/abs/2309.10033) (2023).
- [77] X. G. Wen, Mean-field theory of spin-liquid states with finite energy gap and topological orders, *Phys. Rev. B* **44**, 2664 (1991).
- [78] N. Read and D. Green, Paired states of fermions in two dimensions with breaking of parity and time-reversal symmetries and the fractional quantum Hall effect, *Phys. Rev. B* **61**, 10267 (2000).
- [79] M. Stone and R. Roy, Edge modes, edge currents, and gauge invariance in $p_x + ip_y$ superfluids and superconductors, *Phys. Rev. B* **69**, 184511 (2004).
- [80] M. Asaduzzaman, S. Catterall, J. Hubisz, R. Nelson, and J. Unmuth-Yockey, Holography on tessellations of hyperbolic space, *Phys. Rev. D* **102**, 034511 (2020).
- [81] R. C. Brower, C. V. Coburn, A. L. Fitzpatrick, D. Howarth, and C.-I. Tan, Lattice setup for quantum field theory in AdS_2 , *Phys. Rev. D* **103**, 094507 (2021).
- [82] P. Basteiro, G. Di Giulio, J. Erdmenger, J. Karl, R. Meyer, and Z.-Y. Xian, Towards explicit discrete holography: Aperiodic spin chains from hyperbolic tilings, *SciPost Phys.* **13**, 103 (2022).
- [83] J. Chen, F. Chen, Y. Yang, L. Yang, Z. Chen, Y. Meng, B. Yan, X. Xi, Z. Zhu, G.-G. Liu, P. P. Shum, H. Chen, R.-G. Cai, R.-Q. Yang, Y. Yang, and Z. Gao, AdS/CFT Correspondence in Hyperbolic Lattices, [arXiv:2305.04862](https://arxiv.org/abs/2305.04862) (2023).
- [84] S. Dey, A. Chen, P. Basteiro, A. Fritzsche, M. Greiter,

- M. Kaminski, P. M. Lenggenhager, R. Meyer, R. Sorbello, A. Stegmaier, R. Thomale, J. Erdmenger, and I. Boettcher, Simulating Holographic Conformal Field Theories on Hyperbolic Lattices, [arXiv:2404.03062](https://arxiv.org/abs/2404.03062) (2024).
- [85] H. Yao and S. A. Kivelson, Exact Chiral Spin Liquid with Non-Abelian Anyons, *Phys. Rev. Lett.* **99**, 247203 (2007).
- [86] H. Yao, S.-C. Zhang, and S. A. Kivelson, Algebraic Spin Liquid in an Exactly Solvable Spin Model, *Phys. Rev. Lett.* **102**, 217202 (2009).
- [87] C. Wu, D. Arovas, and H.-H. Hung, Γ -matrix generalization of the Kitaev model, *Phys. Rev. B* **79**, 134427 (2009).
- [88] M. Barkeshli, H.-C. Jiang, R. Thomale, and X.-L. Qi, Generalized Kitaev Models and Extrinsic Non-Abelian Twist Defects, *Phys. Rev. Lett.* **114**, 026401 (2015).
- [89] A. Vaezi, \mathbb{Z}_3 generalization of the Kitaev’s spin-1/2 model, *Phys. Rev. B* **90**, 075106 (2014).
- [90] P. Bienias, I. Boettcher, R. Belyansky, A. J. Kollár, and A. V. Gorshkov, Circuit Quantum Electrodynamics in Hyperbolic Space: From Photon Bound States to Frustrated Spin Models, *Phys. Rev. Lett.* **128**, 013601 (2022).
- [91] F. Dusel, T. Hofmann, and R. Thomale, Chiral hyperbolic spin liquids (unpublished).
- [92] D. J. S. Robinson, *A Course in the Theory of Groups*, 2nd ed. (Springer, New York, 1996).
- [93] GAP, *GAP – Groups, Algorithms, and Programming, Version 4.11.1*, The GAP Group (2021).
- [94] D. Singerman, Finitely Maximal Fuchsian Groups, *J. London Math. Soc.* **s2-6**, 29 (1972).
- [95] K. Takeuchi, Commensurability classes of arithmetic triangle groups, *J. Fac. Sci. Univ. Tokyo Sec. IA Math.* **24**, 201 (1977).
- [96] J. A. Todd and H. S. M. Coxeter, A practical method for enumerating cosets of a finite abstract group, *Proc. Edinburgh Math. Soc.* **5**, 26 (1936).
- [97] J. Neubüser, An elementary introduction to coset table methods in computational group theory, in *Groups - St Andrews 1981*, London Mathematical Society Lecture Note Series, edited by C. M. Campbell and E. F. Robertson (Cambridge University Press, Cambridge, 1982) pp. 1–45.
- [98] J. F. Humphreys, *A Course in Group Theory* (Oxford University Press, Oxford, 1996).
- [99] X. G. Wen, F. Wilczek, and A. Zee, Chiral spin states and superconductivity, *Phys. Rev. B* **39**, 11413 (1989).
- [100] F. L. Pedrocchi, S. Chesi, and D. Loss, Physical solutions of the Kitaev honeycomb model, *Phys. Rev. B* **84**, 165414 (2011).
- [101] F. D. M. Haldane, Model for a quantum Hall effect without Landau levels: Condensed-matter realization of the “parity anomaly”, *Phys. Rev. Lett.* **61**, 2015 (1988).
- [102] P. M. Lenggenhager, S. Dey, T. Bzdušek, and J. Maciejko, Supplementary data and code for Hyperbolic Spin Liquids (2024), (to be released).
- [103] J. P. Gaspard and F. Cyrot-Lackmann, Density of states from moments. Application to the impurity band, *J. Phys. C* **6**, 3077 (1973).
- [104] P. Turchi, F. Ducastelle, and G. Tréglia, Band gaps and asymptotic behaviour of continued fraction coefficients, *J. Phys. C* **15**, 2891 (1982).
- [105] C. Knetter and G. Uhrig, Perturbation theory by flow equations: dimerized and frustrated $S = 1/2$ chain, *Eur. Phys. J. B* **13**, 209 (2000).
- [106] B. Grünbaum and G. C. Shephard, *Tilings and Patterns* (Freeman, New York, 1987).
- [107] A. W. Sandvik, Computational Studies of Quantum Spin Systems, *AIP Conf. Proc.* **1297**, 135 (2010).
- [108] J. G. Wright and B. S. Shastry, DiracQ: A Quantum Many-Body Physics Package, [arXiv:1301.4494](https://arxiv.org/abs/1301.4494) (2013).
- [109] X.-G. Wen, Quantum Orders in an Exact Soluble Model, *Phys. Rev. Lett.* **90**, 016803 (2003).
- [110] H. Ebisu and B. Han, \mathbb{Z}_2 topologically ordered phases on a simple hyperbolic lattice, *Phys. Rev. Research* **4**, 043099 (2022).
- [111] H. Yan, Hyperbolic fracton model, subsystem symmetry, and holography, *Phys. Rev. B* **99**, 155126 (2019).
- [112] H. Yan, K. Slagle, and A. H. Nevidomskyy, Y-cube model and fractal structure of subdimensional particles on hyperbolic lattices, [arXiv:2211.15829](https://arxiv.org/abs/2211.15829) (2022).
- [113] H. Yan, C. B. Jepsen, and Y. Oz, p -adic Holography from the Hyperbolic Fracton Model, [arXiv:2306.07203](https://arxiv.org/abs/2306.07203) (2023).
- [114] N. P. Mitchell, L. M. Nash, D. Hexner, A. M. Turner, and W. T. M. Irvine, Amorphous topological insulators constructed from random point sets, *Nat. Phys.* **14**, 380 (2018).

Supplemental Material for: Hyperbolic Spin Liquids

Patrick M. Lenggenhager ^{1,*} Santanu Dey ² Tomáš Bzdušek ³ and Joseph Maciejko ^{2,4,†}

¹Max Planck Institute for the Physics of Complex Systems, Nöthnitzer Str. 38, 01187 Dresden, Germany

²Department of Physics, University of Alberta, Edmonton, Alberta T6G 2E1, Canada

³Department of Physics, University of Zürich, Winterthurerstrasse 190, 8057 Zürich, Switzerland

⁴Theoretical Physics Institute & Quantum Horizons Alberta,
University of Alberta, Edmonton, Alberta T6G 2E1, Canada

(Dated: July 16, 2024)

CONTENTS

I. Symmetric 3-edge coloring on hyperbolic $\{2m, 3\}$ lattices	2
A. 3-edge coloring from space-group symmetries	2
B. Symmetric Bravais unit cells	4
C. Useful mathematical results	5
II. Hyperbolic Kitaev model	9
A. Time-reversal-breaking term	9
B. Majorana representation	10
III. Hyperbolic band theory for Majorana Hamiltonians	12
IV. The supercell method	14
A. Supercell sequence and state sampling	14
B. Model definition	16
C. Many-body ground-state energy	18
D. Density of states	19
E. Spectral gap in the thermodynamic limit	19
V. The continued-fraction method	20
A. Clusters with open boundary conditions (OBC)	21
B. Clusters with periodic boundary conditions (PBC)	21
C. The continued-fraction method	22
VI. Ground-state flux sector	24
VII. Fermionic spectrum in the homogeneous π -flux sector	26
A. Gapping by anisotropy	26
B. Gapping by time-reversal-symmetry breaking	26
VIII. Gapped \mathbb{Z}_2 spin liquid in the anisotropic coupling limit	27
A. Mapping to spin-boson model on $(8, 4, 8, 4)$ lattice	27
B. Effective Hamiltonian from perturbation theory	29
C. Hyperbolic $\{8, 4\}$ surface code and anyonic excitations	29
IX. Real-space Chern number	32
X. Chiral edge states	34

* plengg@pks.mpg.de

† maciejko@ualberta.ca

I. SYMMETRIC 3-EDGE COLORING ON HYPERBOLIC $\{2m, 3\}$ LATTICES

In this section, we describe a systematic procedure to construct a symmetry-compatible 3-edge coloring for hyperbolic $\{p, 3\}$ lattices with even $p = 2m$. To define an exactly solvable Kitaev model on a graph, one must first ensure the graph admits a 3-edge coloring, that is, a coloring of edges with at most three colors such that no two edges with a common vertex have the same color. Infinite $\{2m, 3\}$ lattices are bipartite graphs, for which König's theorem ensures they are 3-edge colorable [60]. However, an arbitrary 3-edge coloring does not generically exhibit the infinitely many reflection symmetries that are necessary to unambiguously determine the \mathbb{Z}_2 flux in each plaquette via Lieb's lemma (see main text). Here, we utilize the space-group symmetries of the $\{2m, 3\}$ lattice to construct a 3-edge coloring¹ that exhibits infinitely many reflection symmetries (Section IA), allowing for a complete determination of the ground-state flux in every plaquette. We also determine a sufficient condition on the translation group Γ for the corresponding Bravais unit cell to respect those same symmetries (Section IB). Throughout this section, we make frequent use of various mathematical results collected in Section IC.

A. 3-edge coloring from space-group symmetries

The space group G of the infinite $\{2m, 3\}$ lattice is the hyperbolic triangle group $\Delta(2, 3, 2m)$, an infinite discrete group defined by the presentation

$$G \equiv \Delta(2, 3, 2m) = \langle a, b, c | a^2, b^2, c^2, (ab)^2, (bc)^3, (ca)^{2m} \rangle. \quad (\text{S1})$$

In general, one defines the triangle group $\Delta(r, q, p) = \langle a, b, c | a^2, b^2, c^2, (ab)^r, (bc)^q, (ca)^p \rangle$. For $\frac{1}{r} + \frac{1}{q} + \frac{1}{p} < 1$, as is the case here, this is the symmetry group of a regular tiling of the Poincaré disk \mathbb{D} by hyperbolic triangles with interior angles $\frac{\pi}{r}, \frac{\pi}{q}, \frac{\pi}{p}$. The generators a, b, c are reflections with respect to the sides of a reference triangle (highlighted with thick solid edges near the center of Fig. S1), which is repeated under the action of $\Delta(2, 3, 2m)$ to tessellate the entire Poincaré disk. The composite operations $x \equiv ab$, $y \equiv bc$, $z \equiv ca$ are respectively counterclockwise rotations by $\frac{2\pi}{2} = \pi$, $\frac{2\pi}{3}$, $\frac{2\pi}{2m} = \frac{\pi}{m}$ about the vertices (correspondingly labeled v_x, v_y, v_z) of the reference triangle.

To construct a 3-edge coloring, we first observe that the edges of the $\{2m, 3\}$ lattice (open circles in Fig. S1) are in one-to-one correspondence with all images of the vertex $v_x \in \mathbb{D}$ under the action of G , which we simply call “ x -vertices”. Formally, the set of all x -vertices is the orbit $v_x \cdot G$ where we define a right action of $G < \text{PSU}(1, 1)$ on \mathbb{D} as:

$$z \cdot g \equiv \frac{\alpha^* z - \beta}{-\beta^* z + \alpha}, \quad g \in G, \quad z \in \mathbb{D}, \quad (\text{S2})$$

which obeys $(z \cdot g) \cdot g' = z \cdot (gg')$. Here we have used the representation of an element $g \in \Delta(2, 3, 2m)$ as an $\text{SU}(1, 1)$ matrix $\begin{pmatrix} \alpha & \beta \\ \beta^* & \alpha^* \end{pmatrix}$ with $|\alpha|^2 - |\beta|^2 = 1$. According to the orbit-stabilizer theorem, the orbit $v_x \cdot G$ is in one-to-one correspondence with the right coset space $H \backslash G$, where $H < G$ is the stabilizer of v_x in G :

$$H \equiv G_{v_x} = \{h \in G : v_x \cdot h = v_x\}. \quad (\text{S3})$$

Geometrically, H is the set of elements of the space group G that leave v_x invariant. Inspecting Fig. S1, we see that H is generated by the reflections a and b that pass through v_x , and thus inherits from G the following presentation:

$$H = \langle a, b | a^2, b^2, (ab)^2 \rangle. \quad (\text{S4})$$

This is a Coxeter group isomorphic to the dihedral group $D_2 \cong \mathbb{Z}_2 \times \mathbb{Z}_2$ (Klein's Vierergruppe) of order $|H| = 4$.

So far, we have found that the set of all edges of the $\{2m, 3\}$ lattice is in one-to-one correspondence with the elements of the coset space $H \backslash G$. To construct a 3-edge coloring, we wish to partition $H \backslash G$ into three colors, i.e., distinct equivalence classes of x -vertices such that any three incident edges of the $\{2m, 3\}$ lattice have different colors. For this purpose, we first construct a subgroup $K = \langle A, B, C \rangle < G$ as the group generated by the group elements $A, B, C \in G$ defined as

$$A \equiv a, \quad B \equiv yay^{-1} = bcacb, \quad C \equiv y^{-1}ay = cbabc. \quad (\text{S5})$$

Geometrically, A, B, C are reflections with respect to the sides of a large equilateral reference triangle with interior angles $\frac{\pi}{m}$, which contains six small triangles of the $(2, 3, 2m)$ tessellation (dark shaded region in Fig. S1). We show in Section IC

¹ Hyperbolic triangle group symmetries were also used to construct three-colorings for hyperbolic tilings in Ref. 75.

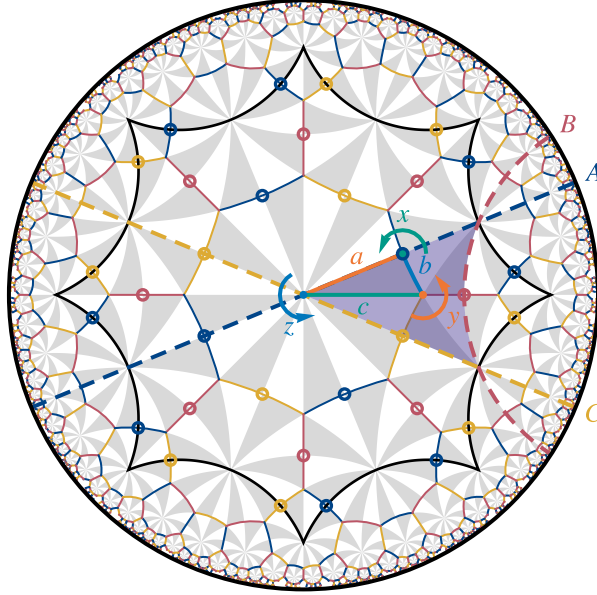


FIG. S1. Symmetric 3-edge coloring on the hyperbolic $\{2m, 3\}$ lattice (depicted here for $m = 4$). The space group $\Delta(2, 3, 2m)$ of this lattice is generated by the reflections a, b, c in the sides of a right triangle, which generate rotations $x = ab, y = bc, z = ca$ around the corners of this triangle as well as all other space-group operations. The edges of the $\{2m, 3\}$ lattice (open circles) are in one-to-one correspondence with the edges of the dual $\{3, 2m\}$ lattice, composed of equilateral triangles. Assigning a distinct color to the three sides of a reference equilateral triangle (shaded region), and applying all possible compositions of the reflections A, B, C (dashed lines) in the sides of this triangle (i.e., all operations in the subgroup $\Delta(m, m, m) \triangleleft \Delta(2, 3, 2m)$ generated by A, B, C), we generate a 3-edge coloring of the entire $\{2m, 3\}$ lattice which is invariant under those bond-cutting reflections. A Bravais unit cell (black octagon) preserves all the symmetries of the coloring provided that the corresponding translation group Γ is a normal subgroup in both $\Delta(2, 3, 2m)$ and $\Delta(m, m, m)$.

that A, B, C obey the defining relations of the hyperbolic triangle group $\Delta(m, m, m)$, which tiles the Poincaré disk with these equilateral triangles. Thus, we conclude that K is in fact isomorphic to $\Delta(m, m, m)$:

$$K \cong \Delta(m, m, m) = \langle A, B, C | A^2, B^2, C^2, (AB)^m, (BC)^m, (CA)^m \rangle. \quad (\text{S6})$$

The equilateral triangles correspond in fact to faces of the dual $\{3, 2m\}$ lattice, and the elements of K are reflections with respect to the edges of this dual lattice. Each of those edges intersects a single x -vertex $v \in v_x \cdot G$. Under this correspondence, the three sides of any equilateral triangle of the dual lattice encode a set of three edges of the $\{2m, 3\}$ lattice (or x -vertices) that meet at a single point. Thus, the problem of finding a 3-edge coloring of the $\{2m, 3\}$ lattice maps onto the problem of coloring the edges of the dual $\{3, 2m\}$ lattice such that the three sides of each equilateral triangle have different colors. A natural solution offers itself: color first the edges of a reference equilateral triangle, and then color the edges of all remaining equilateral triangles by applying all elements of K . Thus, algebraically, two x -vertices $v, v' \in v_x \cdot G$ belong to the same edge color (denoted $v \sim v'$) if and only if they are related by the right action of K , i.e., $v' = v \cdot k$ with $k \in K$. Writing $v' = v_x \cdot (h'g')$ and $v = v_x \cdot (hg)$ with $h, h' \in H$ and $g, g' \in G$, we see that $v \sim v'$ implies $v_x \cdot (h'g') = v_x \cdot (h'gk)$ and thus $h'g' = \tilde{h}hgk$ where $\tilde{h} \in H$. Redefining $h'^{-1}\tilde{h}h \mapsto h \in H$, this defines an equivalence relation on G , namely,

$$g \sim g' \text{ iff there exists } h \in H \text{ and } k \in K \text{ such that } h'gk = g'. \quad (\text{S7})$$

If H, K are subgroups of a group G , the equivalence class HgK of g under equivalence relation (S7) is called the (H, K) -double coset of $g \in G$, and the set of all (H, K) -double cosets is denoted $H \backslash G / K$ (“ $G \bmod K \bmod H$ ”) [92]:

$$H \backslash G / K = \{HK, Hg_2K, \dots, Hg_NK\}, \quad (\text{S8})$$

where $g_1 \equiv 1, g_2, \dots, g_N \in G$ are double coset representatives, assuming here a finite number $N \equiv |H \backslash G / K|$ of double cosets. As with ordinary cosets, double cosets form a disjoint decomposition of G . Thus, we have found that the set of distinct edge colors is in one-to-one correspondence with the elements of the double coset space $H \backslash G / K$. According to our earlier geometric argument, we expect there should be $N = 3$ colors, since x -vertices of different colors correspond to inequivalent sides of the (m, m, m) equilateral triangles, i.e., sides that are not related by the action of $K \cong \Delta(m, m, m)$. We also see that each site of the

$\{2m, 3\}$ lattice lies at the center of a unique equilateral (m, m, m) triangle, thus the three edges incident on this site are necessarily assigned different colors by our construction, satisfying the conditions for 3-edge coloring.

For consistency, it thus remains to be shown that $|H \backslash G / K| = 3$. To show this, we use the formula

$$|G : K| = \sum_{HgK \in H \backslash G / K} |H : H \cap gKg^{-1}|, \quad (\text{S9})$$

proven in Section **IC**, where $|G : K|$ denotes the index of K in G and the sum is over all double cosets in $H \backslash G / K$. In Section **IC**, we further prove two useful mathematical facts. First, $K \triangleleft G$; therefore, $gKg^{-1} = K$ and all summands in Eq. (S9) are equal, implying $|G : K| = |H \backslash G / K| |H : H \cap K|$. Second, $|G : K| = 6$, which corresponds to each triangle of the dual lattice consisting of six white or gray Schwarz triangles of the original lattice (Fig. **S1**). Combining these two facts, we have

$$|H \backslash G / K| = \frac{6}{|H : H \cap K|}. \quad (\text{S10})$$

We now consider the intersection $H \cap K$, which is the subset of elements of the stabilizer (S4) that are also in the triangle group $\Delta(m, m, m)$. Clearly, $a = A \in K$ [see Eq. (S6)] and thus the intersection $H \cap K$ contains at least the \mathbb{Z}_2 subgroup $\{1, a\} < H$. Regarding the other elements $\{b, ab\} \subset H$, they clearly cannot be in K . First, the element b is a reflection that passes through the equilateral reference triangle and swaps inequivalent (B and C) sides of this triangle (see Fig. **S1**), an operation that is not in $\Delta(m, m, m)$. It follows that also $ab \notin K$, as the converse would contradict $b = a^{-1}(ab) \notin K$. Thus, we find that $H \cap K = \{1, a\} \cong \mathbb{Z}_2$. Using Lagrange's theorem [92], we have $|H : H \cap K| = |H|/|H \cap K| = 2$, thus Eq. (S10) implies:

$$|H \backslash G / K| = 3, \quad (\text{S11})$$

predicting an edge coloring of the infinite $\{2m, 3\}$ lattice with three colors, as expected. Thus, for any edge associated to an x -vertex $v_x \cdot g$ with $g \in G$, we can determine its color algebraically by checking to which double coset in $H \backslash G / K$ the element g belongs, which is easily done in GAP [93].

B. Symmetric Bravais unit cells

For reciprocal-space calculations using the supercell method [13] or real-space calculations using finite clusters with periodic boundary conditions (PBC) [12], we must construct a Bravais unit cell and the corresponding translation group Γ , which is a torsion-free subgroup of the space group $\Delta(2, 3, 2m)$. In this section, Γ denotes either the primitive translation group [20] or a supercell translation group [13]. In particular, for verifications of the ground-state flux sector using the supercell method (Section **VI**), we would like to ensure that the chosen Bravais unit cell preserves the reflection symmetries mandated by Lieb's lemma. In this section, we show this is ensured if the corresponding translation group Γ is a normal subgroup of both $G = \Delta(2, 3, 2m)$ and $K = \Delta(m, m, m)$.

We first observe that on the Bravais unit cell associated to Γ , the infinite set $v_x \cdot G$ of x -vertices is replaced by the finite set of x -vertices contained inside the unit cell. Mathematically, the reference vertex v_x should be replaced by the orbit $\tilde{v}_x \equiv v_x \cdot \Gamma$, which is the set of all Γ -translates of v_x . For any $g \in G$ and $\gamma \in \Gamma$, the elements g and γg have the same right action on \tilde{v}_x . Thus, the group that acts most naturally on \tilde{v}_x is not G itself but rather the factor group G/Γ , i.e., the set of cosets Γg , which is a finite group of order $|G : \Gamma|$. (If Γ is chosen as the torsion-free normal subgroup of smallest possible index in G , then it is the primitive translation group of the $\{2m, 3\}$ lattice [20], and G/Γ is the point group of that lattice.) For G/Γ to be a group, we require Γ to be normal in G . Note that since $\Gamma \triangleleft G$, right and left cosets are equivalent and $\Gamma \backslash G = G/\Gamma$. Thus, the set of x -vertices contained inside the unit cell is the orbit $\tilde{v}_x \cdot (G/\Gamma)$.

Next, we wish to describe the orbit $\tilde{v}_x \cdot (G/\Gamma)$ in purely algebraic terms using the orbit-stabilizer theorem. To do so, we must find the stabilizer of \tilde{v}_x in G/Γ . We first define the product [92] of $\Gamma \triangleleft G$ and $H < G$ [Eq. (S3)] as

$$\Gamma H = \{\gamma h : \gamma \in \Gamma, h \in H\} = \{\Gamma h : h \in H\}. \quad (\text{S12})$$

Assuming $\gamma_1, \gamma_2 \in \Gamma$ and $h_1, h_2 \in H$, since Γ is normal in G , we have $(\gamma_1 h_1)(\gamma_2 h_2) = \gamma_1 h_1 \gamma_2 h_1^{-1} h_1 h_2 = \gamma_1 \gamma_2' h_1 h_2$ with $\gamma_2' \in \Gamma$, thus $\Gamma H < G$. This infinite subgroup of G leaves \tilde{v}_x invariant:

$$\begin{aligned} \tilde{v}_x \cdot (\gamma h) &= v_x \cdot (\Gamma \gamma h) \\ &= v_x \cdot (h \Gamma) \\ &= \tilde{v}_x, \end{aligned} \quad (\text{S13})$$

where we have used the normality of Γ and the fact that H stabilizes v_x . However, we want the stabilizer of \tilde{v}_x in the finite group G/Γ , which is the factor group $\Gamma H/\Gamma$, i.e., the set of (right) cosets of Γ in ΓH :

$$\begin{aligned}\Gamma H/\Gamma &= \{\Gamma, \Gamma\gamma_2 h_2, \dots, \Gamma\gamma_M h_M\} \\ &= \{\Gamma, \Gamma h_2, \dots, \Gamma h_M\},\end{aligned}\tag{S14}$$

assuming M cosets. This can be viewed as another generalization of coset space (i.e., one cannot directly write H/Γ since Γ is not a subgroup of H). That $\Gamma H/\Gamma$ is a group in this case follows from the fact that $\Gamma \triangleleft \Gamma H$. Indeed, first, $\Gamma \subset \Gamma H$ since $\Gamma = \Gamma \cdot 1$ with $1 \in H$. Second, $\Gamma < \Gamma H$ since Γ is a group. Third, Γ is normal in ΓH since it is normal in $G > \Gamma H$. Using the second isomorphism theorem [92], we have

$$\Gamma H/\Gamma \cong H/(\Gamma \cap H) \cong H \cong \mathbb{Z}_2 \times \mathbb{Z}_2,\tag{S15}$$

using the fact that $\Gamma \cap H = \{1\}$ since Γ is torsion-free and H contains only elements of finite order [Eq. (S4)]. Finally, $\Gamma H/\Gamma$ is a subgroup of G/Γ : it can be viewed as a set of (right) cosets of Γ in G , and it is a group. Thus, the stabilizer of \tilde{v}_x in G/Γ is $\Gamma H/\Gamma$, which is a finite group isomorphic to H .

Having identified $\tilde{G} \equiv G/\Gamma$ and $\tilde{H} \equiv \Gamma H/\Gamma$ as the unit cell equivalents of the groups G and H for the infinite lattice, we further define $\tilde{K} \equiv K/\Gamma$ as the third object required to construct a symmetric 3-edge coloring on the unit cell. For \tilde{K} to be a group, Γ must be a normal subgroup of $K = \Delta(m, m, m)$. Assuming this condition, by the third isomorphism theorem [92], we have $\tilde{K} \triangleleft \tilde{G}$ and also $\tilde{G}/\tilde{K} \cong G/K$ which implies $|\tilde{G} : \tilde{K}| = |G : K| = 6$. Thus, applying Eq. (S9) to the groups \tilde{G} , \tilde{H} , and \tilde{K} , we have

$$|\tilde{H} \backslash \tilde{G} / \tilde{K}| = \frac{6}{|\tilde{H} : \tilde{H} \cap \tilde{K}|}.\tag{S16}$$

Next, we compute $\tilde{H} \cap \tilde{K}$. Using the correspondence theorem (Section IC), since $\Gamma H, K < G$ and $\Gamma \triangleleft \Gamma H, K$, we have

$$\tilde{H} \cap \tilde{K} = (\Gamma H/\Gamma) \cap (K/\Gamma) = (\Gamma H \cap K)/\Gamma.\tag{S17}$$

Finally, we invoke Dedekind's modular law (Section IC), which implies that $\Gamma H \cap K = \Gamma(H \cap K)$. Using once more the second isomorphism theorem, we have

$$\tilde{H} \cap \tilde{K} = \Gamma(H \cap K)/\Gamma \cong (H \cap K)/(\Gamma \cap H \cap K) = (H \cap K)/\{1\} = H \cap K \cong \mathbb{Z}_2.\tag{S18}$$

Using again Lagrange's theorem, we have $|\tilde{H} : \tilde{H} \cap \tilde{K}| = |\tilde{H}|/|\tilde{H} \cap \tilde{K}| = |H|/|H \cap K| = 2$, thus

$$|\tilde{H} \backslash \tilde{G} / \tilde{K}| = 3,\tag{S19}$$

giving us again a (symmetric) 3-edge coloring, but this time on a finite unit cell.

Under the condition $\Gamma \triangleleft G, K$, the unit cell is manifestly compatible with the reflection symmetries relevant for Lieb's lemma, encoded in K . Indeed, on such a symmetric unit cell, the space group G descends to the quotient $\tilde{G} = G/\Gamma$, and the reflection symmetries $K \triangleleft G$ descend to the quotient $\tilde{K} = K/\Gamma \triangleleft \tilde{G}$. An example of symmetric unit cell is provided by the $\{8, 8\}$ unit cell on the $\{8, 3\}$ lattice (black octagon in Fig. S1). In general, given any finite-index translation group $\Gamma \triangleleft G$ not necessarily normal in K , one can always construct a symmetry-compatible translation group via $\Gamma' \equiv \Gamma \cap K$. The resulting Γ' also has finite index in G (and K), implying that the corresponding unit cell contains finitely many sites.

C. Useful mathematical results

Throughout the paper, when referring to groups, we use \subset to denote inclusion as a subset, $<$ to denote inclusion as a subgroup, and \triangleleft to denote inclusion as a normal subgroup. We work with finitely presented groups of the form

$$G = \langle S | R \rangle,\tag{S20}$$

where $S = \{s_1, s_2, \dots, s_k\}$ is a finite set of generators and $R = \{r_1, r_2, \dots, r_n\}$ is a finite set of relators, i.e., words in the generators that are set to the identity ($r_1 = r_2 = \dots = r_n = 1$).

1. $K \cong \Delta(m, m, m)$

Here, we prove algebraically that the elements $A, B, C \in G$ defined in Eq. (S5) obey the defining relations of $\Delta(m, m, m)$. Together with the geometric action of those elements on the Poincaré disk (Fig. S1), this establishes that $K = \langle A, B, C \rangle \cong \Delta(m, m, m)$. Here, a, b, c denote the generators of $\Delta(2, 3, 2m)$. First, we have

$$A^2 = a^2 = 1, \quad (\text{S21})$$

$$B^2 = yay^{-1}yay^{-1} = ya^2y^{-1} = yy^{-1} = 1, \quad (\text{S22})$$

$$C^2 = y^{-1}ayy^{-1}ay = y^{-1}a^2y = y^{-1}y = 1. \quad (\text{S23})$$

Next, using the relations $xyz = ab \cdot bc \cdot ca = 1$ and $x^2 = 1, y^3 = 1, z^{2m} = 1$, as well as Eqs. (S21-S23), we have:

$$\begin{aligned} (CA)^m &= (AC)^{-m} \\ &= (acbabc)^{-m} \\ &= (ab \cdot bc \cdot bc \cdot ca \cdot bc)^{-m} \\ &= (xy \cdot yz \cdot y)^{-m} \\ &= (z^{-1}xy)^{-m} \\ &= (z^{-2})^{-m} \\ &= 1. \end{aligned} \quad (\text{S24})$$

The remaining two relations $(BC)^m = 1$ and $(AB)^m = 1$ follow from the first one by conjugation by y (or y^{-1}), i.e., rotations about the center of the equilateral (m, m, m) triangle. Indeed, we have:

$$\begin{aligned} (BC)^m &= (CB)^{-m} \\ &= (cba \cdot bcba \cdot acb)^{-m} \\ &\stackrel{(bc)^3=1}{=} (cba \cdot cb \cdot acb)^{-m} \\ &= [cb(acba \cdot bcba)^m bc]^{-1} \\ &\stackrel{(cb)^3=1}{=} [cb(acbabc)^m bc]^{-1} \\ &\stackrel{(\text{S24})}{=} (y^{-1}y)^{-1} \\ &= 1. \end{aligned} \quad (\text{S25})$$

Similarly,

$$\begin{aligned} (AB)^m &= (BA)^{-m} \\ &= (bcacba)^{-m} \\ &= [bc(acbabc)^m cb]^{-1} \\ &\stackrel{(\text{S24})}{=} (yy^{-1})^{-1} \\ &= 1. \end{aligned} \quad (\text{S26})$$

2. $\Delta(m, m, m) \triangleleft \Delta(2, 3, 2m)$

It is known in the mathematical literature [94, 95] that $\Delta^+(m, m, m)$ is a normal subgroup of $\Delta^+(2, 3, 2m)$ of index 6, where $\Delta^+(r, q, p)$ denotes the von Dyck group or proper triangle group:

$$\Delta^+(r, q, p) = \langle x, y, z | xyz, x^r, y^q, z^p \rangle, \quad (\text{S27})$$

which is an index-2 subgroup of $\Delta(r, q, p)$ containing only orientation-preserving isometries of the Poincaré disk (rotations). Since reflections are important for Lieb's lemma, it is not sufficient for our purposes to work with the proper triangle groups. Here, we show that the normal subgroup inclusion above extends to the (improper) triangle group $\Delta(r, q, p)$.

To do this, we use the fact that a faithful representation $\rho : G \rightarrow \text{GL}(V)$ of a group G on a vector space V gives a group isomorphism between G and its image $\rho(G) \subset \text{GL}(V)$. In the Supplemental Material of Ref. 26, a faithful representation of

a	b	c	a	c	b	c	b	c
1	1	1	2	4	4	2	1	1

TABLE S1. Subgroup tables for Todd-Coxeter coset enumeration of $\Delta(m, m, m) \triangleleft \Delta(2, 3, 2m)$.

$\Delta(2, q, p)$ on $V = \mathbb{R}^3$ is given as

$$\rho(a) = \begin{pmatrix} -1 & 2 \cos \alpha & 2 \cos \gamma \\ 0 & 1 & 0 \\ 0 & 0 & 1 \end{pmatrix}, \quad \rho(b) = \begin{pmatrix} 1 & 0 & 0 \\ 0 & 1 & 0 \\ 2 \cos \gamma & 2 \cos \beta & -1 \end{pmatrix}, \quad \rho(c) = \begin{pmatrix} 1 & 0 & 0 \\ 2 \cos \alpha & -1 & 2 \cos \beta \\ 0 & 0 & 1 \end{pmatrix}, \quad (\text{S28})$$

where $\alpha = \frac{\pi}{p}$, $\beta = \frac{\pi}{q}$, and $\gamma = \frac{\pi}{2}$. Using this representation and setting $q = 3$ and $p = 2m$, we show using MATHEMATICA that the following relations hold:

$$\begin{aligned} aAa^{-1} &= A, & bAb^{-1} &= A, & cAc^{-1} &= C, \\ aBa^{-1} &= ABA, & bBb^{-1} &= C, & cBc^{-1} &= B, \\ aCa^{-1} &= ACA, & bCb^{-1} &= B, & cCc^{-1} &= A. \end{aligned} \quad (\text{S29})$$

Since any element $g \in G \equiv \Delta(2, 3, 2m)$ can be expressed as a word in $\{a, b, c\}$, and any element $k \in K \equiv \Delta(m, m, m)$ can be expressed as a word in $\{A, B, C\}$, this implies that $gkg^{-1} \in K$ for all $g \in G$ and $k \in K$. Thus, $K \triangleleft G$.

$$3. \quad |\Delta(2, 3, 2m) : \Delta(m, m, m)| = 6$$

Having shown that $K \equiv \Delta(m, m, m)$ is normal in $G \equiv \Delta(2, 3, 2m)$, we now show that $|G : K| = 6$ using the Todd-Coxeter coset enumeration procedure [96, 97]. The Todd-Coxeter procedure determines the index of a subgroup K in a finitely presented group G by systematically enumerating the right cosets Kg (here, since $K \triangleleft G$, right cosets are equivalent to left cosets). If $|G : K| < \infty$, the procedure is guaranteed to terminate in a finite number of steps, and returns the index $|G : K|$ as well as the full coset table (i.e., the permutation representation of the right action of G on the coset space $K \backslash G$).

The Todd-Coxeter algorithm constructs the cosets Kg one by one, utilizing two basic facts. First, for every coset Kg and relator $r_i = s_{\alpha_1} \cdots s_{\alpha_t}$ of G , where s_{α_i} is a generator of G (or its inverse), we have a sequence of $t+1$ cosets that starts and ends with Kg :

$$Kg, Kgs_{\alpha_1}, Kgs_{\alpha_1}s_{\alpha_2}, \dots, Kgs_{\alpha_1} \cdots s_{\alpha_t} = Kgr_i = Kg. \quad (\text{S30})$$

Second, consider a finitely generated subgroup $K = \langle w_1, w_2, \dots, w_l \rangle < G$. For every generating element $w_i = s_{\beta_1} \cdots s_{\beta_k}$, we have a sequence of $k+1$ cosets that starts and ends with the trivial coset K :

$$K, Ks_{\beta_1}, Ks_{\beta_1}s_{\beta_2}, \dots, Ks_{\beta_1} \cdots s_{\beta_k} = Kw_i = K, \quad (\text{S31})$$

utilizing the fact that $w_i \in K$.

For each generating element w_i in K , the sequence (S31) is expressed in a *subgroup table*. Here, K is generated by $A = a$, $B = bcacb$, and $C = cbabc$ [Eq. (S5)], thus we have three subgroup tables (Table S1). Denoting the trivial coset K by the number 1, each subgroup table is initialized with 1 at both the far left and the far right, with the other entries (corresponding to cosets as yet unknown) initially left blank.

Similarly, for each relator r_i of G , the sequence (S30) is expressed in a *relation table*. Each line of the table corresponds to a different coset Kg , with the first line corresponding to the trivial coset ("1"). Each relation table is again initialized with only the entry 1 at both the far left and far right of the first line. Here, G has six relators: a^2 , b^2 , c^2 , $(ab)^2$, $(bc)^3$, and $(ca)^{2m}$, thus there are six relation tables (Table S2). Entries in both the subgroup and relation tables symbolize the right action of a generator on a coset. For example, the entries:

$$\begin{array}{c|c} & c \\ \cdots & \cdots \\ 2 & 4 \\ \cdots & \cdots \end{array} \quad (\text{S32})$$

signify that right multiplication of coset 2 by generator c produces coset 4, i.e., $2c = 4$.

Finally, a *coset table* is also initialized (Table S3) and gradually filled out throughout the procedure. The i th row of the coset table corresponds to the coset Kg_i , and the j th column to the generator s_j of G , such that the corresponding entry of the table is the coset $Kg_i s_j$.

a	a
1	1
2	2
3	3
4	4
5	5
6	6

b	b
1	2
2	1
3	5
4	6
5	3
6	4

c	c
1	3
2	4
3	1
4	2
5	6
6	5

a	b	a	b
1	1	2	2
2	2	1	1
3	3	5	5
4	4	6	6
5	5	3	3
6	6	4	4

b	c	b	c	b	c
1	2	4	6	5	3
2	1	3	5	6	4
3	5	6	4	2	1
4	6	5	3	1	2
5	3	1	2	4	6
6	4	2	1	3	5

c	a	c	a	\cdots	c	a	c	a
1	3	3	1	1	\cdots	3	3	1
2	4	4	2	2	\cdots	4	4	2
3	1	1	3	3	\cdots	1	1	3
4	2	2	4	4	\cdots	2	2	4
5	6	6	5	5	\cdots	6	6	5
6	5	5	6	6	\cdots	5	5	6

TABLE S2. Relation tables for Todd-Coxeter coset enumeration of $\Delta(m, m, m) \triangleleft \Delta(2, 3, 2m)$. As emphasized by the blue and orange colors, each line of the last relation table features a repeating pattern of the form $\text{AABBAA}BB \cdots$, showing that the relation tables close after six cosets for any even $p = 2m$.

	a	a^{-1}	b	b^{-1}	c	c^{-1}
1	1	1	2	2	3	3
2	2	2	1	1	4	4
3	3	3	5	5	1	1
4	4	4	6	6	2	2
5	5	5	3	3	6	6
6	6	6	4	4	5	5

TABLE S3. Coset table for $\Delta(m, m, m) \triangleleft \Delta(2, 3, 2m)$ obtained from Todd-Coxeter coset enumeration.

The Todd-Coxeter procedure works by alternatively *defining* new cosets and reporting those definitions in the tables, and *deducing* facts about cosets from the subgroup and relation tables (which are also reported elsewhere in the tables). Coset l must always be defined from an earlier coset, i.e., $l = ks$ with $k < l$, for some generator s of G . For example here, after defining the trivial coset as 1, we deduce from the first subgroup table in Table S1 that $1a = 1$, and thus also that $1a^{-1} = 1$, which are reported in the coset table as well as in the subgroup and relation tables. Next, we define the second coset as $2 = 1b$. Reporting this in the second subgroup table, we deduce that $2b = 1$, which is also reported wherever appropriate. Through the successive definitions

$$1 \equiv K, \quad 2 \equiv 1b, \quad 3 \equiv 1c, \quad 4 \equiv 2c, \quad 5 \equiv 3b, \quad 6 \equiv 4b, \quad (\text{S33})$$

and attendant deductions, we eventually find that all tables simultaneously close after a finite number of steps. As guaranteed by the Todd-Coxeter procedure [96, 97], this implies that we have found all cosets, and thus $|G : K| = 6$.

4. Double coset formula

Here, we prove the formula (S9):

$$|G : K| = \sum_{HgK \in H \backslash G/K} |H : H \cap gKg^{-1}|. \quad (\text{S34})$$

Consider the space G/K of left K -cosets of G . For a given left K -coset $[g] \equiv gK$, the double coset $HgK = H[g]$ can be viewed as the orbit of the K -coset $[g]$ under a left action of H by multiplication $h \cdot [g] = (hg)K = [hg]$, $h \in H$. By the orbit-stabilizer theorem, the number of left K -cosets in this orbit is $|H : \text{Stab}_H([g])|$, where we denote by $\text{Stab}_H([g])$ the stabilizer of $[g]$ in H ,

$$\text{Stab}_H([g]) = H \cap gKg^{-1}. \quad (\text{S35})$$

Indeed, we have $gKg^{-1} \cdot [g] = gKg^{-1}gK = gK$, but we want the stabilizer in H so the intersection with H must be taken. Since the double coset decomposition is a disjoint decomposition of G , each K -coset belongs to a distinct double coset HgK . Thus, the total number $|G : K|$ of K -cosets in G is given by summing $|H : \text{Stab}_H([g])|$ over all distinct double cosets HgK , where g

denotes a choice of double coset representative:

$$|G : K| = \sum_{HgK \in H \backslash G / K} |H : \text{Stab}_H([g])| = \sum_{HgK \in H \backslash G / K} |H : H \cap gKg^{-1}|, \quad (\text{S36})$$

which gives Eq. (S9).

5. Correspondence theorem

The correspondence theorem is a general result in a group theory that states that, given a normal subgroup N of a group G , the subgroups of G containing N are in one-to-one correspondence with the subgroups of G/N [98]. Here, we use the simpler, following corollary (Proposition 7.16 in Ref. 98). Let $A, B < G$ and $N \triangleleft A, B$. Then

$$\begin{aligned} (A \cap B)/N &= \{Ng : g \in A \cap B\} \\ &= \{Ng : g \in A\} \cap \{Ng : g \in B\} \\ &= (A/N) \cap (B/N). \end{aligned} \quad (\text{S37})$$

6. Dedekind's modular law

Let H, Γ, K be subgroups of a group G and assume that $\Gamma \subseteq K$. Dedekind's modular law [92] stipulates that $\Gamma H \cap K = \Gamma(H \cap K)$, which is proven as follows. First, $\Gamma(H \cap K) \subseteq \Gamma H$ and $\Gamma(H \cap K) \subseteq \Gamma K = K$: hence $\Gamma(H \cap K) \subseteq \Gamma H \cap K$. Conversely, let $x \in \Gamma H \cap K$ and write $x = \gamma h$ with $\gamma \in \Gamma$ and $h \in H$: then $h = \gamma^{-1}x \in \Gamma K = K$, so that $h \in H \cap K$. Hence $x \in \Gamma(H \cap K)$.

II. HYPERBOLIC KITAEV MODEL

In this section, we review relevant aspects of Kitaev's spin liquid model, paying attention to its definition on any trivalent graph with an arbitrary 3-edge coloring. In Section II A, we discuss the general form of the time-reversal-symmetry breaking term and in Section II B, we derive the Majorana representation of the full Hamiltonian.

A. Time-reversal-breaking term

Before deriving the Majorana representation for the Hamiltonian given in Eq. (1) of the main text, we justify the appearance of the totally antisymmetric tensor $\varepsilon_{\alpha\beta\gamma}$ (which satisfies $\varepsilon_{xyz} = +1$) in the three-spin term:

$$\hat{\mathcal{H}}_K = -K \sum_{[lmn]_{\alpha\beta\gamma}^+} \varepsilon_{\alpha\beta\gamma} \hat{\sigma}_l^\alpha \hat{\sigma}_m^\beta \hat{\sigma}_n^\gamma. \quad (\text{S38})$$

The two sublattices (filled/empty disks in Fig. 1a of the main text and in Fig. S2) of the infinite $\{p, 3\}$ hyperbolic lattice are related by reflection symmetry. This manifests as filled (empty) sites always lying in white (gray) Schwarz triangles of $\Delta(p/2, p/2, p/2)$. Our symmetric coloring is, by construction, compatible with $\Delta(p/2, p/2, p/2)$ which implies that the colors of the bonds around sites from different sublattices are related to each other by an odd number of reflections and thus oriented oppositely, see Fig. S1.

We now argue that Eq. (S38) is reflection-symmetric. Any reflection operator $\hat{\theta}$ acts on the spin operators as $\hat{\theta} \hat{\sigma}_j^\alpha \hat{\theta}^{-1} = -\hat{\sigma}_{j'}^\alpha$, where j' is the reflected partner of j and we use the fact that the coloring is invariant under reflections. Considering a single term in $\hat{\mathcal{H}}_K$, associated with the triplet $[lmn]_{\alpha\beta\gamma}^+$, we first note that the reflected triplet has opposite orientation: $[l'm'n']_{\alpha\beta\gamma}^-$ as can be seen in Fig. S2. Then,

$$\begin{aligned} \hat{\theta} \varepsilon_{\alpha\beta\gamma} \hat{\sigma}_l^\alpha \hat{\sigma}_m^\beta \hat{\sigma}_n^\gamma \hat{\theta}^{-1} &= -\varepsilon_{\alpha\beta\gamma} \hat{\sigma}_{l'}^\alpha \hat{\sigma}_{m'}^\beta \hat{\sigma}_{n'}^\gamma, \\ &= \varepsilon_{\gamma\beta\alpha} \hat{\sigma}_{n'}^\gamma \hat{\sigma}_{m'}^\beta \hat{\sigma}_{l'}^\alpha, \end{aligned} \quad (\text{S39})$$

where we used the antisymmetry of $\varepsilon_{\alpha\beta\gamma}$, the fact that the spin operators on different sites commute, and rearranged the operators such that they correspond to the triplet $[n'm'l']_{\gamma\beta\alpha}^+$ oriented as it appears in the sum in Eq. (S38). Thus, we arrive at

$$\hat{\theta} \hat{\mathcal{H}}_K \hat{\theta}^{-1} = \hat{\mathcal{H}}_K. \quad (\text{S40})$$

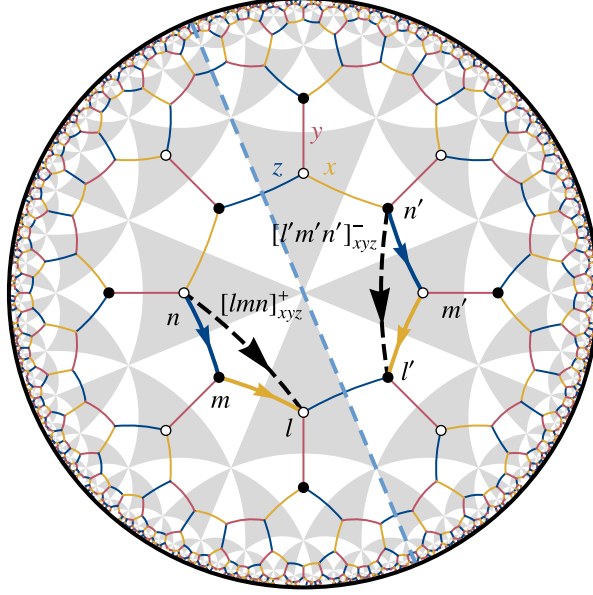


FIG. S2. Illustration of the triplets $[lmn]_{\alpha\beta\gamma}^+$ involved in the definition of the K -term on the $\{8, 3\}$ lattice with symmetric coloring. A three-spin interaction is defined by a triplet (n, m, l) of sites, where the superscript “+” in the label $[lmn]_{xyz}^+$ denotes counterclockwise (positive) orientation around the octagonal plaquette the path $n \rightarrow m \rightarrow l$ is part of. This is illustrated with the sites n, m, l to the left of the blue dashed mirror line. In the Majorana representation, this becomes a next-nearest-neighbor hopping (dashed black arrow) from n to l , inheriting the counterclockwise orientation with respect to going around the center of the plaquette. The corresponding bond operators \hat{u}_{mn} (z -bond from n to m) and \hat{u}_{lm} (x -bond from m to l) whose eigenvalues determine the hopping amplitude are indicated as bold solid arrows. Note that the reflected triplet is indeed oriented oppositely, i.e., clockwise, justifying the label $[l'm'n']_{xyz}^-$.

For the coloring used in Ref. 49, the factor $\varepsilon_{\alpha\beta\gamma}$ is unnecessary, because for any positively oriented triplet $[lmn]_{\alpha\beta\gamma}^+$, $\varepsilon_{\alpha\beta\gamma}$ always takes the same value. We also note that, although reminiscent of the scalar spin chiralities $\hat{\chi}_{lmn} \equiv \hat{\sigma}_l \cdot (\hat{\sigma}_m \times \hat{\sigma}_n)$ [99], the operators appearing in Eq. (S38) are not the same as $\hat{\chi}_{lmn}$ because there is no free sum over α, β, γ ; rather, the spin components are fixed by the colors α, β, γ of the bonds incident on l, m, n . Therefore, just like the two-spin term in the Hamiltonian, the three-spin term (S38) completely breaks the $SU(2)$ spin rotation symmetry.

B. Majorana representation

In this subsection, we derive the Majorana representation, i.e., Eq. (2) of the main text, for the Hamiltonian given in Eq. (1):

$$\hat{\mathcal{H}} = - \sum_{\langle j,k \rangle_\alpha} J_\alpha \hat{\sigma}_j^\alpha \hat{\sigma}_k^\alpha - K \sum_{[lmn]_{\alpha\beta\gamma}^+} \varepsilon_{\alpha\beta\gamma} \hat{\sigma}_l^\alpha \hat{\sigma}_m^\beta \hat{\sigma}_n^\gamma. \quad (\text{S41})$$

We follow Ref. 49 and introduce the Majorana fermions \hat{b}_j^α , $\alpha \in \{x, y, z\}$, and \hat{c}_j , at each site j , such that $\hat{\sigma}_j^\alpha = i\hat{b}_j^\alpha \hat{c}_j$. Further, for the nearest-neighbor bond $\langle j, k \rangle_\alpha$, we define the bond variable $\hat{u}_{jk} = i\hat{b}_j^\alpha \hat{b}_k^\alpha$. Recall that this extends the Hilbert space and comes with the gauge transformation operators $\hat{D}_j = \hat{b}_j^x \hat{b}_j^y \hat{b}_j^z \hat{c}_j$ that define the physical subspace as their common +1 eigenspace. The first term in the Hamiltonian then becomes

$$\begin{aligned} \hat{\mathcal{H}}_J &= - \sum_{\langle j,k \rangle_\alpha} J_\alpha \left(i\hat{b}_j^\alpha \hat{c}_j \right) \left(i\hat{b}_k^\alpha \hat{c}_k \right) \\ &= \sum_{\langle j,k \rangle_\alpha} J_\alpha \left(i\hat{b}_j^\alpha \hat{b}_k^\alpha \right) i\hat{c}_j \hat{c}_k \\ &= \sum_{\langle j,k \rangle_\alpha} J_\alpha \hat{u}_{jk} i\hat{c}_j \hat{c}_k, \end{aligned} \quad (\text{S42})$$

and the second

$$\begin{aligned}
\hat{\mathcal{H}}_K &= -K \sum_{[lmn]_{\alpha\beta\gamma}^+} \varepsilon_{\alpha\beta\gamma} \left(i\hat{b}_l^\alpha \hat{c}_l \right) \left(i\hat{b}_m^\beta \hat{c}_m \right) \left(i\hat{b}_n^\gamma \hat{c}_n \right) \\
&= K \sum_{[lmn]_{\alpha\beta\gamma}^+} \varepsilon_{\alpha\beta\gamma} \left(i\hat{b}_l^\alpha \right) \left(i\hat{b}_m^\beta \hat{c}_m \right) \hat{b}_n^\gamma i\hat{c}_l \hat{c}_n \\
&= K \sum_{[lmn]_{\alpha\beta\gamma}^+} \varepsilon_{\alpha\beta\gamma} \left(i\hat{b}_l^\alpha \hat{b}_m^\alpha \hat{b}_n^\alpha \right) \hat{b}_m^\beta \hat{c}_m \hat{b}_n^\gamma \left(i\hat{b}_m^\gamma \hat{b}_n^\gamma \right) i\hat{c}_l \hat{c}_n \\
&= K \sum_{[lmn]_{\alpha\beta\gamma}^+} \varepsilon_{\alpha\beta\gamma} \hat{b}_m^\alpha \hat{b}_m^\beta \hat{b}_m^\gamma \hat{c}_m \hat{u}_{lm} \hat{u}_{mn} i\hat{c}_l \hat{c}_n \\
&= K \sum_{[lmn]_{\alpha\beta\gamma}^+} \hat{b}_m^x \hat{b}_m^y \hat{b}_m^z \hat{c}_m \hat{u}_{lm} \hat{u}_{mn} i\hat{c}_l \hat{c}_n \\
&= K \sum_{[lmn]_{\alpha\beta\gamma}^+} \hat{D}_m \hat{u}_{lm} \hat{u}_{mn} i\hat{c}_l \hat{c}_n.
\end{aligned} \tag{S43}$$

Since $D_m = +1$ in the physical subspace, we can drop it, such that we arrive at

$$\hat{\mathcal{H}} = \sum_{\langle j,k \rangle_\alpha} J_\alpha \hat{u}_{jk} i\hat{c}_j \hat{c}_k + K \sum_{[lmn]_{\alpha\beta\gamma}^+} \hat{u}_{lm} \hat{u}_{mn} i\hat{c}_l \hat{c}_n. \tag{S44}$$

This can be written compactly as

$$\hat{\mathcal{H}} = \frac{i}{4} \sum_{j,k} \hat{A}_{jk} \hat{c}_j \hat{c}_k, \tag{S45}$$

with

$$\hat{A}_{jk} = \begin{cases} 2J_\alpha \hat{u}_{jk}, & \text{for } \langle j,k \rangle_\alpha, \\ \pm 2K \hat{u}_{jl} \hat{u}_{lk}, & \text{for } [jlk]_{\alpha\beta\gamma}^\pm, \end{cases} \tag{S46}$$

where the additional factor of 1/2 compensates the double counting of each bond and triplet. Note that $\hat{A}_{kj} = -\hat{A}_{jk}$, because $\hat{u}_{kj} = -\hat{u}_{jk}$ and $[klj]_{\gamma\beta\alpha}^\pm \hat{=} [jlk]_{\alpha\beta\gamma}^\mp$, see also Fig. S2.

As discussed in the main text, in a fixed flux sector, we can replace the bond operators \hat{u}_{jk} by their expectation values u_{jk} and thus \hat{A}_{jk} by the skew-symmetric real matrix A_{jk} , resulting in the Hamiltonian

$$\hat{\mathcal{H}} = \frac{i}{4} \sum_{j,k} A_{jk} \hat{c}_j \hat{c}_k, \tag{S47}$$

acting only on the fermionic degrees of freedom in the specified flux sector. Note that A in Eq. (S47) is gauge dependent. Projection to the physical (gauge-invariant) subspace is important for exact computations of quantities in the original spin model like the many-body ground-state energy and the \mathbb{Z}_2 vortex gap, especially in a finite system with periodic boundary conditions [100]. However, as in earlier work [49, 67], we focus here only on the fermionic excitation spectrum in the thermodynamic limit, which is correctly given by the (positive) eigenvalues of the Hermitian matrix $H = iA$ in a fixed flux sector. We further make the simplifying assumption that the $K = 0$ flux sector determined by Lieb's lemma persists for $K \neq 0$, which is correct for infinitesimal K but ignores the possibility of flux phase transitions at finite K . The assumption is consistent with our results in Section VI, where we find that among all the translation-invariant flux configurations with zero net flux per primitive cell, the homogeneous π -flux configuration has lowest energy even for relatively large K . We leave an analysis of the stability of the π -flux sector for future work.

We finally comment on time-reversal symmetry. The antiunitary time-reversal operator $\hat{\mathcal{T}}$ acts on the spin operators as $\hat{\mathcal{T}} \hat{\sigma}_j^\alpha \hat{\mathcal{T}}^{-1} = -\hat{\sigma}_j^\alpha$, thus the three-spin term in Eq. (S38) is odd under time reversal:

$$\hat{\mathcal{T}} \hat{\mathcal{H}}_K \hat{\mathcal{T}}^{-1} = -\hat{\mathcal{H}}_K. \tag{S48}$$

In the Majorana representation, Eq. (S47), it is useful to consider time reversal composed with a gauge transformation to compensate for the change in sign of $\hat{u}_{jk} = i\hat{b}_j^\alpha \hat{b}_k^\alpha$ due to the antiunitary nature of $\hat{\mathcal{T}}$ [49]. The corresponding symmetry $\hat{\mathcal{T}}'$, which leaves \hat{u}_{jk} invariant but flips the sign of \hat{c}_j on one of the sublattices, enforces couplings only between the two sublattices. Correspondingly, $K \neq 0$ turns on a coupling within each sublattice, analogous to the next-nearest neighbor hopping in the Haldane model [101], suggesting a non-vanishing Chern number (see Sec. IX).

III. HYPERBOLIC BAND THEORY FOR MAJORANA HAMILTONIANS

In this section, we extend the concept of hyperbolic band theory and hyperbolic Bloch Hamiltonians [11, 12] including the supercell method [13] to generic quadratic Majorana Hamiltonians of the form of Eq. (S47), i.e.,

$$\hat{\mathcal{H}} = \frac{i}{4} \sum_{j,k} A_{jk} \hat{c}_j \hat{c}_k, \quad (\text{S49})$$

where A is a skew-symmetric real matrix, $A^\top = -A$, and $\{\hat{c}_j, \hat{c}_k\} = 2\delta_{jk}$.

Following the ideas in Ref. 13, we assume $\hat{\mathcal{H}}$ in Eq. (S49) to be defined on a large (but finite) cluster of a hyperbolic lattice with periodic boundary conditions (PBC cluster). At the very end, we formally take the limit [25] of an infinite PBC cluster, recovering a description of the infinite lattice. The large PBC cluster is defined [12] by a normal subgroup Γ_{PBC} of the full translation group Γ and of the triangle group Δ . Further, we assume a division of the PBC cluster into N translated copies of a (super-)cell, characterized by $\Gamma_{\text{sc}} \triangleleft \Delta$, $\Gamma_{\text{sc}} \leq \Gamma$, such that $\Gamma_{\text{PBC}} \triangleleft \Gamma_{\text{sc}}$. These copies are labeled by the corresponding translations from the supercell at the origin to the copy, modulo translations in Γ_{PBC} . Thus, the different copies of supercells are labeled by cosets $\eta \in G = \Gamma_{\text{sc}}/\Gamma_{\text{PBC}}$. This, in turn, allows us to enumerate all sites in the PBC cluster as tuples (η, j) , where j now labels the corresponding Wyckoff position in the supercell rather than the site in the PBC cluster; there are $M = |\Delta : \Gamma_{\text{sc}}|$ such Wyckoff positions. Writing $\hat{c}_{(\eta,j')} = \hat{c}_{\eta,j}$, the Hamiltonian can be written as

$$\hat{\mathcal{H}} = \frac{i}{4} \sum_{\eta, \eta' \in G} \sum_{j,k=1}^M A_{(\eta',j),(\eta,k)} \hat{c}_{\eta',j} \hat{c}_{\eta,k}. \quad (\text{S50})$$

By translation invariance, the skew-symmetric matrix satisfies $A_{(\eta',j),(\eta,k)} = A_{jk}(\eta'\eta^{-1})$, i.e., it depends only on the relative translation $\gamma = \eta'\eta^{-1} \in G$ between the two copies of the supercell and not their absolute position. Recognizing that $\eta' = \gamma\eta$, we arrive at

$$\hat{\mathcal{H}} = \frac{i}{4} \sum_{\eta, \gamma \in G} \sum_{j,k} A_{jk}(\gamma) \hat{c}_{\gamma\eta,j} \hat{c}_{\eta,k} \quad (\text{S51})$$

where j, k implicitly run from 1 to M .

To rewrite Eq. (S51) in hyperbolic reciprocal space, we use the formalism recently developed in Ref. 35, which defines a Fourier transform on PBC clusters. Let $f(\gamma)$ be a function (potentially operator-valued) on G and denote the irreducible representations of G by $D^{(K)}$. Recall that because G is generally non-Abelian, $D^{(K)}$ can be matrix valued and we denote its dimension by d_K ; K takes the role of momentum in hyperbolic reciprocal space. Then, the Fourier transform is defined as

$$f(\gamma) = \frac{1}{\sqrt{N}} \sum_{K, \mu, \nu} \sqrt{d_K} f_{\mu\nu}^{(K)} D_{\nu\mu}^{(K)}(\gamma)^*, \quad (\text{S52a})$$

$$f_{\mu\nu}^{(K)} = \frac{1}{\sqrt{N}} \sum_{\gamma \in G} \sqrt{d_K} f(\gamma) D_{\nu\mu}^{(K)}(\gamma), \quad (\text{S52b})$$

where $N = |G| = |\Gamma_{\text{PBC}} : \Gamma_{\text{sc}}|$, K runs over all irreducible representations and μ, ν run from 1 to d_K . Here, the unitary matrix $D_{\nu\mu}^{(K)}(\gamma)$ plays a role akin to the usual phase factor $e^{i\mathbf{K}\cdot\mathbf{R}}$ on Euclidean lattices.

This allows us to define the following reciprocal-space representation $\hat{a}_{\mu\nu,j}^{(K)}$ for the Majorana operators $\hat{c}_{\eta,j}$,

$$\hat{c}_{\eta,j} = \sqrt{\frac{2}{N}} \sum_{K, \mu, \nu} \sqrt{d_K} \hat{a}_{\mu\nu,j}^{(K)} D_{\nu\mu}^{(K)}(\eta)^*, \quad (\text{S53a})$$

$$\hat{a}_{\mu\nu,j}^{(K)} = \frac{1}{\sqrt{2N}} \sum_{\eta \in G} \sqrt{d_K} \hat{c}_{\eta,j} D_{\nu\mu}^{(K)}(\eta), \quad (\text{S53b})$$

which satisfy canonical anticommutation relations:

$$\begin{aligned} \left\{ \hat{a}_{\mu\nu,j}^{(K)}, \hat{a}_{\mu'\nu',k}^{(K')} \right\}^\dagger &= \frac{d_K}{2N} \sum_{\eta, \eta' \in G} D_{\nu\mu}^{(K)}(\eta) D_{\nu'\mu'}^{(K')}(\eta)^* \{ \hat{c}_{\eta,j}, \hat{c}_{\eta',k} \} \\ &= \frac{d_K}{N} \delta_{jk} \sum_{\eta \in G} D_{\nu\mu}^{(K)}(\eta) D_{\nu'\mu'}^{(K')}(\eta)^* \\ &= \delta_{KK'} \delta_{\mu\mu'} \delta_{\nu\nu'} \delta_{jk}, \end{aligned} \quad (\text{S54})$$

where we used $\{\hat{c}_{\eta,j}, \hat{c}_{\eta',k}\} = 2\delta_{\eta\eta'}\delta_{jk}$ as well as Schur's orthogonality relation. However, the fact that $\hat{c}_{\eta,j}^\dagger = \hat{c}_{\eta,j}$ implies that $\hat{a}_{\mu\nu,j}^{(K)}$ and $\hat{a}_{\mu\nu,k}^{(K)\dagger}$ are *not* independent:

$$\begin{aligned}\hat{a}_{\mu\nu,k}^{(K)\dagger} &= \frac{1}{\sqrt{2N}} \sum_{\eta \in G} \sqrt{d_K} \hat{c}_{\eta,j} D_{\nu\mu}^{(K)}(\eta)^* \\ &= \frac{1}{\sqrt{2N}} \sum_{\eta \in G} \sqrt{d_K} \hat{c}_{\eta,j} D_{\nu\mu}^{(-K)}(\eta) \\ &= \hat{a}_{\mu\nu,k}^{(-K)},\end{aligned}\tag{S55}$$

where $D^{(-K)}$ is the representation conjugate to $D^{(K)}$. Thus, self-conjugate (real) representations $D^{(-K)} = D^{(K)}$, if any, generalize to hyperbolic lattices the notion of time-reversal invariant momenta.

Rewriting Eq. (S51), we thus find

$$\begin{aligned}\hat{\mathcal{H}} &= \frac{i}{2N} \sum_{\eta, \gamma \in G} \sum_{j,k} A_{jk}(\gamma) \sum_{K, \mu, \nu} \sqrt{d_K} \hat{a}_{\mu\nu,j}^{(K)\dagger} D_{\nu\mu}^{(K)}(\gamma\eta) \sum_{K', \mu', \nu'} \sqrt{d_{K'}} \hat{a}_{\mu'\nu',k}^{(K')} D_{\nu'\mu'}^{(K')}(\eta)^* \\ &= \frac{i}{2N} \sum_{\gamma \in G} \sum_{j,k} A_{jk}(\gamma) \sum_{\substack{K, \mu, \nu \\ K', \mu', \nu'}} \sqrt{d_K d_{K'}} \hat{a}_{\mu\nu,j}^{(K)\dagger} \hat{a}_{\mu'\nu',k}^{(K')} \sum_{\lambda} D_{\nu\lambda}^{(K)}(\gamma) \sum_{\eta \in G} D_{\lambda\mu}^{(K)}(\eta) D_{\nu'\mu'}^{(K')}(\eta)^*,\end{aligned}$$

where we used that $D^{(K)}(\gamma\eta) = D^{(K)}(\gamma)D^{(K)}(\eta)$. Using Schur's orthogonality relation, this becomes

$$\begin{aligned}&= \frac{i}{2N} \sum_{\gamma \in G} \sum_{j,k} A_{jk}(\gamma) \sum_{\substack{K, \mu, \nu \\ K', \mu', \nu'}} \sqrt{d_K d_{K'}} \hat{a}_{\mu\nu,j}^{(K)\dagger} \hat{a}_{\mu'\nu',k}^{(K')} D_{\nu\mu}^{(K)}(\gamma) \frac{N}{d_K} \delta_{KK'} \delta_{\mu\mu'} \delta_{\lambda\nu'}, \\ &= \frac{i}{2} \sum_{K, \lambda, \mu, \nu} \sum_{j,k} \sum_{\gamma \in G} A_{jk}(\gamma) D_{\nu\lambda}^{(K)}(\gamma) \hat{a}_{\mu\nu,j}^{(K)\dagger} \hat{a}_{\mu\lambda,k}^{(K)} \\ &= \frac{i}{2} \sum_K \sum_{\mu, \nu, \nu'} \sum_{j,k} A_{\nu,j;\nu',k}^{(K)} \hat{a}_{\mu\nu,j}^{(K)\dagger} \hat{a}_{\mu\nu',k}^{(K)},\end{aligned}\tag{S56}$$

where in the last step, we defined the reciprocal-space representation of the matrix A :

$$A_{\nu,j;\nu',k}^{(K)} = \sum_{\gamma \in G} A_{jk}(\gamma) D_{\nu\nu'}^{(K)}(\gamma).\tag{S57}$$

Since $A(\gamma)$ is skew-symmetric, we can consider the Hermitian matrix $iA(\gamma)$, such that

$$H(K) = iA^{(K)} = \sum_{\gamma \in G} iA(\gamma) \otimes D^{(K)}(\gamma),\tag{S58}$$

is a Bloch Hamiltonian as defined in Ref. 13. Let $U^{(K)}$ be the unitary matrix diagonalizing $H(K)$, such that

$$H_{\nu,j;\nu',k}(K) = \sum_{\lambda,l} (U^{(K)\dagger})_{\nu,j;\lambda,l} \varepsilon_{\lambda,l}(K) U_{\lambda,l;\nu',k}^{(K)}\tag{S59}$$

and define

$$\hat{d}_{\mu\lambda,l}^{(K)} = \sum_{\nu,j} U_{\lambda,l;\nu,j}^{(K)} \hat{a}_{\mu\nu,j}^{(K)},\tag{S60}$$

which are again canonically normalized, i.e., $\{\hat{d}_{\mu\lambda,l}^{(K)}, \hat{d}_{\mu'\lambda',m}^{(K)\dagger}\} = \delta_{KK'} \delta_{\mu\mu'} \delta_{\lambda\lambda'} \delta_{lm}$. This diagonalizes the Hamiltonian in Eq. (S56):

$$\begin{aligned}\hat{\mathcal{H}} &= \frac{1}{2} \sum_K \sum_{\mu, \nu, \nu', \lambda} \sum_{j,k,l} \hat{a}_{\mu\nu,j}^{(K)\dagger} (U^{(K)\dagger})_{\nu,j;\lambda,l} \varepsilon_{\lambda,l}(K) U_{\lambda,l;\nu',k}^{(K)} \hat{a}_{\mu\nu',k}^{(K)} \\ &= \frac{1}{2} \sum_{K, \lambda, \mu, l} \varepsilon_{\lambda,l}(K) \hat{d}_{\mu\lambda,l}^{(K)\dagger} \hat{d}_{\mu\lambda,l}^{(K)}.\end{aligned}\tag{S61}$$

Note that Eq. (S58) is Hermitian, $H(K)^\dagger = H(K)$ and thus satisfies

$$H(K)^\top = H(K)^* = - \sum_{\gamma \in G} iA(\gamma) \otimes D^{(K)}(\gamma)^* = -H(-K), \quad (\text{S62})$$

where we used that $D^{(K)}(\gamma)^* = D^{(-K)}(\gamma)$. Since $H(K)^\top$ and $H(K)$ have the same spectrum, it is always possible to choose appropriate bases (for the indices λ, l) in the K and $-K$ sectors, such that

$$\varepsilon_{\lambda,l}(-K) = -\varepsilon_{\lambda,l}(K). \quad (\text{S63})$$

The above allows us to rewrite the sum in Eq. (S61) by splitting it according to the sign of $\varepsilon_{\lambda,l}(K)$:

$$\hat{\mathcal{H}} = \frac{1}{2} \sum_{\substack{K,\lambda,\mu,l \\ \varepsilon_{\lambda,l}(K) > 0}} \varepsilon_{\lambda,l}(K) \hat{d}_{\mu\lambda,l}^{(K)\dagger} \hat{d}_{\mu\lambda,l}^{(K)} + \frac{1}{2} \sum_{\substack{K,\lambda,\mu,l \\ \varepsilon_{\lambda,l}(K) < 0}} \varepsilon_{\lambda,l}(K) \hat{d}_{\mu\lambda,l}^{(K)\dagger} \hat{d}_{\mu\lambda,l}^{(K)}. \quad (\text{S64})$$

In the second term, we rewrite the sum over K as a sum over $K' = -K$, such that

$$\begin{aligned} \frac{1}{2} \sum_{\substack{K,\lambda,\mu,l \\ \varepsilon_{\lambda,l}(K) < 0}} \varepsilon_{\lambda,l}(K) \hat{d}_{\mu\lambda,l}^{(K)\dagger} \hat{d}_{\mu\lambda,l}^{(K)} &= \frac{1}{2} \sum_{\substack{K',\lambda,\mu,l \\ \varepsilon_{\lambda,l}(K') > 0}} \varepsilon_{\lambda,l}(-K') \hat{d}_{\mu\lambda,l}^{(-K')\dagger} \hat{d}_{\mu\lambda,l}^{(-K')} \\ &= -\frac{1}{2} \sum_{\substack{K',\lambda,\mu,l \\ \varepsilon_{\lambda,l}(K') > 0}} \varepsilon_{\lambda,l}(K') \hat{d}_{\mu\lambda,l}^{(K')\dagger} \hat{d}_{\mu\lambda,l}^{(K')} \\ &= \frac{1}{2} \sum_{\substack{K',\lambda,\mu,l \\ \varepsilon_{\lambda,l}(K') > 0}} \varepsilon_{\lambda,l}(K') \left(\hat{d}_{\mu\lambda,l}^{(K')\dagger} \hat{d}_{\mu\lambda,l}^{(K')} - 1 \right). \end{aligned} \quad (\text{S65})$$

Substituting back into Eq. (S64), we find

$$\begin{aligned} \hat{\mathcal{H}} &= \frac{1}{2} \sum_{\substack{K,\lambda,\mu,l \\ \varepsilon_{\lambda,l}(K) > 0}} \varepsilon_{\lambda,l}(K) \hat{d}_{\mu\lambda,l}^{(K)\dagger} \hat{d}_{\mu\lambda,l}^{(K)} + \frac{1}{2} \sum_{\substack{K,\lambda,\mu,l \\ \varepsilon_{\lambda,l}(K) > 0}} \varepsilon_{\lambda,l}(K) \left(\hat{d}_{\mu\lambda,l}^{(K)\dagger} \hat{d}_{\mu\lambda,l}^{(K)} - 1 \right) \\ &= \sum_{\substack{K,\lambda,\mu,l \\ \varepsilon_{\lambda,l}(K) > 0}} \varepsilon_{\lambda,l}(K) \left(\hat{d}_{\mu\lambda,l}^{(K)\dagger} \hat{d}_{\mu\lambda,l}^{(K)} - \frac{1}{2} \right). \end{aligned} \quad (\text{S66})$$

Equation (S66) implies that the spectrum of Eq. (S49) can be found by diagonalizing the Bloch Hamiltonian Eq. (S58) for different K . However, since we are dealing with hyperbolic lattices, K labels not simply ordinary Bloch states, but also non-Abelian Bloch states transforming in higher-dimensional irreducible representations of the translation group. In order to deal with those, we apply the supercell method [13] as discussed in the next section.

IV. THE SUPERCELL METHOD

The supercell method gives access to non-Abelian Bloch states on hyperbolic lattices by considering Abelian Bloch states on a sequence of supercells increasing in size [13]. Here, we apply the method to the Bloch Hamiltonian given in Eq. (S58). In this section, we provide all the necessary details on the computations performed to obtain the data presented in the main text and in later sections. In Section IV A, we specify the particular supercell-sequence that we use and provide details on the random sampling in the Abelian Brillouin zones, followed by more details on the specification of the model in Section IV B. Details on how we extract the many-body ground-state energy, the density of states, and the spectral gap from the fermionic spectrum computed on the supercells, are provided in Section IV C, Section IV D, and Section IV E, respectively.

A. Supercell sequence and state sampling

We consider the hyperbolic Kitaev model on the $\{8, 3\}$ lattice which has symmetry group $\Delta(2, 3, 8)$, see Eq. (S1). The symmetric 3-edge coloring discussed in Section I, breaks that symmetry down to the normal subgroup $\Delta(4, 4, 4) \triangleleft \Delta(2, 3, 8)$, see

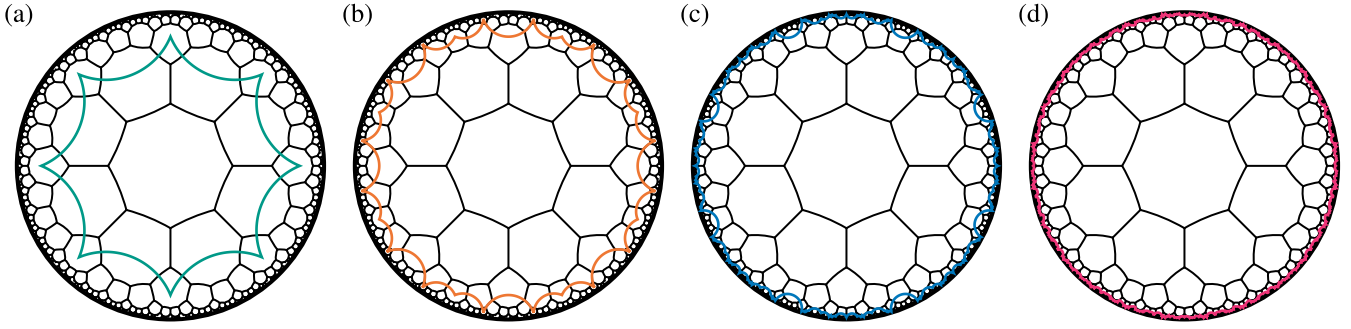


FIG. S3. Supercell sequence used in the computations and defined by the quotients in Eqs. (S67) and (S71): (a) primitive cell T2.1 with 16 sites and 6 plaquettes; (b) first supercell T5.1 with 64 sites and 24 plaquettes; (c) second supercell T17.2 with 256 sites and 96 plaquettes; (d) third supercell T33.1 with 512 sites and 192 plaquettes. The largest supercell (see text) used in the computations is not shown.

Figs. S1 and 1a. The primitive unit cell of the model is thus given by the torsion-free normal subgroup $\Gamma \triangleleft \Delta(4, 4, 4), \Delta(2, 3, 8)$ of lowest index. Such normal subgroups are tabulated, e.g., in Ref. 63, in terms of the quotients of the proper triangle group Δ^+ , i.e., Δ^+/Γ labeled in the form Tg.n. Here, g is the genus of the Riemann surface the group Δ acts on, i.e., on which the corresponding cell can be embedded with periodic boundary conditions, and n is a running index for given g. In our case, we find that Γ corresponds to the quotient T2.1 which, given in terms of the generators of $\Delta(2, 3, 8)$, is

$$\Delta(2, 3, 8)/\Gamma = \Delta(2, 3, 8)/\Gamma_{T2.1} = \langle a, b, c \mid a^2, b^2, c^2, x^2, y^3, z^8, zyxz(zx)^{-1}xz \rangle \quad (\text{S67})$$

with $x = ab, y = bc, z = ca$. Using the implementation of this library of normal subgroups in the HYPERCELLS package [61], we compute the kernel of the quotient homomorphism, which gives the corresponding translation group with the simplified presentation

$$\Gamma = \Gamma_{T2.1} = \langle \gamma_1, \gamma_2, \gamma_3, \gamma_4 \mid \gamma_1\gamma_2^{-1}\gamma_3\gamma_4^{-1}\gamma_1^{-1}\gamma_2\gamma_3^{-1}\gamma_4 \rangle \quad (\text{S68})$$

and

$$\gamma_i = z^{5-i}yz^4y^{-1}z^{i-1}. \quad (\text{S69})$$

In GAP [93], we can easily check that Γ is a subgroup of (and thus normal in) $\Delta(4, 4, 4)$. Indeed, with $A = a, B = yay^{-1}$, and $C = y^{-1}ay$ the generators of $\Delta(4, 4, 4)$ and the corresponding rotations $X = AB, Y = BC$, and $Z = CA, \gamma_i, i = 1, 2, 3, 4$, can be written as

$$\gamma_1 = ZY^{-1}X, \quad (\text{S70a})$$

$$\gamma_2 = ZYX^{-1}, \quad (\text{S70b})$$

$$\gamma_3 = Y^{-1}XZ, \quad (\text{S70c})$$

$$\gamma_4 = YX^{-1}Z, \quad (\text{S70d})$$

implying $\gamma_i \in \Delta(4, 4, 4)$.

To apply the supercell method, we construct a sequence of normal translation subgroups $\Gamma^{(m)} \triangleleft \Delta(2, 3, 8), \Gamma^{(m+1)} \triangleleft \Gamma^{(m)}$ with $\Gamma^{(1)} = \Gamma$ using HYPERCELLS [61]. In terms of their quotient groups $\Delta(2, 3, 8)/\Gamma^{(m)}$, they are given as

$$\Delta(2, 3, 8)/\Gamma_{T5.1} = \langle a, b, c \mid a^2, b^2, c^2, x^2, y^3, z^8, z^3yz^{-1}xzy^{-1}xy^{-1}z^{-2}x \rangle, \quad (\text{S71a})$$

$$\Delta(2, 3, 8)/\Gamma_{T17.2} = \langle a, b, c \mid a^2, b^2, c^2, x^2, y^3, z^8, (z^2yx)^2(zx)^{-1}z^{-1}x^2 \rangle, \quad (\text{S71b})$$

$$\Delta(2, 3, 8)/\Gamma_{T33.1} = \langle a, b, c \mid a^2, b^2, c^2, x^2, y^3, z^8, xz^2(zyx)^3z^2y^2z^{-2}xy^{-1}z^{-2} \rangle, \quad (\text{S71c})$$

$$\Delta(2, 3, 8)/\Gamma_{T33.1 \cap T65.1} = \langle a, b, c \mid a^2, b^2, c^2, x^2, y^3, z^8, (xzy^{-1}z^{-2})^2(xz^2yz^{-1})^2, (xz^2y^{-1}z^{-2})^2(xz^3yz^{-1})^2 \rangle. \quad (\text{S71d})$$

The first three were obtained from the library of quotients [61, 63], while the fourth was constructed using the procedure of intersections of normal subgroups [34, 62]. In particular, $\Gamma_{T33.1 \cap T65.1} = \Gamma_{T33.1} \cap \Gamma_{T65.1}$ with $\Delta(2, 3, 8)/\Gamma_{T65.1}$ from Ref. 63. The resulting supercell has genus 129 and as such corresponds to 128 copies of the primitive cell resulting in 2048 sites and 768 plaquettes. The connected and symmetric (super)cells for $m = 1, 2, 3, 4$ are illustrated in Fig. S3.

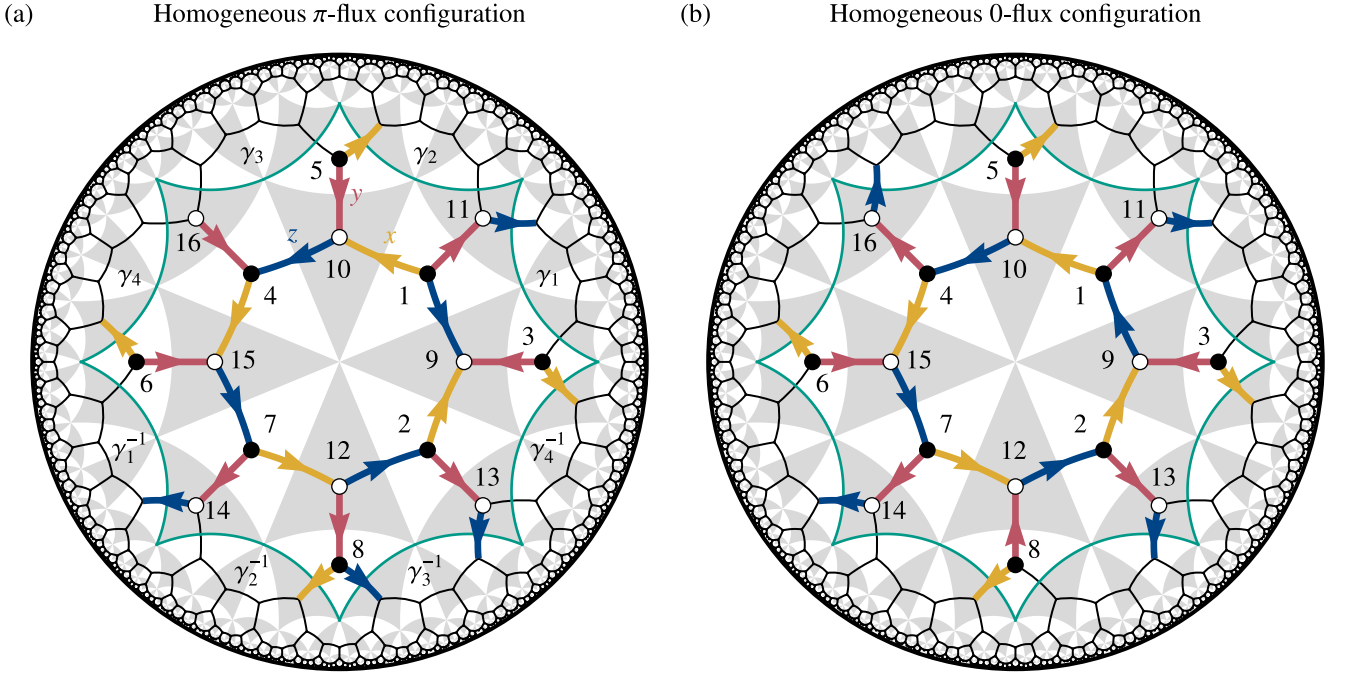


FIG. S4. Gauge choices and site ordering from the homogeneous (a) π - and (b) 0-flux configurations. The choice of gauge, $\{u_{jk}\}$ is indicated by arrows pointing from k to j such that $u_{jk} = +1$. This allows us to easily read off the corresponding eigenvalues of the plaquette operators W_P by going around the plaquette counterclockwise and counting the number of arrows that do not follow that orientation. The numbers by the sites indicate their index in our choice of basis for Eq. (S72). Finally, the translations associated with the boundaries are shown in terms of the translation generators γ_j , $j = 1, 2, 3, 4$.

Given that $\Gamma^{(m)} < \Gamma < \Delta(4, 4, 4) < \Delta(2, 3, 8)$ and $\Gamma^{(m)} \triangleleft \Delta(2, 3, 8)$, we immediately find that $\Gamma^{(m)} \triangleleft \Delta(4, 4, 4)$, as required for compatibility with the symmetric coloring, cf. Section IB. Using the HYPERBLOCH package [64], we then extend the tight-binding model, defined by Eq. (S46), with a choice of gauge $\mathbf{u} = \{u_{jk}\}$ on the primitive cell to the supercells defined by Eq. (S71), following Eq. (S51). Next, we define the corresponding Abelian Bloch Hamiltonian $H(\mathbf{k}^{(m)})$, Eq. (S58), for the one-dimensional irreducible representations $D^{(\mathbf{k}^{(m)})}(\gamma_j^{(m)}) = e^{ik_j^{(m)}}$ defined on the generators $\gamma_j^{(m)}$ of $\Gamma^{(m)}$. Finally, we diagonalize $H(\mathbf{k}^{(m)})$ for 10^5 (in some cases 10^6) randomly sampled momenta $\mathbf{k}^{(m)}$ in the Abelian Brillouin zone $\mathbb{T}^{2g^{(m)}}$, where $g^{(m)}$ is the genus of the surface on which the corresponding supercell is compactified. Based on the resulting sample of eigenvalues, we compute the ground-state energy, density of states, and the spectral gap as detailed below.

While the Hamiltonian in Eq. (S47) is gauge dependent through the choice of gauge $\mathbf{u} = \{u_{jk}\}$ in the definition of the matrix A according to Eq. (S46), the single-particle energies, i.e., the eigenvalues of iA , are explicitly gauge-invariant. They only depend on the corresponding flux sector. However, as we comment in the main text, for a Hamiltonian defined on a PBC cluster with F plaquettes, \mathbf{u} is *not* fully determined by the $F - 1$ independent fluxes through the plaquettes. Instead, the expectation values of the Wilson loop operators along the $2g$ non-contractible loops need to be specified too; we call them the *global fluxes*. The differences in the eigenvalues for different global flux configurations are finite-size effects and vanish in the thermodynamic limit.

On the other hand, hyperbolic band theory explicitly describes eigenstates and energies on the infinite lattice, where there are no global fluxes. Consequently, the flux sector is uniquely determined by the $F - 1$ fluxes through the plaquettes in the unit cell and the single-particle energies $\varepsilon_{\lambda,l}(K)$ only depend on $\{W_P\}_{P=1}^{F-1}$. Operationally, however, the supercell method considers Abelian Bloch Hamiltonians $H(\mathbf{k})$ defined on finite clusters with particular (twisted) boundary conditions specified by \mathbf{k} . To reconcile these two perspectives, note that each global flux precisely corresponds to the shift of momentum \mathbf{k} by π in a particular direction (there are $2g$ directions in the Abelian Brillouin zone). The global fluxes thus only rearrange the blocks $H(\mathbf{k})$ without affecting the full spectrum.

B. Model definition

We define the hyperbolic Kitaev model on the primitive cell and then use Eq. (S51) to extend the definition to any of the supercells (or a compatible PBC cluster or even an OBC flake, see Section V). First, we construct the primitive cell defined by

with $j = 1, 2, 3, 4$,

$$A(\gamma_j \gamma_{j+1}^{-1}) = \begin{pmatrix} 0 & 0 & 0 & 0 & 0 & 0 & 0 & 0 & 0 & 0 & 0 & 0 & 0 & 0 & 0 \\ 0 & 0 & 0 & 0 & 0 & 0 & 0 & 0 & 0 & 0 & 0 & 0 & 0 & 0 & 0 \\ 0 & 0 & 0 & 0 & K\delta_{j5} & 0 & 0 & 0 & 0 & 0 & 0 & 0 & 0 & 0 & 0 \\ 0 & 0 & 0 & 0 & 0 & 0 & 0 & 0 & 0 & 0 & 0 & 0 & 0 & 0 & 0 \\ 0 & 0 & 0 & 0 & 0 & K\delta_{j7} & 0 & 0 & 0 & 0 & 0 & 0 & 0 & 0 & 0 \\ 0 & 0 & 0 & 0 & 0 & 0 & K\delta_{j1} & 0 & 0 & 0 & 0 & 0 & 0 & 0 & 0 \\ 0 & 0 & 0 & 0 & 0 & 0 & 0 & 0 & 0 & 0 & 0 & 0 & 0 & 0 & 0 \\ 0 & 0 & -K\delta_{j3} & 0 & 0 & 0 & 0 & 0 & 0 & 0 & 0 & 0 & 0 & 0 & 0 \\ 0 & 0 & 0 & 0 & 0 & 0 & 0 & 0 & 0 & 0 & 0 & 0 & 0 & 0 & 0 \\ 0 & 0 & 0 & 0 & 0 & 0 & 0 & 0 & 0 & 0 & 0 & 0 & 0 & 0 & 0 \\ 0 & 0 & 0 & 0 & 0 & 0 & 0 & 0 & 0 & 0 & 0 & 0 & 0 & 0 & 0 \\ 0 & 0 & 0 & 0 & 0 & 0 & 0 & 0 & 0 & 0 & 0 & 0 & 0 & 0 & 0 \\ 0 & 0 & 0 & 0 & 0 & 0 & 0 & 0 & 0 & 0 & 0 & 0 & 0 & 0 & 0 \\ 0 & 0 & 0 & 0 & 0 & 0 & 0 & 0 & K\delta_{j4} & 0 & 0 & 0 & 0 & 0 & 0 \\ 0 & 0 & 0 & 0 & 0 & 0 & 0 & 0 & 0 & K\delta_{j2} & 0 & 0 & 0 & 0 & 0 \\ 0 & 0 & 0 & 0 & 0 & 0 & 0 & 0 & 0 & 0 & 0 & 0 & 0 & 0 & 0 \\ 0 & 0 & 0 & 0 & 0 & 0 & 0 & 0 & 0 & 0 & 0 & K\delta_{j8} & 0 & 0 & 0 \end{pmatrix}, \quad (\text{S72d})$$

with $j = 1, 2, \dots, 8$ and $\gamma_{4+i} = \gamma_i^{-1}$. The remaining twelve matrices are defined via

$$A(\gamma^{-1}) = -A(\gamma)^\top. \quad (\text{S72e})$$

Note that the actual calculations [102] have been performed in the gauge obtained from the above choice by performing a single gauge transformation on site 16.

C. Many-body ground-state energy

According to Eq. (S66), the ground-state energy density for a fixed flux sector is given by

$$E_0(\mathbf{u}) = -\frac{1}{2N_s} \sum_{\substack{K, \lambda, \mu, l \\ \varepsilon_{\lambda, l}(K) > 0}} \varepsilon_{\lambda, l}(K), \quad (\text{S73})$$

where N_s is the number of states the sum runs over. Due to $\varepsilon_{\lambda, l}(-K) = -\varepsilon_{\lambda, l}(K)$, cf. Eq. (S63), the above can be rewritten as

$$E_0(\mathbf{u}) = -\frac{1}{4N_s} \sum_{K, \lambda, \mu, l} |\varepsilon_{\lambda, l}(K)|. \quad (\text{S74})$$

Thus, $E_0(\mathbf{u})$ is given simply by the average absolute value of all single-particle energies.

In the context of the supercell method, we restrict the sum to Abelian Bloch states of a given supercell of size N , i.e., consisting of N copies of the primitive cell, and randomly sample N_s momenta from the Abelian Brillouin zone (ABZ). Thus, we actually compute

$$E_0(\{W_P\}) = E_0(\mathbf{u}) = -\frac{1}{4N_s} \sum_{\mathbf{k} \in \text{ABZ}, l} |\varepsilon_l(\mathbf{k})|, \quad (\text{S75})$$

where we indicated that, as discussed above, $E_0(\mathbf{u})$ is gauge-invariant and independent of global fluxes, i.e., depends only on the flux configuration $\{W_P\}$. To capture a representative collection of Bloch states, we apply Eq. (S75) to the sequence of normal subgroups given in Eq. (S71), computing $E_0^{(m)}(\{W_P\})$ for a given Γ -invariant gauge configuration \mathbf{u} on the m^{th} supercell $\Gamma^{(m)}$ consisting of $N^{(m)}$ primitive cells. We subsequently extrapolate $E_0^{(m)}(\{W_P\}) = E_0(N^{(m)}, \{W_P\})$ to infinite supercell size, $N \rightarrow \infty$, obtaining the estimate $E_0(\{W_P\})$ for the given flux configuration $\{W_P\}$. The extrapolation is performed using a weighted least-squares fit with model

$$E_0(N, \{W_P\}) = E_0(\{W_P\}) + \frac{u}{N} + \frac{v}{N^2} \quad (\text{S76})$$

and weights N , excluding the primitive cell $m = 1$. Figure S5 shows the extrapolation for two example flux configurations and illustrates the convergence of the ground-state energy with the inclusion of more non-Abelian states. The resulting estimates for E_0 are given together with the parameter error reflecting the 95% confidence interval. In Section VI, we study this extrapolated value $E_0(\{W_P\})$ systematically for all 32 translation-invariant flux configurations with zero net flux per primitive cell for $K = 0$ and $K = 0.5J$. We find that in both cases the homogenous π -flux has lowest energy.

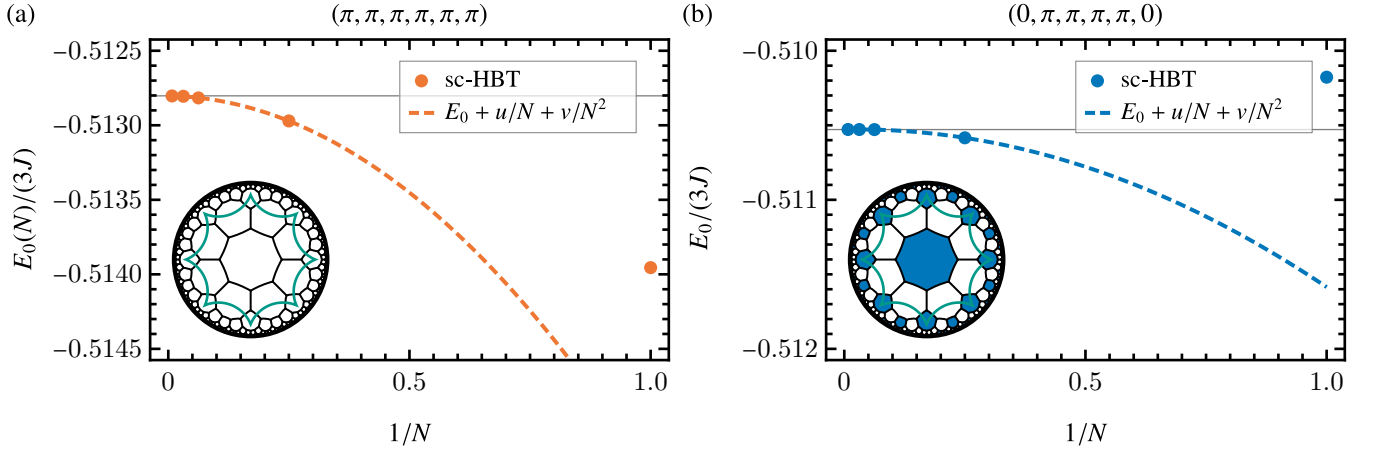


FIG. S5. Extrapolation to the thermodynamic limit E_0 of the ground-state energy $E_0(N)$ obtained from Abelian hyperbolic band theory on a supercell consisting of N primitive cells for two different translation-invariant flux configurations. The data points show the values obtained using Eq. (S75) and the dashed line is a fit according to the model in Eq. (S76). The flux configurations are given in terms of the fluxes through the six plaquettes and illustrated in the bottom left insets with π fluxes shown as white octagons and 0 flux depicted by blue shading. (a) The homogeneous π -flux configuration results in $E_0/(3J) = -0.5128(03 \pm 11)$ from a fit with coefficient of determination $R^2 = 1 - 1.3 \times 10^{-12}$. (b) The flux configuration with next lowest energy has two 0-fluxes per primitive cell (placed at maximal distance to each other) and results in $E_0/(3J) = -0.51052(9 \pm 5)$ from a fit with coefficient of determination $R^2 = 1 - 3.6 \times 10^{-13}$.

D. Density of states

The density of states is obtained by constructing a histogram from the computed eigenvalues. Here, we use an energy-bin-width of $0.002J$ when sampling 10^5 momenta (applicable to most computations) and 0.0002 for 10^6 momenta (when higher resolution was required for the data presented in Fig. S12a). When plotting the density of states, we smooth the data with a moving average with a window of five data points, resulting in an effective energy resolution of $0.01J \approx 0.0033 \times 3J$ and $0.001J \approx 0.00033 \times 3J$, respectively. Some example data at different points in the phase diagram are shown in Section VII; note that only states with $E > 0$ are physical excitations. The convergence of the density of states obtained from the supercell method is studied in Ref. 13.

E. Spectral gap in the thermodynamic limit

Extracting the spectral gap in the thermodynamic limit is impeded by the fact that at least some Bloch states transforming in small-dimensional irreducible representations have vanishing weight in the thermodynamic limit [24]. On the other hand, our calculations exclusively rely on Bloch states transforming in one-dimensional irreducible representations. The resolution of this apparent contradiction lies in the specific choice of sequence in the supercell method that ensures convergence [13, 25]. As a consequence, the spectral gap cannot be simply read off from the spectrum and instead requires an extrapolation to the thermodynamic limit.

The spectral gap $\Delta = 2E_g$ is characterized by a transition from a range of energies $E < E_g$ where the density of states $\rho(E, N)$ decreases with increasing supercell size N to a range $E > E_g$ where $\rho(E, N)$ increases with N . Consequently, the integrated density of states

$$\mathcal{N}(E, N) = \int_0^E dE' \rho(E', N) \quad (\text{S77})$$

is suppressed for $E < E_g$ and enhanced for $E > E_g$, see Fig. S6a. If we consider $\mathcal{N}(E, N)$ as a function of N at fixed energies, as shown in Fig. S6b, we can estimate E_g by extrapolation to $N \rightarrow \infty$. To perform this extrapolation, we fit $\mathcal{N}(E, N)$ as a function of $1/N$ for fixed E in the vicinity of E_g using the linearized model

$$\mathcal{N}(E, N) = \mathcal{N}_0(E) + \frac{s(E)}{N}. \quad (\text{S78})$$

The data points are weighted by N since the spectrum obtained from larger supercells is more representative of the spectrum on the infinite lattice and the primitive cell, $N = 1$, is excluded from the fit altogether.

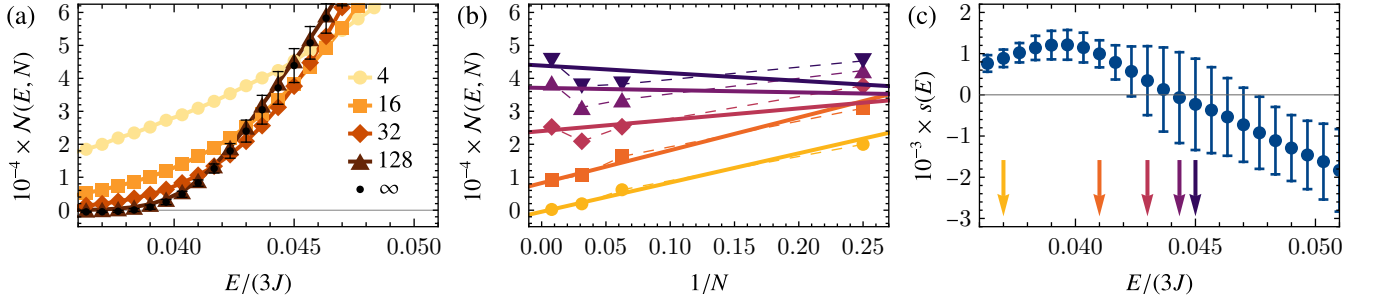


FIG. S6. Estimation of the spectral gap using the supercell method. Integrated density of states $\mathcal{N}(E, N)$ for $J_x = J_y = J_z = J$ and $K/(3J) = 0.1$. (a) $\mathcal{N}(E, N)$ as a function of energy E for different supercells (see inset legend for the supercell size N), including the extrapolated value $\mathcal{N}_0(E)$ (shown as “ ∞ ” in the legend) with 95% confidence intervals shown as error bars. (b) $\mathcal{N}(E, N)$ as a function of $1/N$, i.e., the inverse supercell size, for the values of energy indicated by the correspondingly colored arrows in panel (c). Dashed lines are guides to the eye and the solid lines are linear maximum-likelihood fits. (c) The slope $s(E)$ extracted from the same fits as a function of energy E ; error bars indicated 95% confidence intervals.

Care has to be taken with the actual fitting of $\mathcal{N}(E, N)$ as a function of N , because our estimates of \mathcal{N} are not normally distributed. Ignoring potential correlations from states at the same Abelian momentum, we assume that the N_s randomly sampled states, characterized by energy E , are independent samples from the probability distribution $\rho(E)$, i.e., the density of states. Thus, the probability of finding a state in the energy range $[0, E]$ is precisely the integrated density of states

$$\mathcal{N}(E) = \int_0^E dE' \rho(E'). \quad (\text{S79})$$

The probability of observing n states in that range when sampling a total of N_s states is thus given by the binomial distribution $\mathcal{B}(N_s, \mathcal{N}(E))$:

$$P(n) = \binom{N_s}{n} \mathcal{N}(E)^n (1 - \mathcal{N}(E))^{N_s - n}. \quad (\text{S80})$$

The actual (numerically obtained) values for \mathcal{N} correspond to estimates of the mean of that distribution

$$\hat{\mathcal{N}} = \frac{n}{N_s}. \quad (\text{S81})$$

Therefore, we apply a maximum-likelihood algorithm assuming binomially distributed values to determine the best fit to the model Eq. (S78). This is done using the `GeneralizedLinearModelFit` function in `MATHEMATICA` with the exponential family option set to “`QuasiLikelihood`”, the variance function to $\mu \mapsto \mu(1 - \mu)$ (giving the variance as a function of the mean), the response domain to $[0, 1]$, and the link function to the identity. The result of such a fit for several choices of energy is shown in Fig. S6b.

From each fit, we extract \mathcal{N}_0 and the slope s together with their 95% confidence intervals, see Figs. S6a and S6c, respectively. The extrapolated integrated density of states $\mathcal{N}_0(E)$ is expected to change from 0 to a positive value at E_g . On the other hand, the slope $s(E)$ is expected to change from a positive value below E_g to a negative value above, since a positive value suggests that the corresponding range in energy is depleted of states for $N \rightarrow \infty$, while a negative value suggests that E is outside the gap. From both datasets, we obtain estimates of E_g including uncertainties due to the confidence intervals. Results are shown in Figs. S11a and S12a for the energy gap as a function of J_z and K .

For large enough gaps and if we do not require estimates of the uncertainty, then the described procedure can be simplified by considering only the largest two supercells $N^{(4)}, N^{(5)}$. In that case, the procedure reduces to determining the intersection of $\mathcal{N}(E, N^{(4)})$ with $\mathcal{N}(E, N^{(5)})$ as functions of E . For performance reasons, we used this simplified procedure when computing the full phase diagrams shown in Figs. 2a and 3a in the main text.

V. THE CONTINUED-FRACTION METHOD

The supercell method discussed in Sec. IV provides an efficient way to study hyperbolic lattices directly in the thermodynamic limit. In practice, it is useful, because relatively small cutoffs on the supercell sequence and the momentum sampling produce good approximations. However, near band edges and band degeneracies, the presence of such cutoffs can lead to the sampling of

Bloch states that are strongly suppressed in the thermodynamic limit [13, 34]. Thus, it is helpful to have an alternative method to verify our results. In this section, we provide details on the computation of the single-particle density of states (DOS) using the continued fraction method [65, 66], which was applied recently to nearest-neighbor hyperbolic tight-binding models [24]. To the difference of Ref. 24, which only considered clusters with open boundary conditions (OBC), here we consider clusters with either OBC (Section V A) or periodic boundary conditions (PBC, Section V B). We provide details of the continued-fraction method itself in Section V C, which also introduces modifications to the algorithm of Ref. 24 that are needed to capture the presence of energy gaps [103, 104].

A. Clusters with open boundary conditions (OBC)

To construct large hyperbolic lattices with OBC, we use the procedure detailed in Appendix A of Ref. 19. We use the fact that the $\{8, 3\}$ lattice can be viewed as an $\{8, 8\}$ Bravais lattice with a 16-site basis [19]. In other words, the $\{8, 3\}$ lattice can be generated by acting on a reference unit cell containing 16 sites (black and white dots in Fig. 1a of the main text) with all elements γ of the Fuchsian translation group Γ of the $\{8, 8\}$ lattice. The latter group is a finitely presented infinite group with the presentation already given in Eq. (S68) [see Eq. (S20) for the notion of presentation of a discrete group],

$$\Gamma = \langle \gamma_1, \gamma_2, \gamma_3, \gamma_4 | \gamma_1 \gamma_2^{-1} \gamma_3 \gamma_4^{-1} \gamma_1^{-1} \gamma_2 \gamma_3^{-1} \gamma_4 \rangle. \quad (\text{S82})$$

The elements $\gamma \in \Gamma$ are expressed as words in the generators $\gamma_1, \dots, \gamma_4, \gamma_1^{-1}, \dots, \gamma_4^{-1}$. To generate a finite, rotationally symmetric flake centered around the reference unit cell, we apply to this unit cell all words in Γ of length up to a maximal length p . To eliminate redundancy between different words that correspond to the same element of Γ , we work with the PSU(1, 1) matrix representation of the generators [11], which gives a faithful representation of Γ . This also allows us to compute the complex coordinate $z_\gamma \equiv \gamma(0)$ in the Poincaré disk \mathbb{D} of the center of a unit cell translated by γ from the reference cell centered at $z = 0$. We enumerate all words of length up to $p = 8$, corresponding to a finite OBC cluster with $N = 7\,579\,465$ unit cells and thus $V = 16N = 121\,271\,440$ sites.

Once all distinct translations γ and corresponding $\{8, 8\}$ cell coordinates z_γ have been identified, to construct the Kitaev model on an OBC cluster, we also need to identify nearest-neighbor (NN) and next-nearest-neighbor (NNN) pairs. (Once those are known, NN and NNN pairs on the $\{8, 3\}$ lattice are easily identified.) The hyperbolic distance $d(z, z')$ between two points $z, z' \in \mathbb{D}$, measured in units of the radius of curvature of \mathbb{D} , is defined by [9]

$$\cosh d(z, z') = 1 + \frac{2|z - z'|^2}{(1 - |z|^2)(1 - |z'|^2)}. \quad (\text{S83})$$

Using the PSU(1, 1) matrix representation of the generators, the NN and NNN distances on the $\{8, 8\}$ lattice are found to be

$$\cosh d_{\text{NN}} = 5 + 4\sqrt{2}, \quad \cosh d_{\text{NNN}} = 17 + 12\sqrt{2}. \quad (\text{S84})$$

For each pair $z_\gamma, z_{\gamma'}$ of cell coordinates on the flake, we first compute $d(z_\gamma, z_{\gamma'})$ and find the NN and NNN pairs that satisfy Eq. (S84) within numerical error. Second, for each such pair, we identify the Fuchsian translation $\gamma^{-1}\gamma'$ that relates the two cells, which is either a single generator (for a NN pair) or a product of two generators (for a NNN pair). From the knowledge of those translations, we construct the $16N \times 16N$ matrix A_{jk} appearing in the Majorana Hamiltonian (S47).

B. Clusters with periodic boundary conditions (PBC)

PBC clusters correspond to finite hyperbolic lattices where a certain subset of translations within the primitive translation group Γ are set to the identity, i.e., unit cells differing by those translations are identified, producing a closed lattice without boundaries. Algebraically, a PBC cluster with N unit cells is defined by a choice of normal subgroup Γ' of Γ with (finite) index N , and the unit cells on the cluster are labeled by the cosets Γ/Γ' . Translation symmetry on the finite cluster can be viewed as the action of the finite group Γ/Γ' on itself via the (left-)regular representation [12]. For our calculations on the $\{8, 3\}$ lattice, we generate a PBC cluster with $N = 13\,063\,680$ unit cells ($V = 16N = 209\,018\,880$ sites) by utilizing the method described in the Supplemental Material of Ref. 34. In this method, we compute Γ' as the intersection of several normal subgroups $\Gamma^{(i)}$ of index $|\Gamma : \Gamma^{(i)}| \leq 25$, previously obtained using the low-index normal subgroups procedure [12]. To mitigate finite-size effects, we impose a π flux in each plaquette—given that this is the lowest-energy configuration in the thermodynamic limit (see main text)—even though the particular PBC cluster we work with does not respect all bond-cutting symmetries (i.e., Γ' is not constructed as a normal subgroup of G or K).

For both OBC and PBC clusters, the 16×16 submatrices appearing in A_{jk} are given explicitly in Eq. (S72).

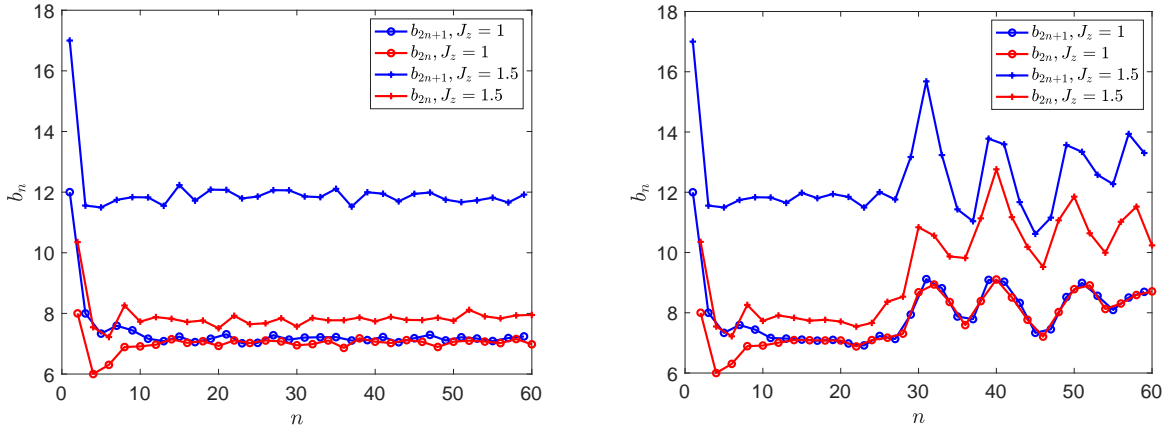


FIG. S7. Continued-fraction coefficients b_n computed on finite hyperbolic lattices for PBC with $V = 209\,018\,880$ sites (left panel); and OBC with $V = 121\,271\,440$ sites (right panel). Here, $J_x = J_y = 1$ and $K = 0$. In the isotropic limit ($J_z = 1$), the odd and even coefficients converge to approximately the same value for $n \geq 15$, indicative of a gapless spectrum. In OBC, the large oscillations for $n \geq 30$ indicate finite-size artefacts from danglings bonds at the boundary, and we estimate b_∞ by averaging over the interval $n \in [15, 20]$. In PBC, we estimate b_∞ by averaging over the interval $n \in [30, 60]$. Over those respective intervals, for $J_z \neq 1$, the odd and even coefficients converge to a different value, indicative of a single spectral gap.

C. The continued-fraction method

The single-particle spectrum is controlled by the eigenvalues of the Hermitian antisymmetric matrix $H_{jk} \equiv iA_{jk}$ in Eq. (S47). From the single-particle Green's function in the site basis $\{|i\rangle\}$,

$$\mathcal{G}_{ij}(z) = \langle i|(z - H)^{-1}|j\rangle, \quad (\text{S85})$$

we obtain the local DOS on site i , $\rho_i(E) = -\frac{1}{\pi} \text{Im} \mathcal{G}_{ii}(E + i0^+)$. For an infinite $\{p, q\}$ lattice, because of lattice symmetries, the local DOS is the same on every site, and we obtain the (global) DOS as

$$\rho(E) = -\frac{1}{\pi} \text{Im} \mathcal{G}_{00}(E + i0^+), \quad (\text{S86})$$

computed on some reference site $i = 0$. In practice, H is the Hamiltonian matrix for a finite cluster with periodic boundary conditions (PBC) or open boundary conditions (OBC), and we choose the reference site to be at the center of the cluster, to mitigate finite-size artefacts introduced by the boundary conditions.

The continued fraction method is a Lanczos-type method which, starting from a normalized state vector $|1\rangle \equiv |0\rangle$ localized on the reference site, constructs an entire new basis $|n\rangle$ via a recursion relation,

$$|n+1\rangle = H|n\rangle - a_n|n\rangle - b_{n-1}|n-1\rangle, \quad n = 1, 2, 3, \dots, \quad (\text{S87})$$

with coefficients a_n and b_n given as

$$a_n = \frac{\langle n|H|n\rangle}{\langle n|n\rangle}, \quad b_n = \frac{\langle n+1|n+1\rangle}{\langle n|n\rangle}, \quad n = 1, 2, 3, \dots, \quad (\text{S88})$$

with $b_0 \equiv 0$. The coefficients are chosen to make the basis orthogonal, and an orthonormal basis is obtained as $|n\rangle \equiv |n\rangle/\sqrt{\langle n|n\rangle}$. In this orthonormal basis, the Hamiltonian is tridiagonal,

$$\langle n|H|n'\rangle = \begin{pmatrix} a_1 & \sqrt{b_1} & & & \\ \sqrt{b_1} & a_2 & \sqrt{b_2} & & \\ & \sqrt{b_2} & a_3 & \ddots & \\ & & & \ddots & \ddots \\ & & & & & \ddots \end{pmatrix}. \quad (\text{S89})$$

For models with a particle-hole symmetric DOS $\rho(E) = \rho(-E)$, as is the case here, all the a_n coefficients vanish identically.

k	Supercell	Continued-fraction (PBC)	Continued-fraction (OBC)
2	3	3	3
4	15	15	15
6	87	87	87
8	537	537	537
10	3 423	3 423	3 423
12	22 239	22 239	22 239
14	146 289	146 289	146 289
16	970 677	970 677	970 677
18	6 482 175	6 482 175	6 482 175
20	43 502 596	43 502 595	43 502 595
22	293 107 927	293 107 916	293 107 916
24	1 981 314 254	1 981 314 166	1 981 314 176
26	13 429 789 221	13 429 788 112	13 429 788 608

TABLE S4. Comparison of (normalized) k th DOS moments $\mu_k/2^k$ obtained from the supercell method (2048 sites, 10^6 momenta, energy resolution 0.0002; rounded to the nearest integer) and the continued-fraction method with PBC and OBC clusters, in the isotropic limit $J_x = J_y = J_z = 1$, $K = 0$. Digits that disagree across methods are highlighted in orange.

$\mathcal{G}_{00}(z)$ is obtained as the 11 element of the Green's function matrix in this basis:

$$\mathcal{G}_{00}(z) = \langle 1 | (z - H)^{-1} | 1 \rangle = \frac{1}{z - \frac{b_1}{z - \frac{b_2}{z - \dots \frac{b_{N-1}}{z - b_N t(z)}}}}, \quad (\text{S90})$$

for a given $N > 1$, where we define the remainder $t(z)$ as the infinite continued fraction

$$t(z) = \frac{1}{z - \frac{b_{N+1}}{z - \frac{b_{N+2}}{z - \dots}}}. \quad (\text{S91})$$

In a gapless system, the sequence b_n converges to a well-defined value $b_\infty \equiv \lim_{n \rightarrow \infty} b_n$ [104]. We compute the b_n coefficients via Lanczos iteration (S87-S88) on a finite hyperbolic lattice with PBC or OBC up to a value $n = N$ until the desired degree of convergence is reached. However, on a finite hyperbolic lattice with V sites, only the first n_{\max} coefficients capture the true bulk physics where n_{\max} grows logarithmically with V [24]. In practice, we compute the coefficients until approximate convergence is reached within a certain range $n_1 < n < n_2$ (see Fig. S7). We then obtain an estimate of b_∞ as the average of the b_n over this range. We then set $b_n = b_\infty$ for all $n > N$ for some chosen $N < n_1, n_2$. Thus, the remainder can be calculated exactly:

$$t(z) = \frac{1}{z - \frac{b_\infty}{z - \frac{b_\infty}{z - \dots}}} = \frac{1}{z - b_\infty t(z)} = \frac{1}{2b_\infty} \left(z - \sqrt{z^2 - 4b_\infty} \right), \quad (\text{S92})$$

upon solving the quadratic equation $(z - b_\infty t)t = 1$ for t , where the negative square root is chosen to ensure $t(z)$ has the correct analytic properties of a Green's function (vanishes as $z \rightarrow \infty$). Since $t(z)$ develops a nonzero imaginary part for $|\text{Re } z| < 2\sqrt{b_\infty}$, the DOS has nonzero support in the interval $-2\sqrt{b_\infty} < E < 2\sqrt{b_\infty}$.

In a system with a (single) gap, the odd coefficients (b_{2n+1}) and even coefficients (b_{2n}) asymptote to two different limits as $n \rightarrow \infty$ [104]. In this case, we choose N to be an even integer, such that the remainder becomes

$$t(z) = \frac{1}{z - \frac{b_\infty^{(o)}}{z - \frac{b_\infty^{(e)}}{z - \frac{b_\infty^{(o)}}{z - \frac{b_\infty^{(e)}}{z - \dots}}}}} = \frac{1}{z - \frac{b_\infty^{(o)}}{z - b_\infty^{(e)} t(z)}}, \quad (\text{S93})$$

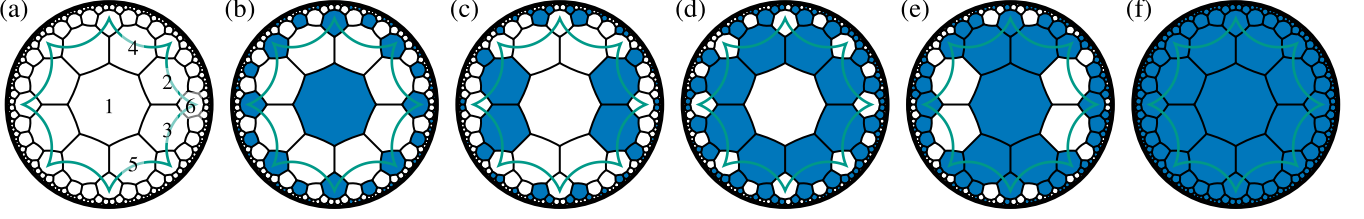


FIG. S8. The six equivalence classes of translation-invariant flux configurations. White (blue shaded) octagons denote plaquettes with π (0) flux, $W_P = -1$ ($W_P = +1$). The following representative flux configurations are shown: (a) $(\pi, \pi, \pi, \pi, \pi, \pi)$, (b) $(0, \pi, \pi, \pi, \pi, 0)$, (c) $(\pi, 0, 0, \pi, \pi, \pi)$, (d) $(\pi, 0, 0, 0, 0, \pi)$, (e) $(0, \pi, \pi, 0, 0, 0)$, and (f) $(0, 0, 0, 0, 0, 0)$, where the plaquette fluxes are given in the order specified by the numbers in panel (a).

having defined $b_\infty^{(o)} \equiv \lim_{n \rightarrow \infty} b_{2n+1}$ and $b_\infty^{(e)} \equiv \lim_{n \rightarrow \infty} b_{2n}$. In practice, we again estimate $b_\infty^{(o)}$ and $b_\infty^{(e)}$ as averages over a suitable interval of (odd/even) n where approximate convergence is observed, together with error bars from the maximum/minimum values of b_n over this convergence interval. The quadratic equation for $t(z)$ in Eq. (S93) can again be solved, yielding

$$t(z) = \frac{1}{2b_\infty^{(e)} z} \left(z^2 - \Delta_\infty - \sqrt{(z^2 - \Delta_\infty)^2 - 4b_\infty^{(e)} z^2} \right), \quad (\text{S94})$$

where we define $\Delta_\infty \equiv b_\infty^{(o)} - b_\infty^{(e)}$. Inspecting the branch points of $t(z)$ as before, we find that the gap in the DOS is given by

$$\Delta E = 2 \left(\sqrt{b_\infty^{(o)}} - \sqrt{b_\infty^{(e)}} \right). \quad (\text{S95})$$

In Figs. S11a and S12a, we plot the gap ΔE together with estimated error bars coming from the maximum/minimum gap over the convergence interval discussed previously. For both PBC and OBC clusters, within the estimated error, we find that the spectrum is gapless in the isotropic limit $J_x = J_y = J_z = J$ and for $K = 0$. Thus, in the main text, we present results in this case that are calculated using the remainder formula (S92) for gapless systems. For $J_z \neq 1$ or $K \neq 0$, we use the two-sided remainder formula (S94).

To compare results obtained from the supercell method (Section IV) vs the continued-fraction method, we compare in Table S4 the moments of the DOS, defined as

$$\mu_k = \int_{-\infty}^{\infty} dE \rho(E) E^k. \quad (\text{S96})$$

Due to the bipartite nature of the $\{8, 3\}$ lattice, the model has a particle-hole symmetry, $\rho(-E) = \rho(E)$, and thus only the even moments are nonvanishing. We compare the even moments from the supercell method, obtained via numerical integration of the DOS, to those obtained from the continued-fraction method (in the isotropic, $K = 0$ limit). For the latter method, we use the fact that for a translation invariant system with V sites,

$$\mu_k = \frac{1}{V} \sum_i \langle i | H^k | i \rangle = \langle 0 | H^k | 0 \rangle = \langle 1 | H^k | 1 \rangle, \quad (\text{S97})$$

with $|0\rangle = |1\rangle$ denoting the localized state at the center of the cluster. The $(1, 1)$ element of the k th power of H is easily computed using the tridiagonal representation of H in Eq. (S89), and only involves b_n coefficients up to $n = k/2$. For the PBC cluster, translation symmetry implies that $\langle i | H^k | i \rangle$ is truly independent of i , while for the OBC cluster, since there is no true translation invariance, $i = 0$ is chosen to mitigate boundary effects. The computation of moments can also be used to benchmark our finite-size clusters. For the simple nearest-neighbor tight-binding model on the $\{8, 3\}$ lattice [24], we find that our PBC (OBC) cluster captures the correct moments up to $k = 22$ ($k = 30$).

VI. GROUND-STATE FLUX SECTOR

In this section, we study the ground-state energy in different flux sectors. For computational reasons, we restrict the analysis to flux configurations that are translation invariant, i.e., invariant under Γ , and have zero net flux per unit cell. This allows us to work with Γ -invariant gauge configurations. Since a primitive cell has six faces and the number of plaquettes with $W_P = -1$ has

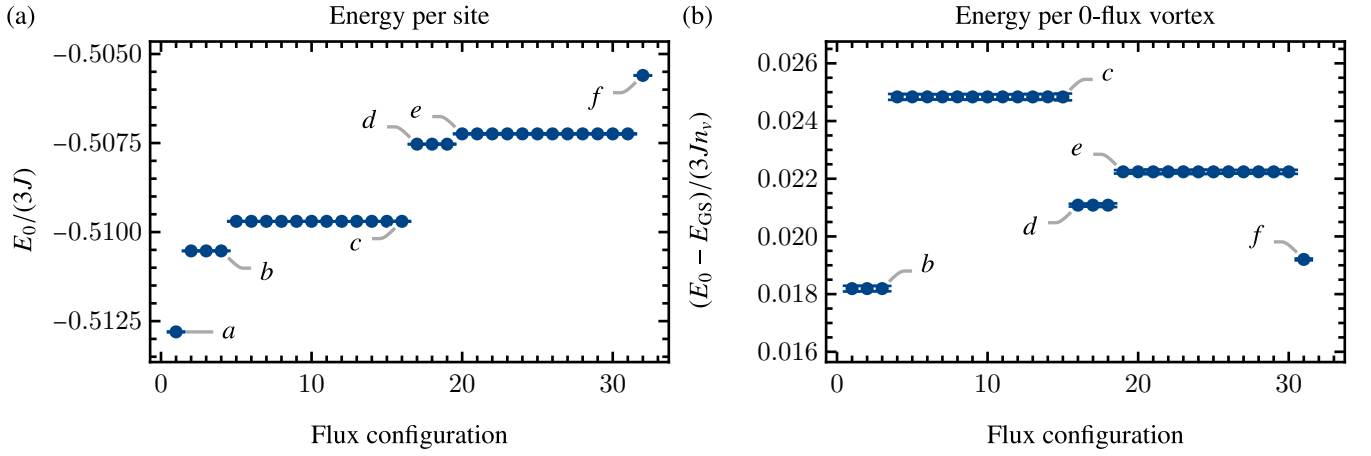


FIG. S9. Ground-state energy for the 32 translation-invariant flux configurations with zero net flux per primitive cell for $J_x = J_y = J_z = J$ and $K = 0$ with error bars indicating 95% confidence intervals. The flux configurations fall into the six equivalence classes shown in Fig. S8 and are labeled by the corresponding panel label. (a) Estimated ground-state energy per site E_0 with errors from the fit Eq. (S76). (b) Energy per 0-flux vortex obtained by computing the energy difference $E_0 - E_{GS}$ between the ground-state energy E_0 of the given flux configuration and E_{GS} , the minimal one (homogeneous π flux), and dividing by the density of vortices n_v in the given configuration.

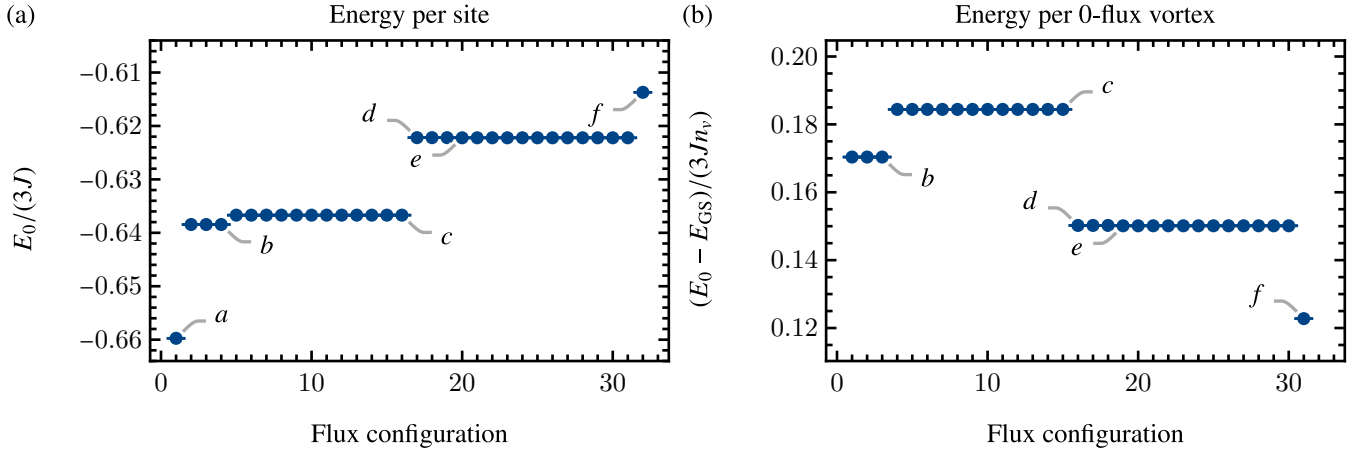


FIG. S10. Ground-state energy for the 32 translation-invariant flux configurations for $J_x = J_y = J_z = J$ and $K = 0.5J$. See Fig. S9.

to be even, there are $2^{6-1} = 32$ such flux configurations. We observe that symmetry further reduces this to the six equivalence classes depicted in Fig. S8.

We first consider the case $K = 0$. As we discussed in the main text, by reflection positivity, the flux configuration with homogeneous π flux has lowest energy. To check this prediction, we explicitly compute the ground-state energy E_0 using the supercell method according to Section IV C for the 32 translation-invariant flux configurations mentioned above. The results are shown in Fig. S9a and demonstrate that indeed the configuration with homogeneous π flux has lowest energy with a gap of $0.0022(74 \pm 12) \times 3J$. Further insights can be gained by computing the energy per vortex (corresponding to a plaquette with flux 0) $(E_0 - E_{GS})/n_v$ for each of the configurations, see Fig. S9b. Here E_{GS} is the the ground-state energy E_0 of the homogeneous π -flux configuration and n_v is the vortex density, i.e., the number of vortices per site. We observe a nontrivial dependence on the distance between the vortices involved in each configuration. The lowest energy per vortex is attained for configurations of the type shown in Fig. S8b, which have two vortices per unit cell spread out symmetrically. This is closely followed by the homogenous 0-flux configuration, Fig. S8f. Curiously, the other configuration with two vortices per unit cell, Fig. S8c, where the vortices are closer to each other, has highest energy.

We repeat the same analysis for $K = 0.5J$ and show the results in Fig. S10. While Lieb's lemma does not apply to the case $K \neq 0$ due to the presence of next-nearest-neighbor terms in the Hamiltonian, we find that the homogeneous π flux still results in the lowest energy. In fact, the gap to the next translation-invariant configuration, which is still Fig. S8b as for $K = 0$, increases by an order of magnitude to $0.02129(7 \pm 4) \times 3J$. Interestingly, there is a rearrangement of the configurations in terms of energy

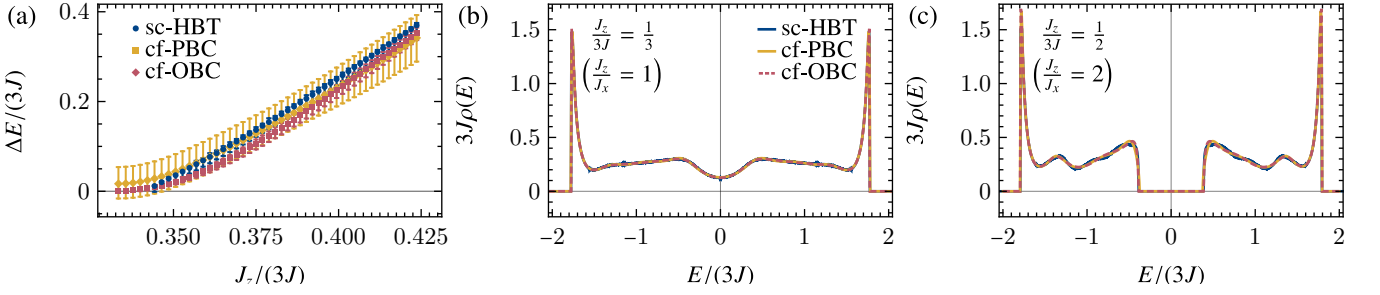


FIG. S11. (a) Spectral gap ΔE including uncertainties shown as error bars as a function of $J_z/(3J)$ for $J_x = J_y$ and $J_x + J_y + J_z = 3J$. The gap opens immediately when departing from the isotropic point $J_z/(3J) = 1/3$. (b,c) Density of states ρ as a function of energy E at (b) the isotropic point (gapless) and (c) $J_z/(3J) = 2$ (gapped). Data obtained using the supercell method (sc-HBT; 2048 sites, moving average window $0.01J$), the continued-fraction method applied to clusters with periodic boundary conditions (cf-PBC; $\sim 10^8$ sites) and to flakes with open boundary conditions (cf-OBC; $\sim 10^8$ sites) is shown, see legend. The density of states obtained from the continued-fraction method explicitly assumes the presence of (b) no and (c) a single gap.

per vortex. While configurations of the class shown in Fig. S8b also had the lowest energy per vortex for $K = 0$, now the homogeneous 0-flux configuration drops significantly below it. This suggests a change in the vortex-vortex interaction potential when increasing K .

VII. FERMIONIC SPECTRUM IN THE HOMOGENEOUS π -FLUX SECTOR

In this section, we present some additional details on the fermionic spectrum in the homogeneous π -flux sector going beyond Figs. 2 and 3. In particular, in Section VII A, we study how the gap opens when departing from the isotropic point $J_x = J_y = J_z$ ($K = 0$) in the phase diagram, demonstrating that indeed the gapless phase exists only at a single point. On the other hand, in Section VII B, we provide additional data on the gap induced by $K \neq 0$ and discuss the complications in extracting the gap at larger K using the continued-fraction method.

A. Gapping by anisotropy

To study the extent of the compressible spin-liquid phase at the isotropic point $J_x = J_y = J_z$ in the absence of the time-reversal-symmetry breaking term, we consider the vertical cut through the parameter space going from the center of the phase diagram towards the top corner: $J_x = J_y$, $J_x + J_y + J_z = 3J$, i.e., $J_x = J_y = 3J(1 - J_z/(3J))/2$. We use the supercell method (see Sections IV D and IV E) as well as the continued-fraction method applied to PBC clusters and OBC flakes (see Section V C) to determine the density of states $\rho(E)$ and the spectral gap ΔE .

The spectral gap is shown in Fig. S11a as a function of J_z close to the isotropic point $J_z/(3J) = 1/3$. Note that no data points for the gap obtained from the supercell method are shown very close to the isotropic point. For those, the algorithm introduced in Section IV E fails to detect a gap, which either implies a truly gapless spectrum (in the thermodynamic limit) or insufficient convergence in the supercell size for extrapolation to work accurately. In this range, we therefore rely on the results obtained from the continued-fraction method which suggests a finite gap at any $J_z \neq J$. Overall, the results obtained from the three methods agree within their respective error bars.

Figures S11b and S11c show the density of states for the two choices $J_z/(3J) = 1/3$ and $J_z/(3J) = 1/2$, respectively, covering the full energy range in contrast to Fig. 2b. We again observe very good agreement between the three methods. Note that in the case of the continued-fraction method, an assumption on the number of gaps needs to be made. This is done based on Fig. S11a, i.e., in Fig. S11b no gap while in Fig. S11c a single gap is assumed.

B. Gapping by time-reversal-symmetry breaking

Similarly, we study the effect of the time-reversal-breaking term, i.e., $K \neq 0$. Figure S12a shows an extension of Fig. 3c, i.e., the spectral gap as a function of K at the isotropic point. As expected from symmetry, we observe that any $K \neq 0$ opens the gap. However, here, we find increasing deviations in the results obtained from the three methods with increasing K . Considering the density of states obtained from the supercell method, Figs. S12b and S12c, we recognize that additional gaps develop away from zero energy. These gaps are *not* captured by our implementation of the continued-fraction method, which assumes at most

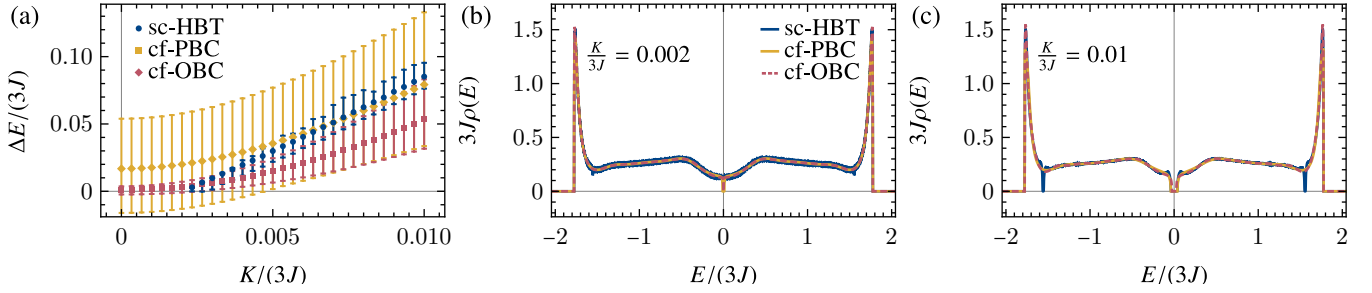


FIG. S12. Spectral gap ΔE and density of states at the isotropic point $J_x = J_y = J_z = J$ for different values of K . See caption to Fig. S11 for more details. Note the two gaps at $E/(3J) \approx \pm 1.55$ that start developing at (b) $K/(2J) \approx 0.002$ and have fully formed (as far as can be discerned from the supercell method at the given resolution) at (c) $K/(3J) = 0.01$. The density of states obtained from the continued-fraction method explicitly assumes the presence of a single gap in both (b) and (c).

a single gap. Multiple gaps can in principle be captured by the method [104]; however, the formalism becomes increasingly complicated and would require even larger system sizes, which are currently not accessible to us. As long as the additional gaps are small enough, we do not expect them to significantly influence the extracted main gap ΔE , but the influence grows with K . In fact, even the density of states away from the gaps is barely affected in Fig. S12c. Thus, the continued-fraction method allows us to extract the gap at small K , where the spectrum obtained from the supercell method is not converged to the necessary resolution in energy, while the supercell method becomes more reliable at larger K .

VIII. GAPPED \mathbb{Z}_2 SPIN LIQUID IN THE ANISOTROPIC COUPLING LIMIT

In this section, we study the hyperbolic Kitaev model [Eq. (1) in the main text] in the anisotropic coupling limit $J_x, J_y \ll J_z$ with $K = 0$. From the phase diagram obtained via the free-fermion solution of the model [Fig. 2a in the main text], we know that in this limit, the fermion sector is gapped. By studying the model directly in the spin-1/2 representation but treating $J_x/J_z, J_y/J_z$ as small parameters, we show here that the model maps in that limit onto an analog of the toric code [70] but on the hyperbolic $\{8, 4\}$ lattice. We find that the latter model is again exactly solvable, and use it to show that the low-energy spectrum contains two types of gapped anyons (e and m particles) with mutual semionic statistics. By adiabatic continuity, this establishes that the entire phase denoted \mathbb{G} in Fig. 2a of the main text is a gapped spin liquid with \mathbb{Z}_2 topological order.

In Section VIII A, we rewrite the $\{8, 3\}$ Kitaev model as a model of effective $s = 1/2$ spins and hard-core bosons on the Archimedean $(8, 4, 8, 4)$ lattice. In Section VIII B, we formulate a perturbative approach to systematically compute an effective Hamiltonian as a power series in the small parameters $J_x/J_z, J_y/J_z$. In Section VIII C, we focus on the limit of low energies $\omega \ll J_z$ (i.e., energies much less than the Majorana fermion gap $E_g = \Delta E/2 \approx 2J_z$) and show that the effective Hamiltonian reduces to a hyperbolic surface code on the $\{8, 4\}$ lattice with (static) anyonic excitations. Throughout this section, we rely heavily on the perturbative methods developed in Ref. 105 and applied in Refs. 68 and 69 to the original Kitaev model on the honeycomb lattice.

A. Mapping to spin-boson model on $(8, 4, 8, 4)$ lattice

In the limit $J_x = J_y = 0$ with $J_z > 0$, the model consists of decoupled dimers with ferromagnetic interactions on the z -bonds of the 3-edge colored $\{8, 3\}$ lattice. The many-body ground state in this limit is macroscopically degenerate, each dimer being in either the $|\uparrow\uparrow\rangle$ or $|\downarrow\downarrow\rangle$ configuration. The lowest excited state above this degenerate ground state corresponds to flipping a single spin on a single dimer, with an energy cost $2J_z$. In the Majorana fermion language, this corresponds to the single-particle gap $\Delta E = 4J_z$ obtained at the corners of the phase diagram in Fig. 2a of the main text [the physical many-body gap is $\Delta E/2$, since only Majorana excitations with energy $\varepsilon > 0$ are physical—see Eq. (S66)]. Here, we are interested in how the macroscopic ground-state degeneracy is lifted upon turning on small exchange couplings $J_x, J_y \ll J_z$. As we will see, this results in a much smaller many-body gap $\Delta \propto J_x^4 J_y^4 / J_z^7 \ll J_z$, corresponding to \mathbb{Z}_2 vortex (or vison) excitations.

The idea [68] is to represent the four possible states of a dimer, including the (ferromagnetic) low-energy states $|\uparrow\uparrow\rangle, |\downarrow\downarrow\rangle$ and the antiferromagnetic (high-energy) states $|\uparrow\downarrow\rangle, |\downarrow\uparrow\rangle$, in terms of an effective spin-1/2 moment $\hat{\tau}$ (with $\hat{\tau}^z$ eigenstates denoted as $|\uparrow\rangle, |\downarrow\rangle$) and a hard-core boson \hat{b}, \hat{b}^\dagger (with occupation number states denoted as 0, 1):

$$|\uparrow\uparrow\rangle = |\uparrow 0\rangle, \quad |\downarrow\downarrow\rangle = |\downarrow 0\rangle, \quad |\uparrow\downarrow\rangle = |\uparrow 1\rangle, \quad |\downarrow\uparrow\rangle = |\downarrow 1\rangle. \quad (\text{S98})$$

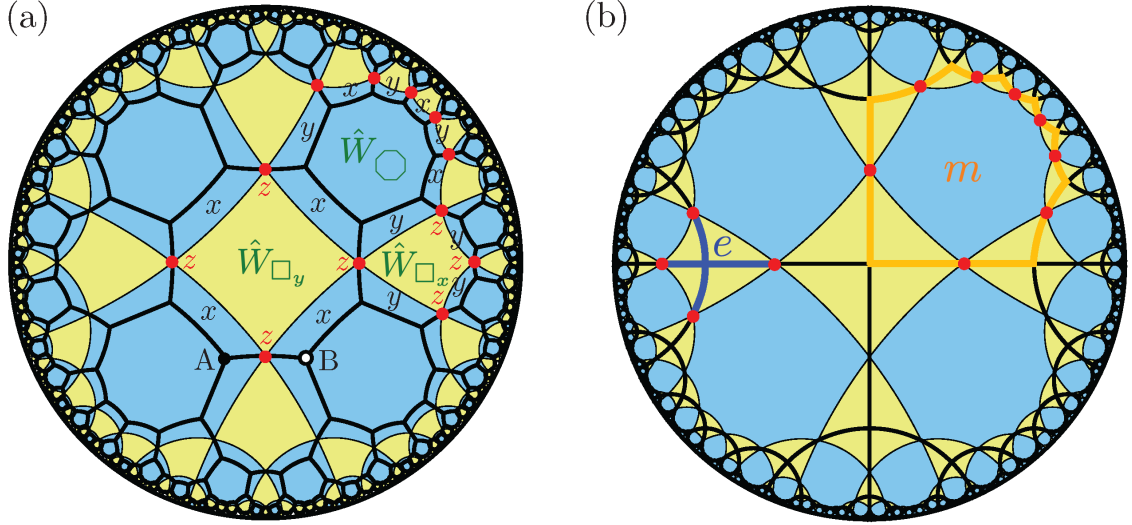


FIG. S13. In the anisotropic coupling limit $J_x, J_y \ll J_z$, the Kitaev model on the $\{8, 3\}$ lattice [black lines in (a)] maps onto a model of effective $s = 1/2$ spins and hard-core bosons on the hyperbolic Archimedean $(8, 4, 8, 4)$ lattice [tiling by blue octagons and yellow squares in (a) and (b), with lattice sites indicated as red dots]. At low energies, this effective model reduces to a hyperbolic analog of the toric code, where spins (red dots) live on the edges of the $\{8, 4\}$ lattice [black lines in (b)]. Low-energy e (m) excitations correspond to star (plaquette) excitations on the $\{8, 4\}$ lattice [blue and orange in (b), respectively] and obey mutual semionic statistics.

As the local Hilbert space dimension on a given dimer is still four, the mapping (S98) does not necessitate the imposition of any local gauge constraint. Here, we use the bipartite property of the $\{8, 3\}$ lattice to assign sublattice (A/B) labels to the two physical spins on any z -bond dimer [black and white dots in Fig. S13a]. The corresponding spin operators can be written as follows in the new representation:

$$\begin{aligned} \hat{\sigma}_A^x &= \hat{\tau}^x (\hat{b}^\dagger + \hat{b}), & \hat{\sigma}_A^y &= \hat{\tau}^y (\hat{b}^\dagger + \hat{b}), & \hat{\sigma}_A^z &= \hat{\tau}^z, \\ \hat{\sigma}_B^x &= \hat{b}^\dagger + \hat{b}, & \hat{\sigma}_B^y &= i\hat{\tau}^z (\hat{b}^\dagger - \hat{b}), & \hat{\sigma}_B^z &= \hat{\tau}^z (1 - 2\hat{b}^\dagger \hat{b}). \end{aligned} \quad (\text{S99})$$

Although this representation explicitly breaks the bipartite symmetry of the lattice, as will be seen, the symmetry will be restored in the effective Hamiltonian.

Collapsing each z -bond to a single effective site on which those new degrees of freedom live, the original Kitaev model is now mapped exactly onto a model of interacting effective spins and hard-core bosons on the hyperbolic Archimedean $(8, 4, 8, 4)$ lattice [Fig. S13a]. An Archimedean $(n_1^{a_1}, n_2^{a_2}, n_3^{a_3}, \dots)$ lattice is a lattice composed of more than one type of regular polygons (here squares and regular octagons), where each vertex is surrounded by an identical sequence of a_1 adjacent n_1 -gons, followed by a_2 adjacent n_2 -gons, followed by a_3 adjacent n_3 -gons, \dots , as one goes clockwise around the vertex [106]. (For example, the Euclidean honeycomb and kagome lattices are (6^3) and $(6, 3, 6, 3)$ Archimedean lattices, respectively.) Using Eq. (S99), the $\{8, 3\}$ Kitaev model can be written as:

$$\hat{\mathcal{H}} = -N_z J_z + 2J_z \hat{Q} + \hat{T}_0 + \hat{T}_2 + \hat{T}_{-2}, \quad (\text{S100})$$

where N_z is the total number of z -bonds,

$$\hat{Q} = \sum_R \hat{b}_R^\dagger \hat{b}_R, \quad (\text{S101})$$

is the total number operator for hard-core bosons, with R denoting the sites of the $(8, 4, 8, 4)$ lattice,

$$\hat{T}_0 = -J_x \sum_{\langle RR' \rangle_x} \hat{b}_R^\dagger \hat{b}_{R'} \hat{\tau}_{R'}^x - J_y \sum_{\langle RR' \rangle_y} \hat{b}_R^\dagger \hat{b}_{R'} i\hat{\tau}_R^z \hat{\tau}_{R'}^y + \text{H.c.}, \quad (\text{S102})$$

is a boson hopping term, and

$$\hat{T}_2 = -J_x \sum_{\langle RR' \rangle_x} \hat{b}_R^\dagger \hat{b}_{R'}^\dagger \hat{\tau}_{R'}^x - J_y \sum_{\langle RR' \rangle_y} \hat{b}_R^\dagger \hat{b}_{R'}^\dagger i\hat{\tau}_R^z \hat{\tau}_{R'}^y, \quad (\text{S103})$$

$$\hat{T}_{-2} = \hat{T}_2^\dagger, \quad (\text{S104})$$

are boson pair-creation/annihilation terms. (Recall that hard-core boson operators obey anticommutation relations for $R = R'$ and commutation relations for $R \neq R'$.) Here, $\langle RR' \rangle_x$ ($\langle RR' \rangle_y$) denote nearest-neighbor x -bonds (y -bonds) on the $(8, 4, 8, 4)$ lattice [see bonds labeled by x (y) between nearest-neighbor red sites in Fig. S13a]. In Eq. (S100), $-N_z J_z$ is the (macroscopically degenerate) ground-state energy in the $J_x = J_y = 0$ limit. As is clear from Eq. (S98), the term proportional to \hat{Q} indicates that creating a boson corresponds to flipping a physical spin on a single dimer, which costs energy $2J_z$. To investigate vison excitations with a gap much less than $2J_z$, we wish to derive an effective Hamiltonian valid in the $Q = 0$ (zero-boson) sector. To achieve this, the strategy [68] is to perform a unitary transformation to a Hamiltonian $\hat{U}^\dagger \hat{H} \hat{U}$ which conserves the boson number \hat{Q} , and evaluate this Hamiltonian in the low-energy sector $Q = 0$.

B. Effective Hamiltonian from perturbation theory

The desired unitary transformation cannot be performed exactly, but it can be performed order by order as a perturbative expansion [105], here in powers of J_x/J_z and J_y/J_z . We refer the reader to the original reference [105] for the details of the method and outline here only the key steps. The method works for Hamiltonians of the type

$$\hat{H} = \hat{H}_0 + \sum_{n=-N}^N \hat{T}_n, \quad (\text{S105})$$

where the unperturbed Hamiltonian $\hat{H}_0 = -N_z J_z + 2J_z \hat{Q}$ is proportional (up to an additive constant term, here $-N_z J_z$) to a ‘‘charge’’ \hat{Q} with nonnegative integer spectrum $0, 1, 2, \dots$, and \hat{T}_n increases this charge by n , i.e., $[\hat{Q}, \hat{T}_n] = n\hat{T}_n$. The operators \hat{T}_n are assumed to be proportional to a common small parameter which controls the perturbative expansion. The outcome of the method is a unitarily equivalent Hamiltonian expressed as a perturbative series,

$$\hat{U}^\dagger \hat{H} \hat{U} = \hat{H}_0 + \sum_{k=1}^{\infty} \sum_{|\mathbf{m}|=k} C(\mathbf{m}) \hat{T}(\mathbf{m}), \quad (\text{S106})$$

where k is the order in perturbation theory. For each k , the second sum is a sum over all k -component vectors $\mathbf{m} = (m_1, m_2, \dots, m_k)$ (indicated by the notation $|\mathbf{m}| = k$) where the entries $m_i \in \{-2, 0, 2\}$, which are the allowed values of n in Eq. (S105) for our case [compare with Eq. (S100)]. Furthermore, one only keeps in the sum the vectors that obey $\sum_{i=1}^k m_i = 0$. Finally, the operators $\hat{T}(\mathbf{m})$ are products of k operators \hat{T}_n specified by the vector \mathbf{m} ,

$$\hat{T}(\mathbf{m}) = \hat{T}_{m_1} \hat{T}_{m_2} \cdots \hat{T}_{m_k}, \quad (\text{S107})$$

and the numbers $C(\mathbf{m})$ are coefficients that are computed using a recursive method [102]. Note that the condition $\sum_{i=1}^k m_i = 0$ implies that the transformed Hamiltonian commutes with the boson number \hat{Q} as desired. Once Eq. (S106) has been evaluated up to a desired order $k_{\max} \geq k \geq 1$ in perturbation theory, we project it onto the $Q = 0$ sector, i.e., we compute its expectation value in the boson vacuum $|0\rangle$ defined by $\hat{b}_R |0\rangle = 0$ for all R :

$$\hat{H}_{\text{eff}} \equiv \langle 0 | \hat{U}^\dagger \hat{H} \hat{U} | 0 \rangle = -N_z J_z + \sum_{k=1}^{k_{\max}} \sum_{|\mathbf{m}|=k} C(\mathbf{m}) \langle 0 | \hat{T}(\mathbf{m}) | 0 \rangle. \quad (\text{S108})$$

Note that \hat{H}_{eff} is still an operator acting in the effective spin Hilbert space, because only the boson degrees of freedom have been projected out.

C. Hyperbolic $\{8, 4\}$ surface code and anyonic excitations

In the $Q = 0$ sector, the only nonconstant contributions to \hat{H}_{eff} in Eq. (S108) come from closed loops, i.e., plaquette operators [68]. In general, \hat{H}_{eff} contains both single-plaquette terms and multi-plaquette interactions. For simplicity, we ignore multi-plaquette interactions here, and focus on the single-plaquette terms which give a toric-code-like Hamiltonian. The $(8, 4, 8, 4)$ lattice itself contains only two types of plaquettes, square and octagonal, but in the general case $J_x \neq J_y$ the effective model distinguishes three types of plaquettes: two square (\square_x, \square_y) and one octagonal (\circ), see Fig. S13a. For single-plaquette terms, the computation is done by considering separately a single plaquette of each type [102]. Starting with the \square_x plaquette, we see from Fig. S13a that it involves four z -sites connected by four y -bonds. To compute the contribution to the effective Hamiltonian (S108) from such a plaquette, it is sufficient to truncate the full Hamiltonian (S100) to a four-site Hilbert space

($R = 1, 2, 3, 4$) with effective spins $\hat{\tau}_1, \dots, \hat{\tau}_4$ and hard-core bosons $\hat{b}_1^{(\dagger)}, \dots, \hat{b}_4^{(\dagger)}$. Thus, for this calculation, only terms involving sites $R, R' \in \{1, 2, 3, 4\}$ need to be kept in the \hat{T}_n operators in Eqs. (S102-S104). To project out the products $\hat{T}(\mathbf{m})$ in Eq. (S108) onto the boson vacuum $|0\rangle$, we work with a $2^4 \times 2^4$ matrix representation of the $\hat{b}_1^{(\dagger)}, \dots, \hat{b}_4^{(\dagger)}$ operators in the Fock basis. In practice, this is conveniently done by viewing hard-core boson Fock states as the binary representation of the integers $0, \dots, 2^4 - 1$ [107]. Since the effective spin degrees of freedom are not projected out, but remain as noncommuting operators obeying the Pauli algebra, we handle them using the DiracQ MATHEMATICA package [108]. Since the \square_x plaquette contains four bonds, we expect the first non-constant term to appear at fourth order in perturbation theory, and indeed we find, omitting a constant correction to the ground-state energy,

$$\hat{\mathcal{H}}_{\text{eff}}^{(\square_x)} = -\frac{5}{16} \frac{J_y^4}{J_z^3} \hat{\tau}_1^x \hat{\tau}_2^x \hat{\tau}_3^x \hat{\tau}_4^x. \quad (\text{S109})$$

Repeating the calculation for the \square_y plaquette with four z -sites connected by four x -bonds [Fig. S13a], we obtain

$$\hat{\mathcal{H}}_{\text{eff}}^{(\square_y)} = -\frac{5}{16} \frac{J_x^4}{J_z^3} \hat{\tau}_1^x \hat{\tau}_2^x \hat{\tau}_3^x \hat{\tau}_4^x, \quad (\text{S110})$$

i.e., the same result but with J_y replaced by J_x . Finally, for the octagonal plaquette with eight z -sites connected by alternating x - and y -bonds, we expect a non-constant contribution $\propto J_x^4 J_z^4 / J_z^7$ at eighth order in perturbation theory,² and indeed obtain,

$$\hat{\mathcal{H}}_{\text{eff}}^{(\bigcirc)} = -\frac{429}{2048} \frac{J_x^4 J_y^4}{J_z^7} \hat{\tau}_1^y \hat{\tau}_2^y \hat{\tau}_3^y \hat{\tau}_4^y \hat{\tau}_5^y \hat{\tau}_6^y \hat{\tau}_7^y \hat{\tau}_8^y, \quad (\text{S111})$$

working with a 2^8 -dimensional boson Hilbert space. Summing over all plaquettes, we obtain the effective Hamiltonian

$$\hat{\mathcal{H}}_{\text{eff}} = -\frac{5}{16} \frac{J_y^4}{J_z^3} \sum_{\square_x} \prod_{R \in \square_x} \hat{\tau}_R^x - \frac{5}{16} \frac{J_x^4}{J_z^3} \sum_{\square_y} \prod_{R \in \square_y} \hat{\tau}_R^x - \frac{429}{2048} \frac{J_x^4 J_y^4}{J_z^7} \sum_{\bigcirc} \prod_{R \in \bigcirc} \hat{\tau}_R^y. \quad (\text{S112})$$

For reasons to be clarified in a moment, we perform one last unitary rotation of all the spins by $\pi/2$ counterclockwise around the x axis, which leaves the $\hat{\tau}^x$ spins unaffected but rotates the $\hat{\tau}^y$ spins into $\hat{\tau}^z$:

$$\hat{\mathcal{H}}_{\text{eff}} \rightarrow -\frac{5}{16} \frac{J_y^4}{J_z^3} \sum_{\square_x} \prod_{R \in \square_x} \hat{\tau}_R^x - \frac{5}{16} \frac{J_x^4}{J_z^3} \sum_{\square_y} \prod_{R \in \square_y} \hat{\tau}_R^x - \frac{429}{2048} \frac{J_x^4 J_y^4}{J_z^7} \sum_{\bigcirc} \prod_{R \in \bigcirc} \hat{\tau}_R^z. \quad (\text{S113})$$

We next show that the plaquette operators appearing in Eq. (S113) are nothing but the Wilson loop operators $\hat{W}_P = \prod_{(j,k) \in P} \hat{\sigma}_j^\alpha \hat{\sigma}_k^\alpha$ introduced in the main text. Going back to the original $\{8, 3\}$ lattice, our choice of 3-edge coloring defines three different types of plaquette operators (as for dimer covering III in Ref. 67), corresponding to the parent octagons for the \square_x , \square_y , and \bigcirc plaquettes introduced earlier. Numbering the sites around an $\{8, 3\}$ plaquette as $j = 1, \dots, 8$, we have

$$\hat{W}_{\square_x} = \hat{\sigma}_1^y \hat{\sigma}_2^y \hat{\sigma}_2^z \hat{\sigma}_3^z \hat{\sigma}_3^y \hat{\sigma}_4^y \hat{\sigma}_4^z \hat{\sigma}_5^z \hat{\sigma}_5^y \hat{\sigma}_6^y \hat{\sigma}_6^z \hat{\sigma}_7^z \hat{\sigma}_7^y \hat{\sigma}_8^z \hat{\sigma}_8^y \hat{\sigma}_1^z = -\hat{\sigma}_1^x \hat{\sigma}_2^x \hat{\sigma}_3^x \hat{\sigma}_4^x \hat{\sigma}_5^x \hat{\sigma}_6^x \hat{\sigma}_7^x \hat{\sigma}_8^x, \quad (\text{S114})$$

$$\hat{W}_{\square_y} = \hat{\sigma}_1^z \hat{\sigma}_2^z \hat{\sigma}_2^x \hat{\sigma}_3^x \hat{\sigma}_3^z \hat{\sigma}_4^z \hat{\sigma}_4^x \hat{\sigma}_5^z \hat{\sigma}_5^x \hat{\sigma}_6^z \hat{\sigma}_6^x \hat{\sigma}_7^z \hat{\sigma}_7^x \hat{\sigma}_8^z \hat{\sigma}_8^x = -\hat{\sigma}_1^y \hat{\sigma}_2^y \hat{\sigma}_3^y \hat{\sigma}_4^y \hat{\sigma}_5^y \hat{\sigma}_6^y \hat{\sigma}_7^y \hat{\sigma}_8^y, \quad (\text{S115})$$

$$\hat{W}_{\bigcirc} = \hat{\sigma}_1^x \hat{\sigma}_2^x \hat{\sigma}_2^y \hat{\sigma}_3^y \hat{\sigma}_3^x \hat{\sigma}_4^x \hat{\sigma}_4^y \hat{\sigma}_5^y \hat{\sigma}_5^x \hat{\sigma}_6^y \hat{\sigma}_6^x \hat{\sigma}_7^y \hat{\sigma}_7^x \hat{\sigma}_8^y \hat{\sigma}_8^x \hat{\sigma}_1^y = -\hat{\sigma}_1^z \hat{\sigma}_2^z \hat{\sigma}_3^z \hat{\sigma}_4^z \hat{\sigma}_5^z \hat{\sigma}_6^z \hat{\sigma}_7^z \hat{\sigma}_8^z. \quad (\text{S116})$$

Next, we map these operators to the spin-boson Hilbert space using the definitions (S99). In the following, $R = 1, \dots, 8$ once again denote sites of the $(8, 4, 8, 4)$ lattice, as in Eqs. (S109-S111). Since the A/B sublattices alternate as we go around each octagon, we obtain

$$\hat{W}_{\square_x} = -\hat{\sigma}_{1,A}^x \hat{\sigma}_{1,B}^x \hat{\sigma}_{2,A}^x \hat{\sigma}_{2,B}^x \hat{\sigma}_{3,A}^x \hat{\sigma}_{3,B}^x \hat{\sigma}_{4,A}^x \hat{\sigma}_{4,B}^x = -\prod_{R \in \square_x} \hat{\tau}_R^x, \quad (\text{S117})$$

$$\hat{W}_{\square_y} = -\hat{\sigma}_{1,A}^y \hat{\sigma}_{1,B}^y \hat{\sigma}_{2,A}^y \hat{\sigma}_{2,B}^y \hat{\sigma}_{3,A}^y \hat{\sigma}_{3,B}^y \hat{\sigma}_{4,A}^y \hat{\sigma}_{4,B}^y = -(-1)^{\sum_{R \in \square_y} \hat{Q}_R} \prod_{R \in \square_y} \hat{\tau}_R^x, \quad (\text{S118})$$

$$\hat{W}_{\bigcirc} = -\hat{\sigma}_{1,A}^z \hat{\sigma}_{2,B}^z \hat{\sigma}_{3,A}^z \hat{\sigma}_{4,B}^z \hat{\sigma}_{5,A}^y \hat{\sigma}_{6,B}^z \hat{\sigma}_{7,A}^z \hat{\sigma}_{8,B}^z = -(-1)^{\sum_{R=2,4,6,8} \hat{Q}_R} \prod_{R \in \bigcirc} \hat{\tau}_R^z. \quad (\text{S119})$$

² At the same order in perturbation theory, we also expect an interaction term between neighboring \square_x and \square_y plaquettes, but we neglect such terms here for simplicity.

Here, $\hat{Q}_R \equiv \hat{b}_R^\dagger \hat{b}_R$ is the boson number operator on site R . We see that \hat{W}_{\square_y} involves the total boson number on plaquette \square_y , while \hat{W}_{\bigcirc} involves only the sum of boson numbers on every other site of plaquette \bigcirc . After projecting to the boson vacuum, we see that the Wilson loop operators (S117-S119) become precisely the plaquette operators appearing in the effective Hamiltonian (S113), such that we can write

$$\hat{\mathcal{H}}_{\text{eff}} = \frac{5}{16} \frac{J_y^4}{J_z^3} \sum_{\square_x} \hat{W}_{\square_x} + \frac{5}{16} \frac{J_x^4}{J_z^3} \sum_{\square_y} \hat{W}_{\square_y} + \frac{429}{2048} \frac{J_x^4 J_y^4}{J_z^7} \sum_{\bigcirc} \hat{W}_{\bigcirc}. \quad (\text{S120})$$

Note that all the (projected) plaquette operators commute with each other.³ We make two observations. Firstly, since all the couplings in Eq. (S120) are positive, the ground state is obtained by setting all plaquette operators \hat{W}_P to -1 , which is consistent with the argument based on Lieb's lemma in the main text. Secondly, setting $J_x = J_y \equiv J_{\parallel} \ll J_z$ for simplicity, we see that the lowest-energy excitation is a \mathbb{Z}_2 vortex on a single \bigcirc plaquette ($\hat{W}_{\bigcirc} = +1$), which costs an energy $E_{\bigcirc}/J_z \propto (J_{\parallel}/J_z)^8$ that is much lower than a vortex excitation on a square plaquette, $E_{\square}/J_z \propto (J_{\parallel}/J_z)^4$.

Finally, we show that the Hamiltonian (S120) can be mapped to a hyperbolic surface code on the $\{8, 4\}$ lattice [Fig. S13b], i.e., a hyperbolic analog of Kitaev's toric code on the square lattice [70]. To achieve this, we simply view the $(8, 4, 8, 4)$ lattice as the medial lattice of the $\{8, 4\}$ lattice (i.e., the lattice obtained by placing sites at the mid-points of the edges of the original lattice). For simplicity, we also set $J_x = J_y \equiv J_{\parallel}$ as in the previous paragraph, which allows us to ignore the difference between x -bonds and y -bonds. Then, we can reinterpret the Hamiltonian (S120) as a model on the $\{8, 4\}$ lattice,

$$\hat{\mathcal{H}}_{\text{eff}} = -J_e \sum_v \hat{A}_v - J_m \sum_p \hat{B}_p, \quad (\text{S121})$$

where $J_e = 5J_{\parallel}^4/(16J_z^3)$ and $J_m = 429J_{\parallel}^8/(2048J_z^7)$ are positive coupling constants, the sum over v (p) is over all vertices (plaquettes/faces) of the $\{8, 4\}$ lattice, and the (commuting) \hat{A}_v and \hat{B}_p operators are defined as

$$\hat{A}_v = \prod_{\ell \in +_v} \hat{\tau}_{\ell}^x, \quad \hat{B}_p = \prod_{\ell \in \partial p} \hat{\tau}_{\ell}^z, \quad (\text{S122})$$

with $+_v$ denoting the ‘‘star’’ of v (i.e., the four edges incident on v) and ∂p the perimeter of the octagonal plaquette p [70]. We note in passing that in the context of quantum information processing, such hyperbolic surface codes have been the object of much interest in recent years [71–76].

As in the original toric code, the hyperbolic code (S121) can be viewed as a fixed-point Hamiltonian for the deconfined phase of a \mathbb{Z}_2 gauge theory on the $\{8, 4\}$ lattice, with $\hat{\tau}_{\ell}^z$ and $\hat{\tau}_{\ell}^x$ corresponding to the \mathbb{Z}_2 gauge and electric fields on link ℓ , respectively. The ground state has $\hat{A}_v = +1$ for all v and $\hat{B}_p = +1$ for all p . The low-energy excitations are static \mathbb{Z}_2 charges (‘‘ e particles’’) with $\hat{A}_v = -1$ on some vertex v , that cost energy $2J_e$, and static \mathbb{Z}_2 fluxes or vortices (‘‘ m particles’’) with $\hat{B}_p = -1$ on some plaquette p , that cost energy $2J_m \ll 2J_e$. Fluxes and charges obey bosonic self-statistics but are mutual semions, which can be seen as follows [68]. Assuming an infinite lattice, consider a nonlocal operator \hat{X} defined as the product of $\hat{\tau}_{\ell}^x$ operators over all links ℓ crossed by a semi-infinite contour C living on the dual lattice (orange contour in Fig. S14):

$$\hat{X} = \prod_{\ell \in C} \hat{\tau}_{\ell}^x. \quad (\text{S123})$$

When applied to the ground state |GS) of Hamiltonian (S121), this operator flips the sign of $\hat{\tau}_{\ell}^z$ on every link crossed, thus it creates a single m flux ($\hat{B}_p = -1$) on the plaquette p where C terminates. If we create two such excitations on different plaquettes, their corresponding string operators obviously commute (being made of products of only $\hat{\tau}^x$ operators), thus the m particles have bosonic self-statistics. Likewise, we define a nonlocal operator \hat{Z} as the product of $\hat{\tau}_{\ell}^z$ operators over all links ℓ traversed by a semi-infinite contour C' living on the $\{8, 4\}$ lattice (blue contour in Fig. S14):

$$\hat{Z} = \prod_{\ell \in C'} \hat{\tau}_{\ell}^z. \quad (\text{S124})$$

This operator flips the sign of $\hat{\tau}_{\ell}^x$ on every link traversed, thus it creates a single e charge ($\hat{A}_v = -1$) on the vertex v where C' terminates. Again, the string operators creating two separate \mathbb{Z}_2 charges commute, thus those particles also obey bosonic self-statistics.

³ This model can thus be viewed as a hyperbolic analog of the Wen plaquette model [109].

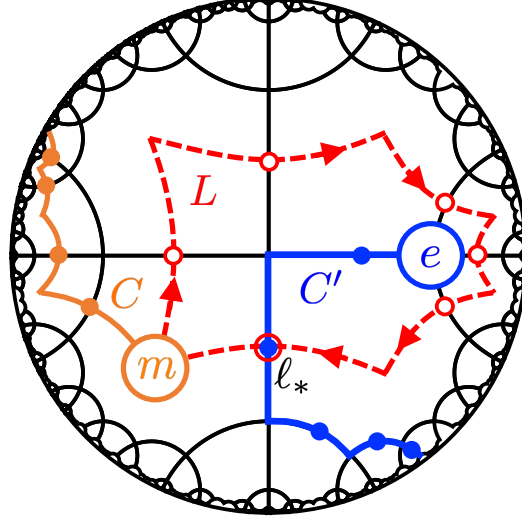


FIG. S14. Mutual anyonic statistics in the $\{8, 4\}$ hyperbolic code. A \mathbb{Z}_2 flux m (charge e) is initially created by a string operator \hat{X} (\hat{Z}) supported on the links (solid dots) crossed by the semi-infinite contour C (C'). The flux is then adiabatically braided around the charge along the closed contour L , which is implemented by a loop operator \hat{X}' with support on the red open circles. The contour L must cross the “Dirac string” C' an odd number of times (here once, on link l_*), resulting in an overall phase factor of -1 which indicates mutual semionic statistics.

Now, begin with the state $|\Psi\rangle = \hat{Z}\hat{X}|\text{GS}\rangle$ containing both m and e particles and consider braiding m around e along a closed contour L (dashed red contour in Fig. S14). Moving m along this contour is accomplished by the operator

$$\hat{X}' = \prod_{\ell \in L} \hat{\tau}_{\ell}^x, \quad (\text{S125})$$

where the product is now only over the red open circles in Fig. S14. We obtain the state $|\Psi'\rangle = \hat{X}'\hat{Z}\hat{X}|\text{GS}\rangle$, but $\hat{X}'\hat{Z} = -\hat{Z}\hat{X}'$ because there is necessarily one link l_* (more generally, an odd number of links) where L and C' cross and thus where $\hat{\tau}_{\ell}^x$ from \hat{X}' and $\hat{\tau}_{\ell}^z$ from \hat{Z} must be anticommutated. Thus, we obtain $|\Psi'\rangle = -\hat{Z}\hat{X}\hat{X}'|\text{GS}\rangle$, using also that \hat{X} and \hat{X}' obviously commute. Finally, \hat{X}' is the product over all $\hat{\tau}_{\ell}^x$ operators crossed by L , and is thus also equal to the product of \hat{A}_v over all vertices v enclosed by L .⁴ (Since all links internal to L appear twice in this product, only links on the perimeter remain.) Since $\hat{A}_v = +1$ for all v in the ground state, we have $\hat{X}'|\text{GS}\rangle = |\text{GS}\rangle$, and thus $|\Psi'\rangle = -|\Psi\rangle$ independent of the detailed shape of the contours C, C', L , apart from their intersections. Thus, an adiabatic phase of -1 is obtained upon braiding an m particle around an e particle, indicating mutual semionic statistics. We conclude that the gapped phase adiabatically connected to the anisotropic coupling limit $J_x, J_y \ll J_z$ is a gapped spin liquid with \mathbb{Z}_2 topological order. For recent studies of hyperbolic lattice models displaying \mathbb{Z}_2 or other types of topological order (e.g., fracton order), also see Refs. 110–113.

Finally, a moment’s thought reveals that the above analysis can be straightforwardly generalized to hyperbolic $\{2m, 3\}$ lattices for any $m \geq 4$, assuming the 3-edge coloring discussed in Section I. One first obtains a spin-boson model on the Archimedean $(2m, m, 2m, m)$ lattice, which is then projected onto a hyperbolic surface code on the $\{2m, m\}$ lattice.

IX. REAL-SPACE CHERN NUMBER

In this section, we discuss the computation of the Chern number for $K \neq 0$ as performed to obtain the data shown in Fig. 4a. We use the real-space Chern number [49], which directly applies to any two-dimensional system, including hyperbolic lattices [20, 28, 29] and even amorphous media [114]. Given a projector P and three regions A, B, C of sites arranged counterclockwise as depicted in Fig. S15a, it is defined as

$$C = 12\pi i \sum_{j \in A} \sum_{k \in B} \sum_{l \in C} (P_{jk}P_{kl}P_{lj} - P_{jl}P_{lk}P_{kj}). \quad (\text{S126})$$

⁴ This can be viewed as a \mathbb{Z}_2 analog of the divergence theorem: \hat{X}' is the net electric flux through L , and $\prod_{v \text{ inside } L} \hat{A}_v$ is the volume integral of the divergence of the electric field. By Gauss’ law, both give the total \mathbb{Z}_2 charge enclosed by L .

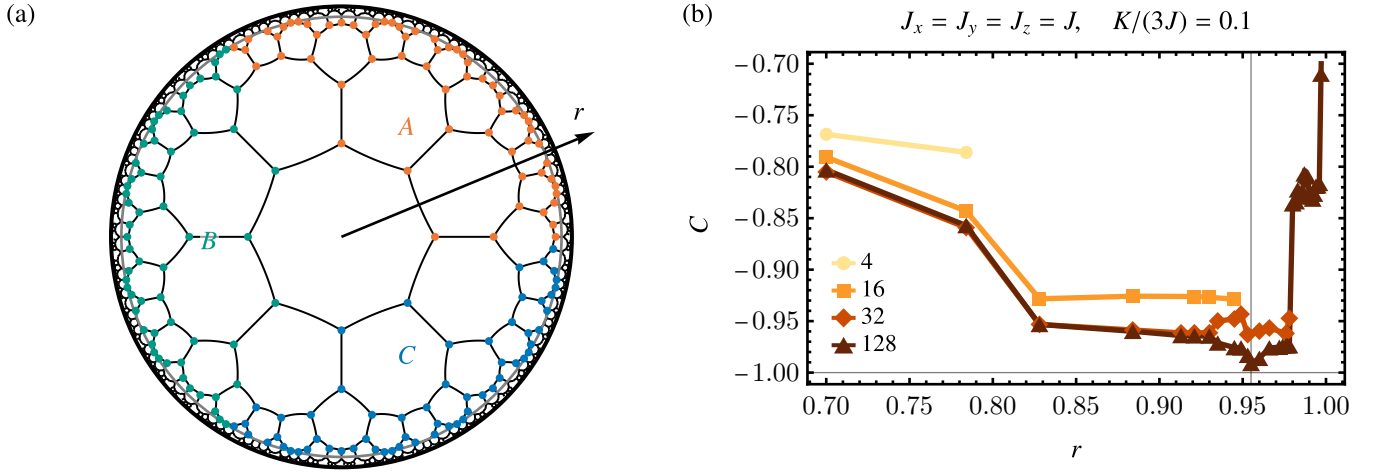


FIG. S15. Computation of the real-space Chern number. (a) 128-primitive-cell PBC cluster $\Gamma_{T33.1}\cap\Gamma_{T65.1}$ (edges shown in black) and the three regions A, B, C (colored sites) up to a bounding radius of $r = 0.955$ (gray circle). (b) Real-space Chern number C at the isotropic point for $K \neq 0$ as a function of bounding radius r for different PBC clusters; their size in terms of number of primitive cells is given in the inset legend. Note that sites within the bounding circle that have nearest-neighbor bonds that connect to the other side of the projection are discarded. The Chern number converges closer to the true value with increasing region size up to a point from which on the result gets poisoned by the periodic boundary conditions.

While this is often applied to systems with open boundary conditions, we here perform the calculation on PBC clusters. In the former case, the regions A, B, C have to be chosen sufficiently far away from the boundary, to avoid boundary effects, which would compensate the bulk and result in a trivial Chern number. On PBC clusters this is similar: we have to constrain the regions such that they are sufficiently separated and do not wrap around the higher-genus surface on which the PBC cluster is embedded.

To select these regions, we work in the Poincaré disk representation and use the fact that any of the supercells described in Section IV A can be interpreted as a finite PBC cluster [62] by considering the quotient $\Gamma/\Gamma^{(m)}$ and then following Section V B. Starting from the symmetric supercell constructed using the HYPERCELLS package [61], this allows us to immediately obtain a symmetric *projection* of the PBC cluster onto the Poincaré disk. When defining the regions A, B, C , we only include sites lying within a given bounding radius r and explicitly exclude sites that have nearest-neighbor bonds that connect to the other side of the projection. Figure S15a shows this construction for the 128-primitive cell PBC cluster defined by $\Gamma_{T33.1}\cap\Gamma_{T65.1}$ given in Eq. (S71d). A priori, it is not clear which r is optimal for approximating the Chern number in the thermodynamic limit, such that we study the Chern number as a function of r on different PBC clusters and choose the maximal r up to which $C(r)$ is monotonic, see Fig. S15b. For the largest PBC cluster, we find an optimal bounding radius of $r = 0.955$ (gray vertical line).

To evaluate Eq. (S126), we need the projector onto the occupied subspace, which we obtain by exact diagonalization of the model Hamiltonian iA on the given PBC cluster. With eigenstates $|n\rangle$ and eigenenergies $\varepsilon_n \neq 0$ (assuming a spectral gap such that the Chern number is well-defined), the projector is

$$P = \sum_{n: \varepsilon_n < 0} |n\rangle\langle n|. \quad (\text{S127})$$

Its matrix elements $P_{jk} = \langle z_j | P | z_k \rangle$ in the real-space basis $|z_j\rangle$ with z_j the position of site j in the Poincaré disk then enter Eq. (S126). In practice, we can obtain this projector from the spectrally flattened Hamiltonian

$$B = -i \operatorname{sgn}(iA), \quad (\text{S128})$$

where sgn only acts on the eigenvalues, as

$$P = \frac{1}{2}(1 - iB). \quad (\text{S129})$$

At the isotropic point $J_x = J_y = J_z = J$, $K/(3J) = 0.1$, i.e., the choice of K in Fig. 3 in the main text, and with the optimal radius $r = 0.955$, we find that C converges to -1 with increasing supercell size N , see Fig. S16a. Figure S16b shows a cut through the phase diagram shown in Fig. 4a along $J_x = J_z$. Besides the Chern number (blue, left axis), we also show the finite-size gap (orange, right axis). We recognize that the washed-out phase boundary pointed out in the main text is caused by several jumps of C with intermediate non-integer values. These jumps occur precisely when the finite-size gap closes (gray vertical lines) and correspond to the transfer of individual states from negative to positive energy or vice versa.

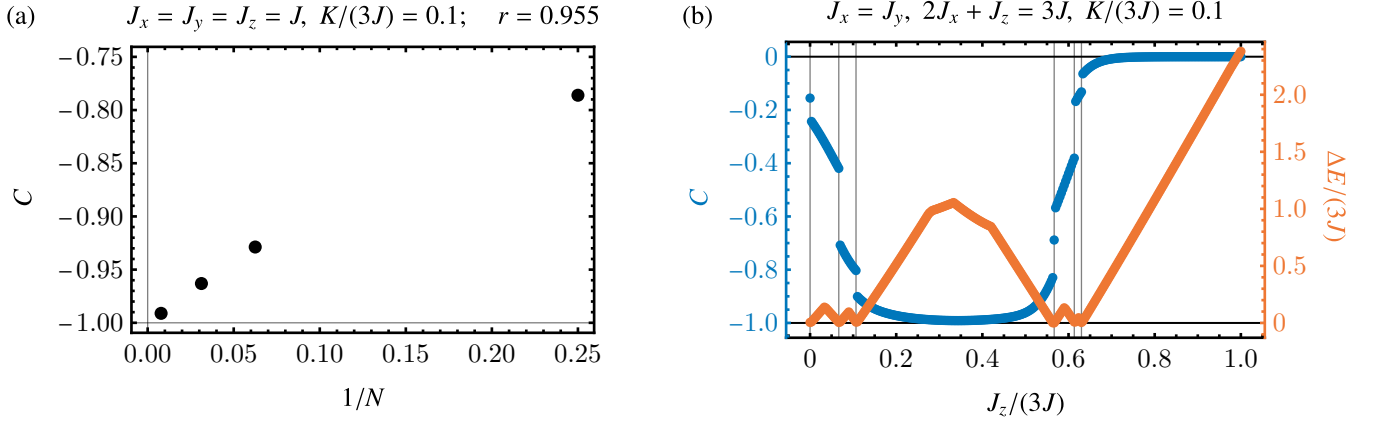


FIG. S16. Results on the real-space Chern number. (a) Convergence with size N (in terms of number of primitive cells) of the PBC cluster at the isotropic point with $K/(3J) = 0.1$ and bounding radius 0.955. The value approaches -1 . (b) Cut through the phase diagram of the Chern number C along $J_x = J_z$ as a function of J_z for $K/(3J) = 0.1$ obtained on the 128-primitive-cell PBC cluster shown in Fig. S15a. In the thermodynamic limit, the Chern number (blue, left axis) is quantized to integers (horizontal black lines at 0, -1) as long as there is a gap ΔE . Due to finite-size effects, there are deviations from the integer values in regions where ΔE is small. More precisely, the closing of the thermodynamic gap is replaced by multiple closings (indicated by vertical gray lines) of the finite-size-gap (orange, right axis) resulting in several jumps of C with non-integer values.

X. CHIRAL EDGE STATES

In this section, we clarify the method used to extract the angular dispersion of the edge state, displayed in Fig. 4b of the main text. When an open boundary is introduced in the chiral gapped (χ) phase, owing to the nonzero Chern number, we expect the model should develop gapless edge states inside the bulk energy gap. We illustrate the appearance of such states explicitly in Fig. S17a by comparing the density of states (DOS) in the bulk vs on the boundary of a disk-shaped sample. To further manifest the boundary character of the in-gap states, we compute for each eigenstate $|\psi_n\rangle$ with energy E_n the quantity:

$$p_{n,\text{edge}} = \sum_{j \in \text{edge}} |\psi_n(j)|^2, \quad (\text{S130})$$

where by “ $j \in \text{edge}$ ” we mean sites located within the outer 10% of the hyperbolic distance to the disk boundary, and $\psi_n(j) = \langle j | \psi_n \rangle$. Similarly, we define the bulk sites “ $j \in \text{bulk}$ ” as those located within the inner 65% of the hyperbolic distance to the disk boundary. By representing each state $|\psi_n\rangle$ as a point with coordinates $(p_{\text{edge},n}, E_n)$ in Fig. S17b, we recognize that all states with energy $|E|/(3J) \lesssim 0.6$ exhibit a significantly larger value of p_{edge} than the states at larger values of $|E|$. All calculations in this section are performed with a system containing all 896 sites of the $\{8, 3\}$ lattice located within 99.14% of the radius of the Poincaré disk (the same as used in Ref. 29 when extracting the chiral edge mode dispersion of a hyperbolic Haldane model). To realize the chiral gapped phase, we set the model parameters to $J := J_{x,y,z} = \frac{1}{3}$ and $K = \frac{1}{10}$.

Near zero energy, we expect the topological edge mode to exhibit an approximately linear dispersion $E \propto \ell$, where ℓ is angular momentum [78, 79]. However, owing to the discreteness of the underlying $\{8, 3\}$ lattice, angular momentum of the individual eigenstates is well-defined only modulo the order of the rotation symmetry, i.e., mod 8, implying an impractically narrow edge Brillouin zone. To obtain the dispersion over an extended range of angular momenta ($-150 \leq \ell \leq 150$ in Fig. 3 of the main text), we need to devise a physically motivated approximation that treats the discrete lattice as a continuum.

Recall that the angular momentum operator is given by $\hat{\ell} = -i\partial_\varphi$ where φ is the angle in polar coordinates. On a disk with continuous $\text{SO}(2)$ rotation symmetry, angular momentum is a well-defined quantum number. The complex phase of the eigenstates of $\hat{\ell}$ must grow linearly with φ , i.e., they are of the form $|\psi_\ell\rangle \propto e^{i\ell\varphi}$, where ℓ is the angular momentum eigenvalue. To verify that this property also holds with good accuracy for the edge states on the discrete graph, we explicitly plot the dependence of the complex phase $\arg[\psi_n(j)]$ on the angular coordinate $\varphi(j)$ of sites j for several eigenstates $|\psi_n\rangle$ with energy E_n close to zero. The result, shown in Fig. S18a, confirms that the complex phase exhibits a well-defined slope corresponding to a half-integer angular momentum, $\ell \in \mathbb{Z} + \frac{1}{2}$, as expected for a chiral Majorana edge mode [78, 79]. The data in Fig. S18a also suggests that the slope ℓ grows with energy E for the Majorana edge modes near $E = 0$.

To establish the linear dispersion $E(\ell)$ of the edge states over a wider energy range, we devise the following scheme to estimate the angular momentum of the individual eigenstates. Assuming that $\ell \in \mathbb{Z} \cup (\mathbb{Z} + \frac{1}{2}) \cong \frac{1}{2}\mathbb{Z}$, we compute for each normalized

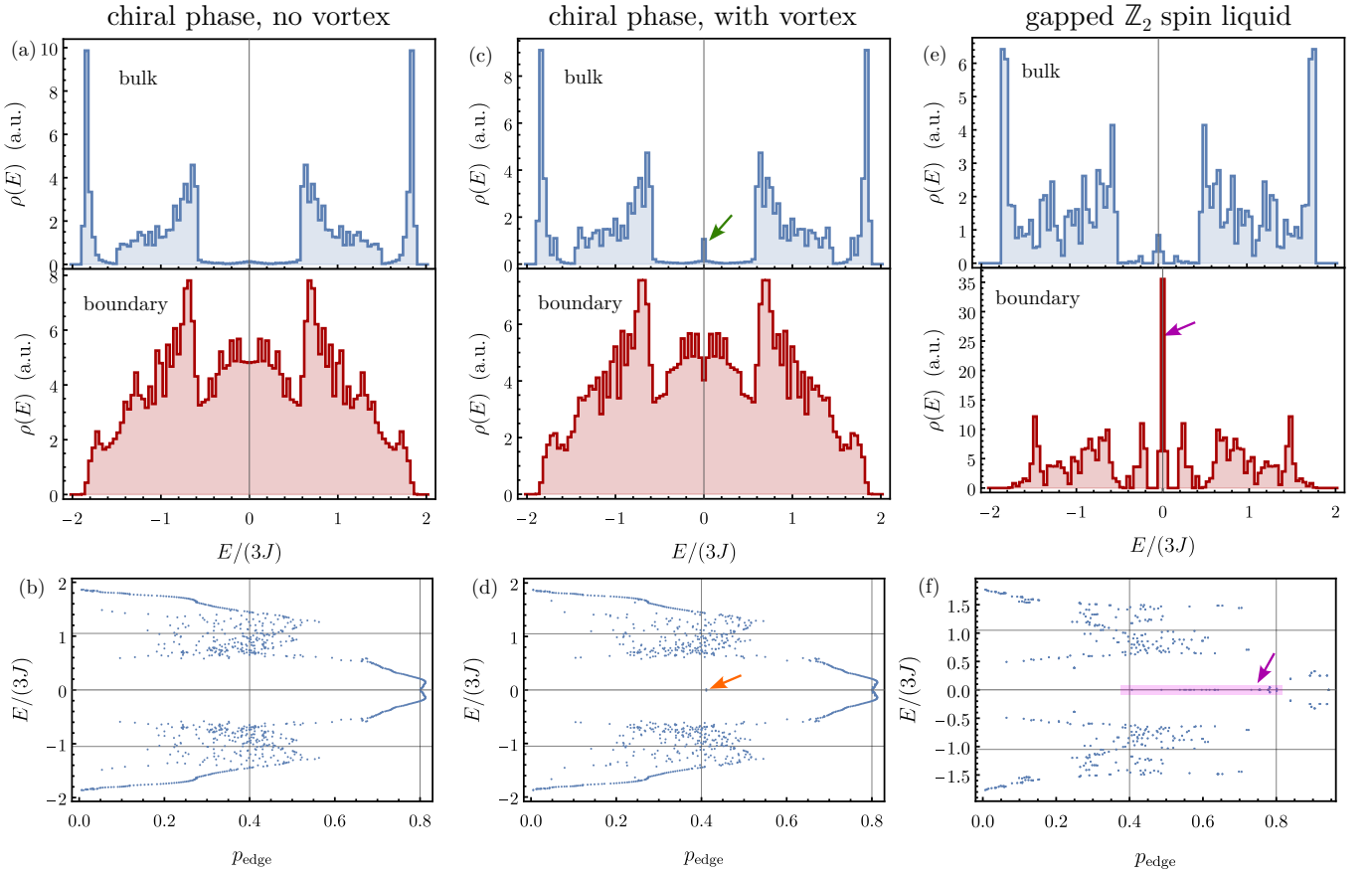


FIG. S17. (a) Density of states (DOS) $\rho(E)$ of the chiral gapped phase on a disk with 896 sites and open boundary conditions, with model parameters set to $J := J_{x,y,z} = \frac{1}{3}$ and $K = \frac{1}{10}$, plotted in arbitrary units (a.u.). The “bulk DOS” (shown in blue) is obtained by summing the local DOS over sites located within the inner 65% of the hyperbolic distance to the disk boundary, whereas in “boundary DOS” (shown in red) we sum over sites within the outer 10% of the hyperbolic distance to the disk boundary. (b) Each eigenstate is represented as a dot with coordinates (p_{edge}, E) , where p_{edge} is a measure of edge localization defined in Eq. (S130). Edge states are recognized as the arc of dots on the right side of the plot. Vertical grid lines indicate the values at which we saturate the color scheme in Fig. 4b of the main text and in Fig. S19, and the horizontal grid lines indicate the energy range adopted in the said figures. (c,d) Analogous data in the presence of a \mathbb{Z}_2 vortex threaded through the plaquette located at the center of the disk. The vortex binds a zero-energy Majorana mode, resulting in a small peak in the bulk DOS at $E = 0$ [indicated with green arrow in panel (c)]. Due to finite-size effects, the Majorana mode at the vortex hybridizes with a zero-energy Majorana mode at the boundary, thus acquiring an enhanced value of p_{edge} [indicated with orange arrow in panel (d)] and a small finite energy $E/(3J) \approx \pm 0.0138$. (e,f) For comparison, we also show the analogous data for the gapped Abelian \mathbb{Z}_2 spin liquid, which carries vanishing Chern number, for parameters $J_x = J_y = 1/4$, $J_z = 1/2$, and $K = 0$. We observe that the gapped \mathbb{Z}_2 spin liquid phase also exhibits edge states within the bulk energy gap, including a flat band at $E = 0$ (indicated with purple arrow). We find that these zero-energy boundary states have a large localization length, making the $E = 0$ peak also visible in the numerically computed bulk DOS. However, we demonstrate in Fig. S20c that edge states of the trivial gapped phase do not exhibit chiral propagation, in accordance with the vanishing Chern number.

eigenstate $|\psi_n\rangle$ and each $\ell \in \frac{1}{2}\mathbb{Z}$ the coefficient

$$c_{n,\ell} = \left| \sum_j e^{-i2\ell\varphi(j)} \psi_n^2(j) \right| \in [0, 1], \quad (\text{S131})$$

which we interpret as the likelihood that the state $|\psi_n\rangle$ carries angular momentum ℓ . This is motivated by the fact that for the exact eigenstate $|\psi_{(\ell')}\rangle \propto e^{i\ell'\varphi}$ localized on the boundary of a continuous disk, an analogous integration gives $c_{(\ell'),\ell} = \delta_{\ell',\ell}$. The result of this analysis, plotted in Fig. S19a (also Fig. 4b in the main text), reveals that the edge states (displayed in red tones) build up a chiral mode with half-integer angular momentum eigenvalues in range $-90 \lesssim \ell \lesssim 90$. In addition, owing to the discreteness of the lattice, we observe several replicas of the chiral mode whose angular momentum is displaced by integer multiples of 4 [that the ambiguity is mod 4 rather than mod 8 follows from the squaring of the wave function amplitude in Eq. (S131)]; nevertheless, the main branch passing through $(E, \ell) = (0, 0)$ dominates in intensity over all replicas for all edge states. In addition, we clearly recognize that the bulk states (displayed in blue tones) do not carry a well-defined $\ell \in \frac{1}{2}\mathbb{Z}$, making the plotted data featureless at

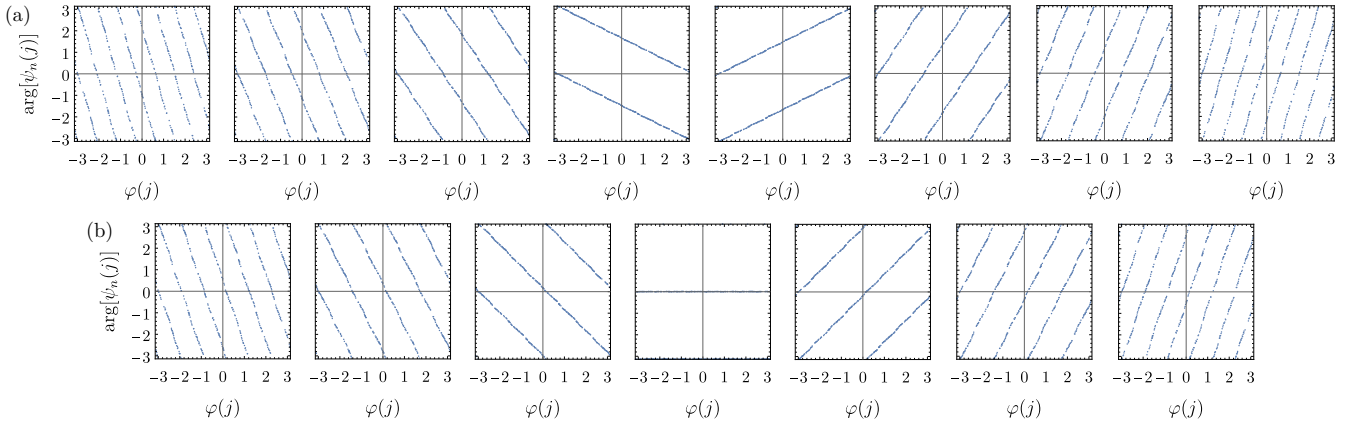


FIG. S18. (a) Plots showing the linear growth of the phase $\arg[\psi_n(j)]$ with the angular coordinate $\varphi(j)$ of site j for several eigenstates $|\psi_n\rangle$ with near-zero energy. Each plot correspond to a single normalized eigenstate, and the energy of the eigenstates grows from negative (on the left) to positive (on the right). We display data points only for sites j with $|\psi_n(j)|^2 > 1/(2N)$ where $N = 896$ is the number of sites in the disk. The observed linear slopes imply that the chiral edge states carry half-integer angular momentum, $\ell \in \mathbb{Z} + \frac{1}{2}$. (b) Analogous data in the presence of a \mathbb{Z}_2 vortex threaded through the central plaquette and with a perturbation that shifts the Majorana mode at the vortex to energy $E/(3J) \approx 1$. In this case, the angular momentum of the chiral edge states is shifted to integer values, $\ell \in \mathbb{Z}$.

energies $|E|/(3J) \gtrsim 0.6$.

We next investigate the edge states of the chiral gapped phase in the presence of a \mathbb{Z}_2 vortex threaded through the plaquette at the center of the disk. We observe in Figs. S17c and S17d that this results in a minimal but important change in the bulk and boundary DOS functions. Namely, the bulk DOS develops a small peak at $E = 0$ [indicated by the green arrow in panel (c)] whereas the boundary DOS develops a correspondingly small dip at the same position. Furthermore, the dispersion analysis, shown in Fig. S19b, reveals that the angular momentum of the Majorana edge states has been shifted to integer values, $\ell \in \mathbb{Z}$, and that the $\ell = 0$ Majorana edge state is missing. These observations are explained by the formation of a Majorana mode bound to the vortex. If the vortex were sufficiently far from the boundary, we would expect a vortex-bound Majorana mode $|\psi_0^{\text{vortex}}\rangle$ to occur at $E = 0$. Due to finite-size effects (for the adopted system size, the shortest path from the vortex to the boundary consists of only seven edges of the $\{8, 3\}$ lattice) we expect the vortex-bound Majorana mode to hybridize with the $E = 0$, $\ell = 0$ Majorana state $|\psi_0^{\text{edge}}\rangle$ on the boundary. The two resulting hybridized states $|\psi_0^{\text{mixed},1}\rangle$ and $|\psi_0^{\text{mixed},2}\rangle$ both have a large support on the bulk sites, and we observe them in Fig. S17d at $E/(3J) \approx \pm 0.0138$ and $p_{\text{edge}} \approx 0.42$ (indicated by the orange arrow). This shared bulk character also explains the dip observed in the boundary DOS in Fig. S17c. In addition, since the vortex-bound Majorana mode $|\psi_0^{\text{vortex}}\rangle$ is strongly localized on a single octagonal plaquette at the center, its coefficients $c_{n,\ell}$ computed according to Eq. (S131) will exhibit strong peaks at all $\ell = 0 \pmod{4}$. This ill-defined value of the angular momentum is shared by the hybridized Majorana states $|\psi_0^{\text{mixed},1}\rangle$ and $|\psi_0^{\text{mixed},2}\rangle$ found in the numerics, as visible in the data near $E = 0$ in Fig. S19b.

To remove these finite-size effects from the numerics, we apply a perturbation to the Hamiltonian as follows. First, we numerically find linear combinations

$$\begin{pmatrix} |\psi_0^{\text{unmixed},1}\rangle \\ |\psi_0^{\text{unmixed},2}\rangle \end{pmatrix} = M \begin{pmatrix} |\psi_0^{\text{mixed},1}\rangle \\ |\psi_0^{\text{mixed},2}\rangle \end{pmatrix} \quad (\text{S132})$$

with $M \in \text{U}(2)$ such that $|\psi_0^{\text{unmixed},1}\rangle$ exhibits the maximal possible value of localization to the boundary p_{edge} [Eq. (S130)]. We interpret the constructed $|\psi_0^{\text{unmixed},1}\rangle$ as $|\psi_0^{\text{edge}}\rangle$ and the constructed orthogonal $|\psi_0^{\text{unmixed},2}\rangle$ as $|\psi_0^{\text{vortex}}\rangle$. We plot the computed state $|\psi_0^{\text{unmixed},2}\rangle \approx |\psi_0^{\text{vortex}}\rangle$ in Fig. S20a. Then we perturb the Hamiltonian by adding a term proportional to the projector onto $|\psi_0^{\text{vortex}}\rangle$; specifically:

$$H' = H + H_{\text{pert.}} \quad \text{where} \quad H_{\text{pert.}} = 3J |\psi_0^{\text{unmixed},2}\rangle \langle \psi_0^{\text{unmixed},2}|. \quad (\text{S133})$$

We anticipate such a perturbation to shift the vortex-bound Majorana mode to finite energy $E/(3J) \approx 1$, leaving behind a well-defined Majorana edge state with $E = 0$, $\ell = 0$. This expectation is confirmed by the edge dispersion data shown in Fig. S19c. Correspondingly, the complex phase $\arg[\psi_n(j)]$, plotted as a function of the angular coordinate $\varphi(j)$ of sites j in Fig. S18b, exhibits for eigenstates $|\psi_n\rangle$ with energy near $E = 0$ the expected linear growth with integer slopes, in accordance with $\ell \in \mathbb{Z}$.

The chiral character of the Majorana edge modes in the chiral gapped phase can also be illustrated through the propagation of a wave packet localized at the boundary. To that end, we return to the simpler case without a vortex, and we construct the

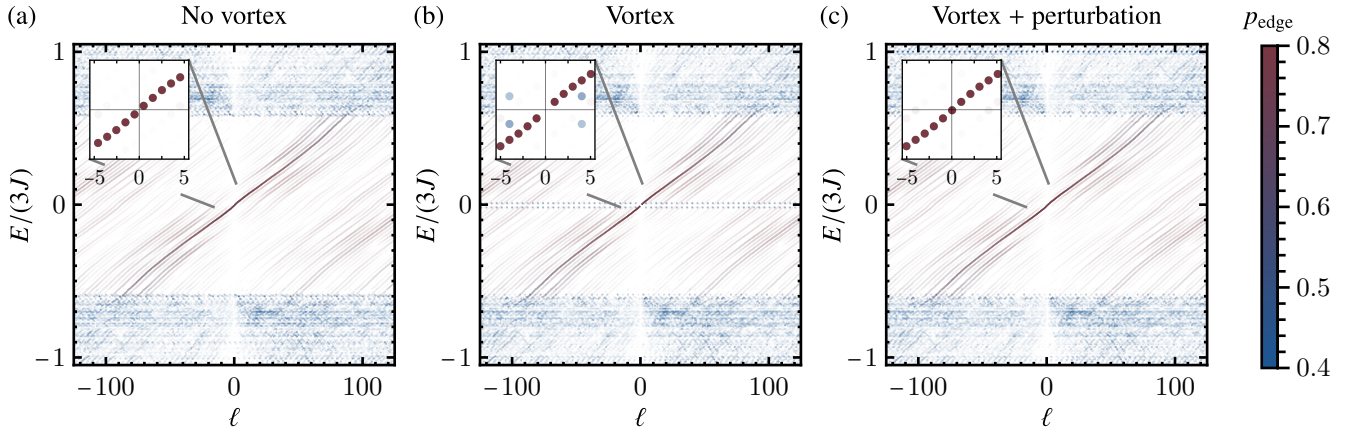


FIG. S19. Edge state dispersion in the chiral gapped phase. For each eigenstate $|\psi_n\rangle$ with energy E_n on the disk-shaped flake and for each angular momentum $\ell \in \frac{1}{2}\mathbb{Z}$, we plot at coordinates (ℓ, E_n) a data point whose color is set by the edge localization $p_{n,\text{edge}}$ [Eq. (S130), see color legend on the right] and whose opacity is given by the coefficient $c_{n,\ell}$ [Eq. (S131)]. Since most coefficients are close to zero, the vast majority of the data points are fully transparent and thus not visible. Only those data points (ℓ, E_n) remain visible whose coefficient $c_{n,\ell} \in [0, 1]$ is sufficiently larger than zero. (a) In the absence of a vortex, we identify a chiral Majorana mode localized at the boundary (displayed in red tones) at energies $|E|/(3J) \lesssim 0.6$. The inset reveals that the edge states carry half-integer angular momentum $\ell \in \mathbb{Z} + \frac{1}{2}$, as expected for chiral Majorana edge modes [78, 79] and in accordance with the phase growth data in Fig. S18a. The bulk states generate a featureless signal at $|E|/(3J) \gtrsim 0.6$ (displayed in blue tones). (b) In the presence of a \mathbb{Z}_2 vortex threaded through the plaquette at the center of the disk, the angular momentum of the Majorana edge modes is shifted to integer values. In addition, the vortex binds an additional Majorana mode whose coefficients $c_{n,\ell}$ exhibit large values at all $\ell = 0 \pmod{4}$. Due to finite-size effects, the Majorana modes expected at zero energy hybridize, resulting in two eigenstates at energy $E/(3J) \approx \pm 0.0138$ and with angular momentum $\ell = 0 \pmod{4}$. (c) To remove the undesired hybridization, we apply the perturbation in Eq. (S133) which shifts the Majorana mode at the vortex to energy $E/(3J) \approx 1$. In this case, we observe an approximately linear dispersion $E(\ell)$ with integer-valued angular momenta $\ell \in \mathbb{Z}$, as expected [78, 79] and in accordance with Fig. S18b.

Gaussian projector operator [29]

$$P_{\mu_E, \sigma_E} = \sum_n \exp \left[-\frac{(E_n - \mu_E)^2}{2\sigma_E^2} \right] |\psi_n\rangle \langle \psi_n|, \quad (\text{S134})$$

where we sum over all eigenstate labels n . Starting with a state $|\psi_{\text{loc.}}\rangle$ localized on a single site at the boundary of the disk (we specifically select the site with the largest horizontal coordinate $\text{Re}(z)$ and $\text{Im}(z) > 0$), the application of the Gaussian projector operator generates a state

$$|\psi_{\mu_E, \sigma_E}^{\text{w.p.}}\rangle = P_{\mu_E, \sigma_E} |\psi_{\text{loc.}}\rangle. \quad (\text{S135})$$

Provided that the range $|\mu_E \pm \sigma_E|$ is sufficiently smaller than the bulk energy gap, the operator P_{μ_E, σ_E} effectively projects onto the edge states. Because of the approximately linear dispersion $E(\ell)$ of the edge states in the chiral gapped phase, the Gaussian function of the eigenstate energy E_n in Eq. (S134) is simultaneously a Gaussian function of the angular momentum ℓ , i.e., the state $|\psi_{\mu_E, \sigma_E}^{\text{w.p.}}\rangle$ constructed in Eq. (S135) is a wave packet. As such, we expect the wave packet to propagate along the circumference of the disk with angular velocity $\omega = \partial E / \partial \ell$, which due to the chiral dispersion has a definite positive or negative sign. To test this prediction numerically, we choose $\mu_E = 0$ and $\sigma_E = 0.06$, which is one order of magnitude smaller than the bulk energy gap. The initial wave packet $|\psi_{\mu_E=0, \sigma_E=0.06}^{\text{w.p.}}\rangle$ is plotted in red in Fig. S20b. The evolution of this wave packet under unitary time evolution e^{-iHT} at times $3JT \in \{100, 200, 300\}$ is depicted in yellow/green/cyan in Fig. S20b. We observe the propagation of the Majorana wave packet in the counterclockwise (positive) direction, consistent with $\partial E / \partial \ell > 0$.

Let us finally contrast the Majorana edge states of the chiral gapped phase to edge states realized in gapped Abelian \mathbb{Z}_2 spin liquid phase. For concreteness, we consider the trivial gapped phase at parameters $J_x = J_y = 1/4$, $J_z = 1/2$ and $K = 0$, which also corresponds to the data in the bottom of Fig. 2b of the main text. The bulk and boundary DOS for this phase are displayed in Fig. S17e. We observe the formation of a zero-energy flat band on the boundary. Due to the somewhat large localization length of the corresponding eigenstates (indicated with purple arrow in Fig. S17f), the flat band remains visible as a small peak at $E = 0$ also in the numerically computed bulk DOS.

To illustrate the absence of chiral edge states in this phase, we consider again the wave packet construction in Eq. (S135), in this case taking as the seed the localized state $|\psi_{\text{loc.}}\rangle$ with equal-amplitude support on the two sites with the largest value of $\text{Re}(z)$

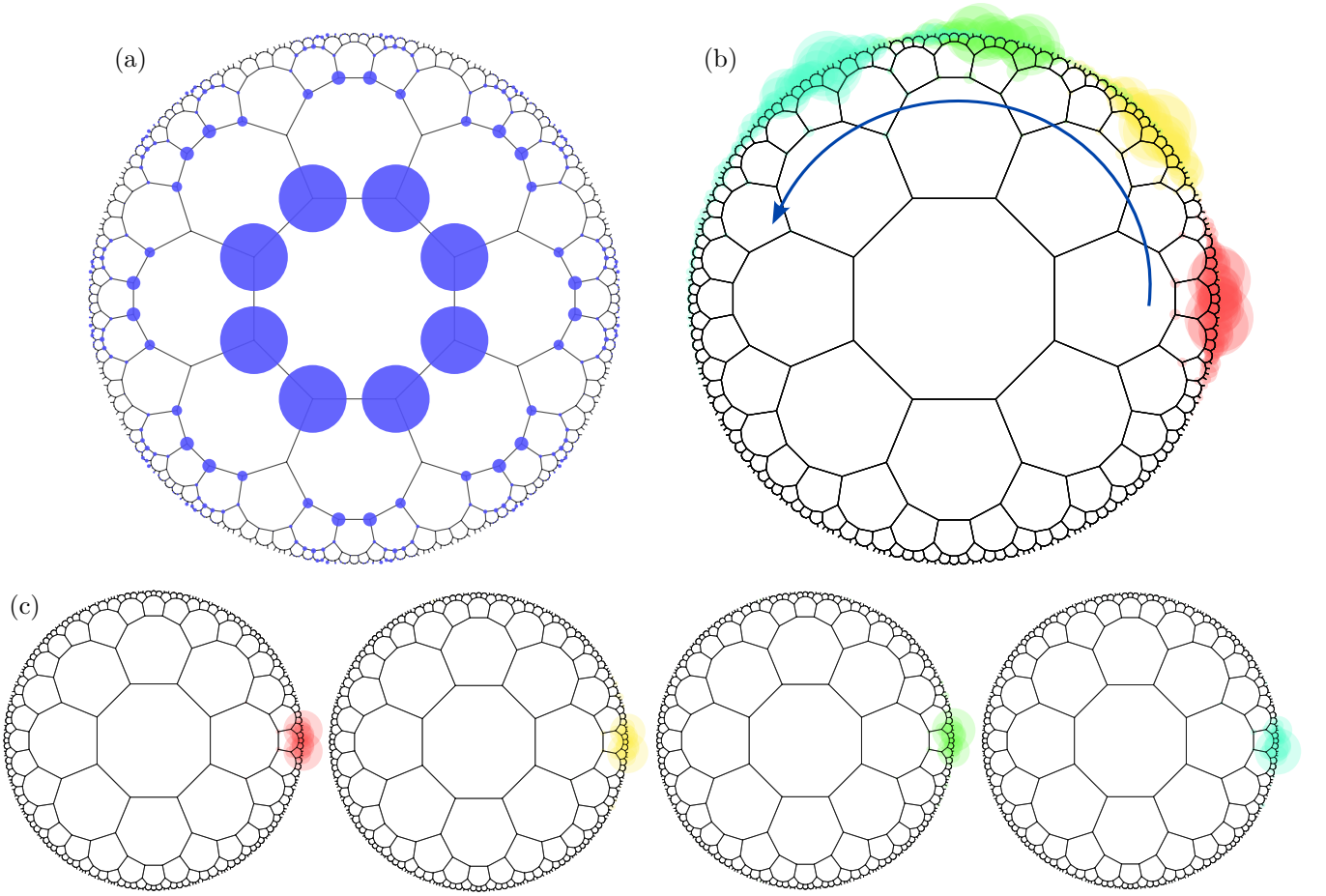


FIG. S20. (a) Plot of the Majorana mode bound to the \mathbb{Z}_2 vortex threaded through the central plaquette, computed using the procedure described around Eq. (S132). The area of the blue disk at site j is proportional to the probability density $|\psi_0^{\text{unmixed},2}(j)|^2$. (b) Propagation of the Majorana wave packet with $\mu_E = 0$ and $\sigma_E = 0.06$ in the chiral gapped phase. The red data show the initial wave packet as defined in Eq. (S135), and the subsequent yellow/green/cyan data show snapshots of the wave packet at equally spaced later times $3JT \in \{100, 200, 300\}$, respectively. The blue arrow indicates the counterclockwise propagation of the wave packet, with the direction fixed by $\partial E / \partial \ell > 0$. (c) Propagation of the wave packet with $\mu_E = 0$ and $\sigma_E = 0.12$ in the gapped Abelian \mathbb{Z}_2 spin liquid phase with parameters $J_x = J_y = 1/4$, $J_z = 1/2$ and $K = 0$. The red data show the initial wave packet, and the subsequent yellow/green/cyan data display snapshots of the wave packet at equally spaced later times $3JT \in \{100, 200, 300\}$, respectively. The wave packet evolution in this case exhibits no noticeable propagation nor broadening.

(one site has $\text{Im}(z) > 0$ while the other one has $\text{Im}(z) < 0$). Choosing $\mu_E = 0$ and $\sigma_E = 0.12$, we obtain the initial state plotted in red in Fig. S20c. Unitary time evolution with e^{-iHT} at times $3JT = \{100, 200, 300\}$, shown in yellow/green/cyan in Fig. S20c, indicates that (i) the state does not propagate in any definite direction around the disk and that (ii) the state does not noticeably broaden on the chosen time scale. The absence of clockwise/counter-clockwise propagation confirms the non-chiral character of the \mathbb{Z}_2 spin liquid phase, whereas the absence of broadening can be seen as a consequence of the flat-band (i.e., dispersionless) character of the edge states near $E = 0$.